Stability and Protective Coatings of Semiconductor Electrodes for Solar Fuel Devices

Thesis by

Pakpoom Buabthong

In Partial Fulfillment of the Requirements for
the Degree of
Doctor of Philosophy

CALIFORNIA INSTITUTE OF TECHNOLOGY
Pasadena, California

2021
Defended May 12, 2021

Pakpoom Buabthong
ORCID: 0000-0001-5538-138X

ACKNOWLEGEMENTS

First and foremost, I would like to thank my advisor, Prof. Nathan S. Lewis, who has provided tremendous support and helped me navigate the electrochemistry labyrinth during my time here. I would also like to thank Prof. Harry Gray for his guidance. His overwhelming positivity has helped correct my course any time I felt lost. I am grateful to the rest of my committee, Prof. Katherine Faber, Prof. William Goddard, and Prof. William Johnson for their expertise and their valuable discussion

Before I move on to other people in my social circle, I would like to thank all the readers of this thesis or any of my manuscripts. I have always thought of reading scientific articles as looking at the wrong side of a beautiful tapestry where the findings are often obscured behind a highly formal style of writing, which keeps it concise and accurate, yet often lacking the pathos found in other types of writing. It might be challenging to sift through the information provided here, but I truly appreciate your time reading this work.

I have learned almost all of my experimental techniques from Dr. Ke Sun, who is one of the most supportive and the hardest working researchers I have ever met. I have also gained much help and knowledge from Dr. Ivan Moreno-Hernandez, who always had answers to my questions.

My time at Caltech would not be the same without Slobodan Mitrovic. He has trained me on all the instruments and has helped me grow as a researcher. I also want to acknowledge Melissa Rojanapongpun for her help with artwork and illustrations during my Ph.D. I would like to thank everyone here at JCAP who made working here really fun: Joachim Lewerentz, Ryan Jones, Kyle Cummins, John Gregoire, Jack Baricuatro, Helge Stein, and Matthias Richter, who knows how to do everything.

I would like to thank everyone in the Lewis group for making my Ph.D. enjoyable and for providing guidance throughout my time here, particularly, Paul Kempler, Katherine Rinaldi, Harold Fu, Zach Ifkovits, Jake Evans, Jackie Dowling, and the former G135 residents: Xinghao Zhou, Carlos Read for making G135 the best office on campus. And I would also like to thank all the non-G135 natives: Weilai Yu, Ellen Yan, Kathleen Kennedy, Ethan Simonoff, Katie Chen, Katie Hamann, Azhar Carim, Michael Mazza, Madeline Meier, Mo Morla, and many more.

I want to thank the wonderful team of administrators: Christy Jenstad, Jennifer Blankenship, Barbara Miralles, and Mabby Howard for all your support that made my PhD so much more memorable, as well as the Caltech staff for being awesome at your work and wonderful friends, especially Brian Markowicz, Denise Rodriquez, and JF Bonavich.

During all my time, I have received numerous encouragements from the “Yangji” group: I don’t have words to express my gratitude to all of you: Claire Kuo, Jash Banker, Michelle Cua, Joeson Wong, Sam Loke, Nori Arai, and Shiori Arai. I would also like to thank my Thai scholar friends who had started this journey with me in 2010, especially Grace Anantaya

Wonaphotimuke, Fa Ngamnithiporn, Nut Pombubpa, and Champ Taweewat Somboonpanyakul, as well as all the Thai community here at Caltech. I want to give a special thanks to Papis Wongchaisuwat for all her support during my time.

I would like to thank the Association for Thai Democracy for giving me a sense of purpose outside of my academic life. I want to extend my special thanks to Toy Jatuporn Leksut and Pongkwan Sawasdipakdi for their companionship that has helped me get through the last few months of my PhD career.

I would also like to thank all of my friends at Aero Association of Caltech (Caltech Flying Club), Greg Schultz, Carlyn Lee, and especially, my instructor Joe O'Rouke, who has enabled me to step back when something went wrong in my experiments, and look at my problem literally from 3000-feet above.

Most importantly, I want to thank Whay Warisa Ketphan for always being there and listening to my endless complaints about everything. My cats back home also deserve my thanks for all their love and support. Last but not least, I would like to thank my parents, Narong and Sirinkorn Buabthong for their unwavering support.

ABSTRACT

Climate change and increasing global energy consumption drive the need for clean and renewable alternatives to fossil fuels. Photoelectrochemical solar fuel devices offer a potential solution to capture and store clean and renewable solar energy in chemical bonds. Nevertheless, degradation of semiconductor electrodes is one of the major impediments to the implementation of practical stable solar fuels systems.

Herein, we investigate the corrosion mechanisms and the corrosion kinetics of CdTe and ZnTe cathodes under the conditions for hydrogen-evolution reaction in strong acid and strong alkaline media. The effects of catalyst over-layer on CdTe's and ZnTe's corrosion pathways are discussed as well as potential protective coatings for ZnTe cathodes. Then, we address the original physical pinhole defects in amorphous a-TiO_2 grown by atomic-layer deposition (ALD) on GaAs anodes. In addition, we explore new pinhole formation during electrochemical experiments and provide simulation for the propagation of the corroding GaAs substrate after new exposure to the electrolyte through microscopic pinholes. Finally, we develop a fabrication procedure for GaAs micro-island structures to provide defect isolation on the a-TiO_2 film. The micro-island structures combined with dissolution measurements of the ALD a-TiO_2 films were used to study the distribution and the evolution of pinholes from pre-existing defect spots in the protective coatings.

PUBLISHED CONTENT AND CONTRIBUTIONS

Buabthong, P., Jiang, J., Yu, W., Moreno-Hernandez, I., Papadantonakis, K. M., Brunschwig, B. S., Lewis, N. S. "Chemical and Electrochemical Corrosion Behaviors of CdTe and ZnTe Electrodes under Conditions Relevant for Hydrogen Evolution Reaction." *in preparation*. Adapted for Chapter 2.
P. B. participated in the conception of the project, prepared the data, and participated in the writing of the manuscript.

Buabthong, P., Ifkovits, Z. P., Kempler, P. A., Chen, Y., Nunez, P. D., Brunschwig, B. S., Papadantonakis, K. M., Lewis, N. S. "Failure Modes of Protection Layers Produced by Atomic Layer Deposition of Amorphous TiO_2 on GaAs Anodes." *Energy Environ. Sci.* (2020) **13**, 4269-427. DOI: 10.1039/D0EE02032J. Adapted for Chapter 3.
P. B. participated in the conception of the project, prepared the data, and participated in the writing of the manuscript.

Buabthong, P., Evans, J., Rinaldi, K. Z., Kennedy, K. M., Fu, H. J., Ifkovits, Z. P., Kuo, T.-J., Brunschwig, B. S., Lewis, N. S. "GaAs Micro-island Anodes Protected by Amorphous TiO2 Films Mitigate Corrosion Spreading Due to Pitting and Enhance Anode Durability for Water Oxidation in Alkaline Electrolytes." in preparation. Adapted for Chapter 4.
P. B. participated in the conception of the project, prepared the data, and participated in the writing of the manuscript.

Buabthong, P., Becerra-Stasiewicz, N., Mitrovic, S., Lewis, N. S., "Vanadium, Niobium and Tantalum by XPS." *Surface Sci. Spec.* (2017) **24**, 024001. DOI: 10.1116/1.4998018.
P. B. participated in the conception of the project, prepared the data, and participated in the writing of the manuscript.

Yu, W., **Buabthong, P.**, Read, C. G., Dalleska, N. F., Lewis, N. S., Lewerenz, H.-J., Gray, H. B., Brinkert, K. "Cathodic NH^{4+} Leaching of nitrogen impurities in CoMo thin-film electrodes in aqueous acidic solutions." *Sustainable Energy Fuels*, 2020, 4, 5080-508. DOI: 10.1039/D0SE00674B.
P. B. participated in the conception of the project, collected and analyzed XPS data, and participated in the writing of the manuscript.

Fu, H. J., Moreno-Hernandez, I., **Buabthong, P.**, Papadantonakis, K. M., Brunschwig, B. S., Lewis, N. S. "Enhanced stability of silicon for photoelectrochemical water oxidation through self-healing enabled by an alkaline protective electrolyte." *Energy Environ. Sci.*, (2020), **13**, 4132-4141. DOI: 10.1039/D0EE02250K.
P. B. collected and analyzed XPS data and participated in the discussion of the project,

Read, C. G., **Buabthong, P.**, "Growth and characterization of single-crystalline oxynitride materials for solar fuels production." *in preparation*. Adapted for Appendix A.

P. B. participated in the conception and discussion of the project, collected and analyzed XPS data.

Yu, W., Richter, R. H., **Buabthong, P.**, Moreno-Hernandez, I., Read, C. G., Simonoff, E., Papadantonakis, K. M., Brunschwig, S. B., Lewis, N. S. "The Stability of InP Photocathode for Solar-driven Hydrogen Evolution in Aqueous Acidic and Alkaline Electrolyte." *in preparation*.
P. B. participated in the conception and discussion of the project, collected and analyzed XPS data.

TABLE OF CONTENTS

NOMENCLATURE

AFM. Atomic force microscopy

CA. Chronoamperometry

CB. Conduction band

CV. Cyclic voltammetry

E_g. Band gap energy

HER. Hydrogen evolution reaction

Hg/HgO. Mercury-mercury oxide electrode

Hg/HgS. Mercury-mercurous sulfate electrode

ICP-MS. Inductively coupled plasma mass spectrometry

n^{++}. Degenerately-doped n-type material

n+. highly-doped n-type material

OER. Oxygen evolution reaction

p++. Degenerately-doped p-type material

p+. highly-doped p-type material

OCV. Open-circuit voltage

RHE. Reversible hydrogen electrode. The reversible potential for HER

SCE. Saturated calomel electrode

SEM. Scanning electron microscopy

VB. Valence band

XPS. X-ray photoelectron spectroscopy

Chapter 1

INTRODUCTION

Global energy demand

The global energy demand has been rising since the Industrial Revolution mostly because of population growth and modernization of developing countries. The current energy demand is expected to continue to increase in the next decades.[1] Currently, the majority of the global energy supply rely on burning fossil fuels, detrimental to the environment.

Since the Industrial Revolution, the anthropogenic greenhouse gas emission has been observed to increase at 2.2 %/year from 2000 to 2010 and will likely continue to increase at a higher rate; the majority of the greenhouse gas was reported to come from CO_2 emission from the industrial processes.[2] At the current emission rate, the atmospheric CO_2 concentration is predicted to exceed 550 ppm in 2100.[3] The increasing CO_2 concentration is found to have a strong correlation in the increase in the average temperature change.[1,3] Out of all anthropogenic CO_2, ~30 % will also be absorbed by the ocean, causing ocean acidification which is detrimental to marine organisms.[1]

Although CO_2 is the most prominent air contaminant from fossil fuel combustion, sulfur and nitrogen in fossil fuels can also release SO_2 and NO_x pollutants. These pollutants react with atmospheric water vapor and other gases to form fine particulate matter (PM2.5), which is one of the main causes of severe air pollution in major cities.

Solar energy

To sustainably meet the increasing global energy demand, clean, renewable, and abundant energy source is needed. Solar energy is one of the most promising candidates.[4] The terrestrial solar energy flux is ~36,000 TW,[5] substantially higher than other renewable

options, namely, hydro, geothermal, and wind energy.[6] Nevertheless, energy storage is still needed for the solar energy to reliably meet the daily energy demand. Figure 1.1 shows the net load, which is calculated by taking the forecasted load and subtracting the forecasted electricity production from renewable energy sources (wind and solar). When there is an excess supply during the morning, the electricity grid would face a risk of potential overgeneration. On the other hand, in the evening where solar energy is not available, the grid would require energy from other sources.

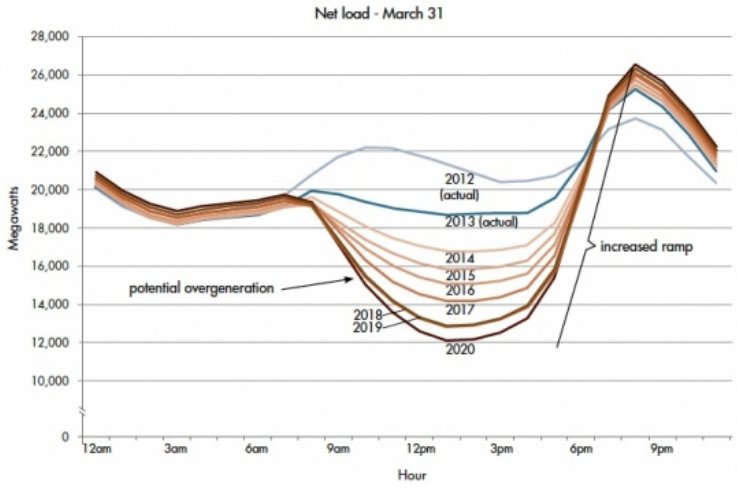

Figure 1.1. Net load (energy demand subtracted by energy supply) of renewable energy source. (reproduced)[7]

Solar fuel conversion system

Lithium-ion batteries or redox flow batteries offer a possible solution to energy storage, yet they are challenging to implement because of high cost and low performance for large-scale application. On the other hand, chemical fuels, including hydrogen (H_2), have higher energy density and potentially lower cost of production. Solar fuels conversion system is one of the options to directly convert solar energy into chemical bonds. The work in this thesis focuses on photoelectrochemical (PEC) water-splitting, but the principles are also applicable to other solar fuels production, including CH_4, C_2H_4, CH_3OH.

The reaction for water-splitting (Eq. 1.1) has a free energy requirement of ΔG = 237.2 kJ mol^{-1}, which corresponds to $\Delta E°$ 1.23 V per electron.

$$2H_2O_{(l)} \rightarrow 2H_{2(g)} + O_{2(g)} \quad \text{(Eq. 1.1)}$$

In acidic solutions, the following half-reactions are expected:

$$2H^+ + 2e^- \rightarrow H_{2(g)} \quad \text{(Eq. 1.2)}$$

$$2H_2O_{(l)} \rightarrow O_{2(g)} + 4H^+ + 4e^- \quad \text{(Eq. 1.3)}$$

In alkaline solutions, the following half-reactions are expected

$$2H_2O_{(l)} + 2e^- \rightarrow H_{2(g)} + 2OH^- \quad \text{(Eq. 1.4)}$$

$$4OH^-_{(aq)} \rightarrow O_{2(g)} + 2H_2O_{(l)} + 4e^- \quad \text{(Eq. 1.5)}$$

here, Eq. 1.2 and Eq. 1.4 correspond to oxygen evolution reactions (OER) and Eq. 1.3 and Eq. 1.5 correspond to hydrogen evolution reactions (HER).

One of the prominent PEC water-splitting system designs focused on in this work consists of semiconducting light-absorber electrodes with cathodes and anodes doing HER and OER, respectively. In a PEC device, at least one of the electrodes is a semiconductor material which can generate carriers. Upon illumination, an electron-hole pair is generated and driven by the potential gradient in the semiconductor materials to their respective side of the device (Fig. 1.2). In order to drive the water-splitting reaction (Eq. 1.1), the electron-hole pair would need to have at least 1.23 eV for the minimum thermodynamic requirement. Nevertheless, in a practical solar fuels device, pH difference, solution resistance, or non-radiative recombination reduce the electron-hole pair energy, thus requiring the light-absorbers to provide the voltage higher than the thermodynamic minimum.[8]

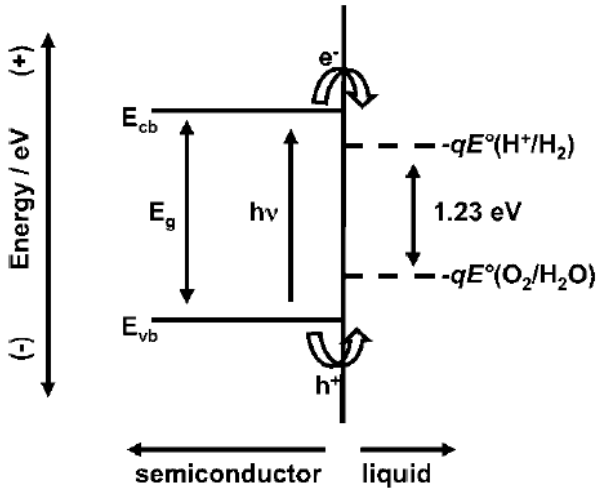

Figure 1.2. Schematics of the band alignment of a semiconductor in acid. (reproduced from Royal Society of Chemistry, RSC)[9]

In order to supply sufficient potential, the semiconducting materials must have large bandgaps, typically ~2.2 eV. However, materials with a 2.2 eV bandgap only absorb a small portion of the solar spectrum (Fig. 1.3). Instead of single-layer light-absorbing materials, tandem device structures can be utilized to allow for broader absorption while providing enough potential to drive the water-splitting reaction. One of the bandgap combinations for a tandem device is with a 1.7 eV bandgap top-cell and a 1.1 eV bandgap bottom-cell.[8] Silicon (Si) is one of the most promising materials for the bottom cell because of its 1.1 eV bandgap, suitable band edge position, as well as established fabrication processes. The suitable top-cell with 1.7 eV bandgap still needs further development.

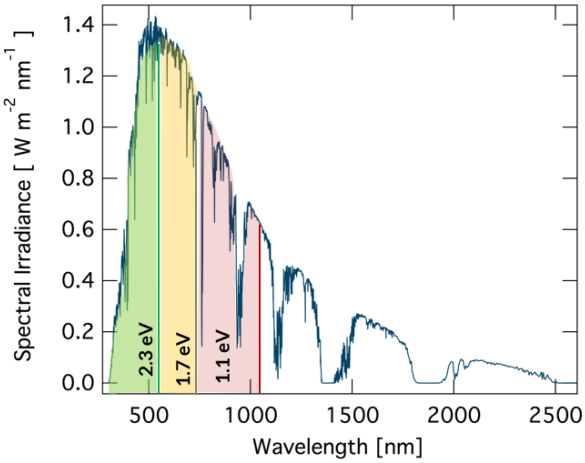

Figure 1.3. AM1.5 G irradiation (100 mW cm^{-2}) with the shaded areas corresponding to the absorption upperbound of semiconductors with 2.3-eV, 1.7-eV, and 1.1-eV bandgap.

Stability of semiconductor electrodes

One of the major impediments for realizing practical solar fuels devices is their stability under operation.[10] Since the devices typically need to operate under corrosive strong acid or strong alkaline electrolyte, the solar fuel devices typically have operational stability in an order of 1,000 to 10,000 of hours.[11] Unlike corrosion behaviors of metals, the corrosion mechanisms of semiconductor electrodes are still lacking.

A general framework for defining stability of photoelectrodes is outlined in Fig. 1.4a, based on the relative energy levels of conduction band (CB) edge and the potentials of cathodic corrosion and solvent reduction (HER).[12,13] If a competition for photogenerated electrons exists for cathodic corrosion reaction and HER (quasi-stable, type b), the semiconductor stability will be critically determined by the position of the quasi Fermi level (E_{qf}) or the kinetic over-potential. If the cathodic corrosion is thermodynamically more difficult compared with the HER, the semiconductor photocathode can be kinetically stabilized against cathodic corrosion by selectively steering all photogenerated electrons to perform HER. This framework also applies to OER where

the energetic levels between the semiconduction decomposition and OER need to compete for the generated holes. Manipulating the energetics at this semiconductor-electrolyte interface may allow for a stable device from otherwise thermodynamically unstable materials. For example, catalyst loading on the electrode's surface may lower the band edge such that HER is more energetically favorable than the decomposition of the semiconductors (Fig. 1.4b). Understanding the kinetic effects towards the semiconductor corrosion will not only be useful for validating this framework, but also expand our fundamental understanding on stabilization of practical solar fuels devices.

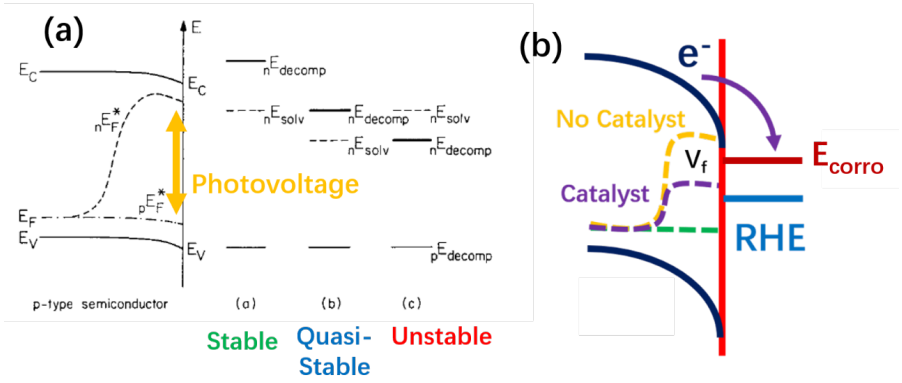

Figure 1.4. Band alignment diagram outlining different corrosion behaviors (a) General framework for defining the photocathode stability (p-type semiconductor) based on the relative energetic positions of the conduction band (E_{CB}), decomposition potential (E_{decomp}), and solvent reduction (E_{solv}). Three types of photocathodes can be classified: (i) Stable: $E_{decomp}<E_{CB}<E_{solv}$; (ii) quasi-stable: $E_{CB}<E_{decomp}<E_{solv}$; (iii) unstable: $E_{CB}<E_{solv}<E_{decomp}$. (Adapted from Gerischer *et al*[12]) (b) Proposed kinetic effects of HER catalysts over the semiconductor stability for the quasi-stable type.

Protective coatings

Instead of developing materials that are intrinsically stable under operation, applying protective coatings to the electrodes is also another promising way to increase the overall stability of the solar fuels devices. Since the generated electrons/holes need to reach the electrode surface to evolve oxygen/hydrogen, the main requirement for the protective

coatings of solar fuels devices is to provide electronic conductivity while separating the semiconductors from the electrolyte and providing sufficient transmission of the light to the underlying substrates. Although protective coatings are needed for both photoanodes and photocathodes, this work focuses on the protection for photoanodes as the anodes are typically prone to both passivation and decomposition because of the higher applied oxidative potential at the anode side.

Amorphous TiO_2 (a-TiO_2) grown by atomic layer deposition (ALD) is one of the promising protective layers for photoanodes.[14] These a-TiO_2 films mitigate parasitic absorbance due to a large band gap (3.3 eV), prevent corrosion due to the stability of a-TiO_2 in alkaline and acidic media, and can maintain ohmic contact with the solution even with 100 nm thick films due to interaction of a Ti^{3+} defect band with metal catalysts.[14–16] PEC systems incorporating an a-TiO_2 protection layer have been demonstrated to be stable for hundreds of hours in both alkaline and acidic media.[11]

Although a-TiO_2 film has been shown to increase the stability of the devices under operation, the failure modes for the film are still not fully understood. Microscopic defects and pinholes have been hypothesized to be the dominating attribution to the device failure.[11,14,17–19] These pinholes are especially detrimental to non-passivating substrates such as III-V or II-VI semiconductors, since any exposure of the substrate to the electrolyte would rapidly corrode the underlying electrodes.[17] Understanding the origins and the evolution of these pinholes on a-TiO_2 would allow for better corrosion mitigation techniques and eventually realizing stable solar fuels devices.

Contents of this thesis

In this thesis, intrinsic stability and corrosion mechanisms of CdTe and ZnTe under conditions for HER are presented. Failure modes of ALD a-TiO_2 films are investigated and fabrication processes for GaAs micro-island structures are developed to accompany defect isolation in the a-TiO_2 films.

- In Chapter 2, chemical and electrochemical corrosion behaviors of CdTe and ZnTe cathodes are presented. The effects of Pt catalysts and a-TiO_2 are also discussed.
- In Chapter 3, short-term failure modes of GaAs anodes coated a-TiO_2 is presented. The correlation between atmospheric particulates and microscopic pinholes on the as-deposited a-TiO_2 is discussed. Simulation of the corrosion front at the exposed GaAs substrates is also provided.
- In Chapter 4, fabrication procedures for GaAs micro-island structures are presented The evolution of new pinhole sites developed from defect spots in the a-TiO_2 film is discussed.
- In Appendix, preliminary results for the growth of oxynitride films for corrosion studies is presented.

References

(1) IEA. *World Energy Outlook 2020*; Paris, 2020.

(2) Pachauri, R. K.; Meyer, L. A. *Climate Change 2014: Synthesis Report. Contribution of Working Groups I, II and III to the Fifth Assessment Report of the Intergovernmental Panel on Climate Change*; 2015.

(3) Karl, T. R.; Melillo, J. M.; Peterson, T. C. *Global Climate Change Impacts in the United States*; 2009.

(4) Lewis, N. S. Research Opportunities to Advance Solar Energy Utilization. *Science (80-.).* **2016**, *351* (6271). https://doi.org/10.1126/science.aad1920.

(5) Jiang, C.; Moniz, S. J. A.; Wang, A.; Zhang, T.; Tang, J. Photoelectrochemical Devices for Solar Water Splitting – Materials and Challenges. *Chem. Soc. Rev.* **2017**, *46* (15), 4645–4660. https://doi.org/10.1039/C6CS00306K.

(6) Murphy, P. Solar Update, in Solar Heating and Cooling Programme. **2020**.

(7) California Independent System Operator. *Renewable Fast Facts*; 2016.

(8) Hu, S.; Xiang, C.; Haussener, S.; Berger, A. D.; Lewis, N. S. An Analysis of the Optimal Band Gaps of Light Absorbers in Integrated Tandem Photoelectrochemical Water-Splitting Systems. *Energy Environ. Sci.* **2013**, *6* (10), 2984. https://doi.org/10.1039/c3ee40453f.

(9) Walter, M.; Warren, E. Solar Water Splitting Cells. *Chem. Rev.* **2010**, *110*, 6446–6473.

(10) Tan, M. X.; Laibinis, P. E.; Nguyen, S. T.; Kesselman, J. M.; Stanton, C. E.; Lewis, N. S. Principles and Applications of Semiconductor Photoelectrochemistry. In *Progress in Inorganic Chemistry*; John Wiley & Sons, Inc., 1994; pp 21–144. https://doi.org/10.1002/9780470166420.ch2.

(11) Bae, D.; Seger, B.; Vesborg, P. C. K.; Hansen, O.; Chorkendorff, I. Strategies for Stable Water Splitting via Protected Photoelectrodes. *Chem. Soc. Rev.* **2017**, *46* (7), 1933–1954. https://doi.org/10.1039/C6CS00918B.

(12) Gerischer, H.; Mindt, W. The Mechanisms of the Decomposition of Semiconductors

by Electrochemical Oxidation and Reduction. *Electrochim. Acta* **1968**, *13* (6), 1329–1341. https://doi.org/10.1016/0013-4686(68)80060-X.

(13) Gerischer, H. Electrolytic Decomposition and Photodecomposition of Compound Semiconductors in Contact with Electrolytes. *J. Vac. Sci. Technol.* **1978**, *15* (4), 1422–1428. https://doi.org/10.1116/1.569800.

(14) Hu, S.; Shaner, M. R.; Beardslee, J. A.; Lichterman, M.; Brunschwig, B. S.; Lewis, N. S. Amorphous TiO_2 Coatings Stabilize Si, GaAs, and GaP Photoanodes for Efficient Water Oxidation. *Science* **2014**, *344* (6187), 1005–1009. https://doi.org/10.1126/science.1251428.

(15) Hu, S.; Richter, M. H.; Lichterman, M. F.; Beardslee, J.; Mayer, T.; Brunschwig, B. S.; Lewis, N. S. Electrical, Photoelectrochemical, and Photoelectron Spectroscopic Investigation of the Interfacial Transport and Energetics of Amorphous TiO2/Si Heterojunctions. *J. Phys. Chem. C* **2016**, *120* (6), 3117–3129. https://doi.org/10.1021/acs.jpcc.5b09121.

(16) Nunez, P.; Richter, M. H.; Piercy, B. D.; Roske, C. W.; Cabán-Acevedo, M.; Losego, M. D.; Konezny, S. J.; Fermin, D. J.; Hu, S.; Brunschwig, B. S.; Lewis, N. S. Characterization of Electronic Transport through Amorphous TiO 2 Produced by Atomic Layer Deposition. *J. Phys. Chem. C* **2019**, *123* (33), 20116–20129. https://doi.org/10.1021/acs.jpcc.9b04434.

(17) Verlage, E.; Hu, S.; Liu, R.; Jones, R. J. R.; Sun, K.; Xiang, C.; Lewis, N. S.; Atwater, H. A. A Monolithically Integrated, Intrinsically Safe, 10% Efficient, Solar-Driven Water-Splitting System Based on Active, Stable Earth-Abundant Electrocatalysts in Conjunction with Tandem III–V Light Absorbers Protected by Amorphous TiO_2 Films. *Energy Environ. Sci.* **2015**, *8* (11), 3166–3172. https://doi.org/10.1039/C5EE01786F.

(18) Ros, C.; Carretero, N. M.; David, J.; Arbiol, J.; Andreu, T.; Morante, J. R. Insight into the Degradation Mechanisms of Atomic Layer Deposited TiO_2 as Photoanode Protective Layer. *ACS Appl. Mater. Interfaces* **2019**, *11* (33), 29725–29735.

https://doi.org/10.1021/acsami.9b05724.

(19) Yu, Y.; Sun, C.; Yin, X.; Li, J.; Cao, S.; Zhang, C.; Voyles, P. M.; Wang, X. Metastable Intermediates in Amorphous Titanium Oxide: A Hidden Role Leading to Ultra-Stable Photoanode Protection. *Nano Lett.* **2018**, *18* (8), 5335–5342. https://doi.org/10.1021/acs.nanolett.8b02559.

Chapter 2

CHEMICAL AND ELECTROCHEMICAL CORROSION BEHAVIORS OF CdTe AND ZnTe ELECTRODES UNDER CONDITIONS RELEVANT FOR HYDROGEN EVOLUTION REACTION

The following chapter discusses the chemical and electrochemical corrosion of CdTe and ZnTe substrates.

Content in this chapter is drawn from the following publication:

- **Buabthong, P.**, Jiang, J., Yu, W., Moreno-Hernandez, I., Papadantonakis, K. M., Brunschwig, B. S., Lewis, N. S. "Chemical and Electrochemical Corrosion Behaviors of CdTe and ZnTe Electrodes under Conditions Relevant for Hydrogen Evolution Reaction." *In preparation*.

Abstract

The corrosion behaviors of CdTe and ZnTe electrodes for hydrogen evolution reaction (HER) were studied in 1.0 M H_2SO_4 (aq) and 1.0 M KOH (aq) under applied potential as -100 mV *vs.* RHE and under open-circuit potential (OCV). Chemical corrosion was observed in both CdTe and ZnTe in acidic solution with the corrosion rate of 0.33 nm hr^{-1} and 0.10 nm hr^{-1} for CdTe under biased and under OCV, and 11 nm hr^{-1} for ZnTe in both conditions. Reduction of Cd^{2+} was found to be the primary pathway of CdTe corrosion in alkaline solution. Both oxidation of Te^{2-} and reduction of Zn^{2+} were found to be the main corrosion pathway for ZnTe. Corrosion of CdTe in alkaline media can be mitigated by applying a thin Pt catalyst layer to compete with the reductive corrosion reaction. However, protective coating is needed to reduce the dissolution of ZnTe in the alkaline solution.

Introduction

Photoelectrochemical (PEC) water-splitting is one of the attractive ways to store solar energy into clean hydrogen fuels. Nevertheless, degradation of semiconductor photoelectrodes is a well-known impediment to implementing efficient and practical solar fuels systems.[1,2] A great deal of information is available about the corrosion and passivation processes that lead to failure of photoanodes[3,4], and much less is defined about the behavior of photocathodes, except for largely phenomenological observations of limited (seconds-hours) lifetimes of such systems in aqueous media.[5–7]

Silicon (Si) is one of the promising candidates for photoelectrodes, due to its small band gap, a suitable band edge position, and earth abundance.[8] Extensive efforts have been made to protect Si photoelectrodes in acid and base.[6,7,9] Recent developments provide a new opportunity to more fully understand, control, and mitigate failure of a variety of photoelectrodes for solar fuels production. Of specific interest are II-VI semiconductors such as CdTe and ZnTe, whose band gaps can be tuned by alloying, and pair well with stabilized Si photoanodes to potentially produce high-efficiency (>20% solar-to-hydrogen) tandem photoelectrochemical cells.[8]

CdTe and ZnTe have been demonstrated as photocathodes in photoelectrochemical fuels production system.[10–12] The stability of CdTe and ZnTe under hydrogen evolution reaction have been studied but only to a limited extent where the device degradation was inferred from the decrease in photocurrent density.[10,13] The Pourbaix diagrams of CdTe and ZnTe can help provide theoretical guidelines for thermodynamic stability of the electrodes. However, experimental validation is still needed to confirm these thermodynamic predictions. Additionally, investigations of the corrosion kinetics of CdTe and ZnTe photoelectrodes are still needed in order to fully understand the corrosion behaviors and evaluate the usability of CdTe and ZnTe, or CdZnTe as potential semiconductor materials for stable photocathodes.

Herein, we describe the chemical and electrochemical corrosion behaviors of dark n-CdTe and n-ZnTe electrodes, biased at conditions relevant for hydrogen evolution

reaction (HER). The corrosion reactions of each condition were inferred from a comprehensive observation of the systems, namely, product dissolution, surface chemistry, and the morphology of the electrodes. We also examined the effect of Pt catalysts and thin TiO_2 protective coatings on the stability of CdTe and ZnTe electrodes.

Results

Dissolution of n-CdTe and n-ZnTe

The corrosion mechanism of n-type semiconductors (n-SC), n-CdTe and n-ZnTe electrodes were tested at -100 mV *vs.* reversible hydrogen electrode (RHE). This primary potential (*E*) of interest is determined by the overpotential (η) of an active electrocatalyst (such as noble metals and metal phosphides) required to drive a current density (*J*) of 10 mA cm^{-2}.[14] The position of the surface potential or quasi Fermi-level (E_{qf}) of an illuminated p-type semiconductor (p-SC) photoelectrode, in the presence of HER catalyst, should closely follow that of an n-SC electrode held at -0.1 V vs. RHE in the dark (Fig. S2.1). Hence, the thermodynamic environments regulating the semiconductor stability should be similar at the front surfaces of an n-SC in the dark and an illuminated p-SC with HER catalysts. Dark experiments moreover allow for probing the mechanism of semiconductor's intrinsic corrosion under well-controlled conditions of HER (*E*~-100 mV *vs.* RHE), by eliminating any variation in the photoelectrochemical (PEC) response of illuminated electrode. Hence, these dark experiments will provide valuable insights into how the corrosion or dissolution of semiconductors under HER conditions correlates with the thermodynamic predictions from the Pourbiax diagrams.

Chronoamperometry profiles of both n-CdTe and n-ZnTe biased at -100 mV *vs.* RHE in both 1.0 M H_2SO_4(aq) and 1.0 M KOH(aq) in the dark exhibit very small current densities as shown in a representative Fig. S2.2. The current densities stayed in the magnitude of μA cm^{-2} range.

Figure 2.1a shows the total dissolution product as a function of time of n-CdTe electrodes in the dark biased at -100 mV *vs.* RHE ("CA", red) and under OCV (purple) in H_2(g)-saturated 1.0 M H_2SO_4(aq) over 24 hours. The dissolution of each electrode was normalized to the electrode areas. The error bars represent variations between three electrochemical runs. The total dissolution concentrations are similar for both CA and

OCV. The dissolution in the first hour increased substantially from zero to ~0.05 µmol cm^{-2}, then continued to increase at a much slower rate after 2 hours, and increased to the maximum of ~0.05 µmol cm^{-2} at 24 hours. Figure 1b shows the dissolution rate of Cd and Te species H_2(g)-saturated 1.0 M H_2SO_4(aq), measured after the initial spike in the first hour. Cd and Te dissolution was ~0.8 µmol cm^{-2} hr^{-1} and ~0.4 µmol cm^{-2} hr^{-1} for the samples held under -100 mV *vs.* RHE, respectively. On the other hand, Cd and Te dissolution was ~0.4 µmol cm^{-2} hr^{-1} and ~0.8 µmol cm^{-2} hr^{-1} for the samples held under OCV.

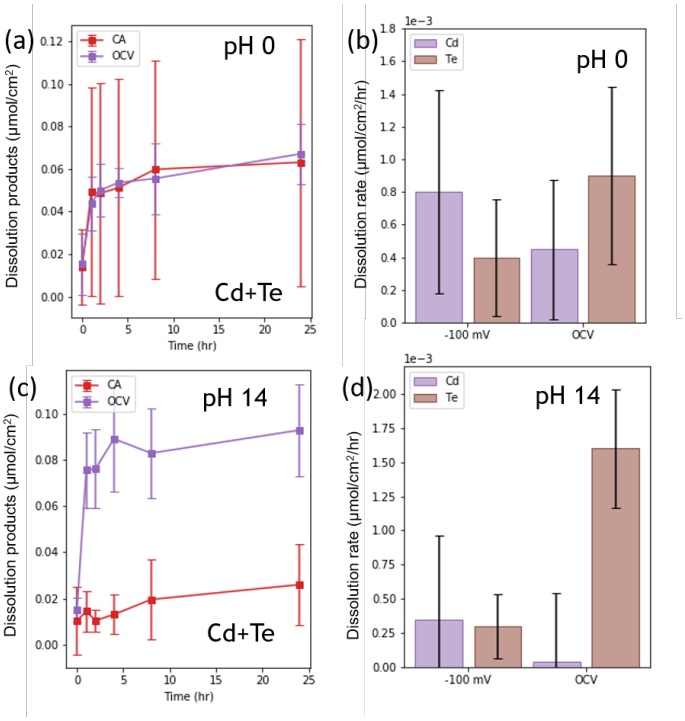

Figure 2.1. Dissolution products of CdTe (a,c) Concentrations of dissolved Cd, Te species in the working compartment biased at -100 mV vs. RHE and OCV in the dark over 24 hours, normalized to the electrode area in H_2(g)-saturated (a) 1.0 M H_2SO_4(aq) and (b) 1.0 M KOH(aq). (b, d) the dissolution rate measured after the initial dissolution in the first hour for the n-CdTe electrodes in (b)1.0 M H_2SO_4(aq) and (d) 1.0 M KOH(aq).

Figure 2.1c shows the total dissolution product as a function of time of n-CdTe electrodes in the dark biased at -100 mV *vs.* RHE ("CA", red) and under OCV (purple) in H_2(g)-saturated 1.0 M KOH(aq) over 24 hours. The total dissolution concentrations are higher for the sample held under open-circuit potential, which increased substantially from zero to ~0.08 μmol cm^{-2} within the first hour, then continued to increase at a much slower rate after 2 hours. On the other hand, in the total dissolution for the samples held under -100 mV *vs.* RHE, no initially dissolution spike was observed. Nevertheless, the total dissolution gradually increased to ~0.2 μmol cm^{-2} after 24 hours. Figure 2.1d shows the dissolution rate of Cd and Te species in H_2(g)-saturated 1.0 M KOH(aq) measured after the initial spike in the first hour. For the samples held under -100 mV *vs.* RHE, both Cd and Te dissolution rates were similar at ~0.25 μmol cm^{-2} hr^{-1}. However, for the samples at open-circuit potential, the Te dissolution rate was substantially higher at ~1.5 μmol cm^{-2} hr^{-1} compared to that of Cd at ~0.08 μmol cm^{-2} hr^{-1}.

Similarly, ZnTe electrodes were tested under -100 mV *vs.* RHE and OCV while monitoring the dissolution products in the working-electrode compartment. Figure 2.2a shows the total dissolution product as a function of time of n-ZnTe electrodes in the dark biased at -100 mV *vs.* RHE ("CA", red) and under OCV (purple) in H_2(g)-saturated 1.0 M H_2SO_4(aq) over 8 hours. The total dissolution concentrations are similar for both the samples held under open-circuit potential and held at -100 mV *vs.* RHE. Unlike n-CdTe samples, no initial spikes were observed in the first hour; the dissolutions for n-ZnTe samples linearly increased from zero to 1.5 μmol cm^{-2} at 8 hours. Figure 2.2b shows the dissolution rate of Zn and Te species in H_2(g)-saturated 1.0 M H_2SO_4(aq). Since the dissolution products increased linearly from the start, the rates were calculated from the whole time span of the electrochemical experiments. For all samples, both Zn and Te dissolution rates were similar at ~0.07 μmol cm^{-2} hr^{-1}.

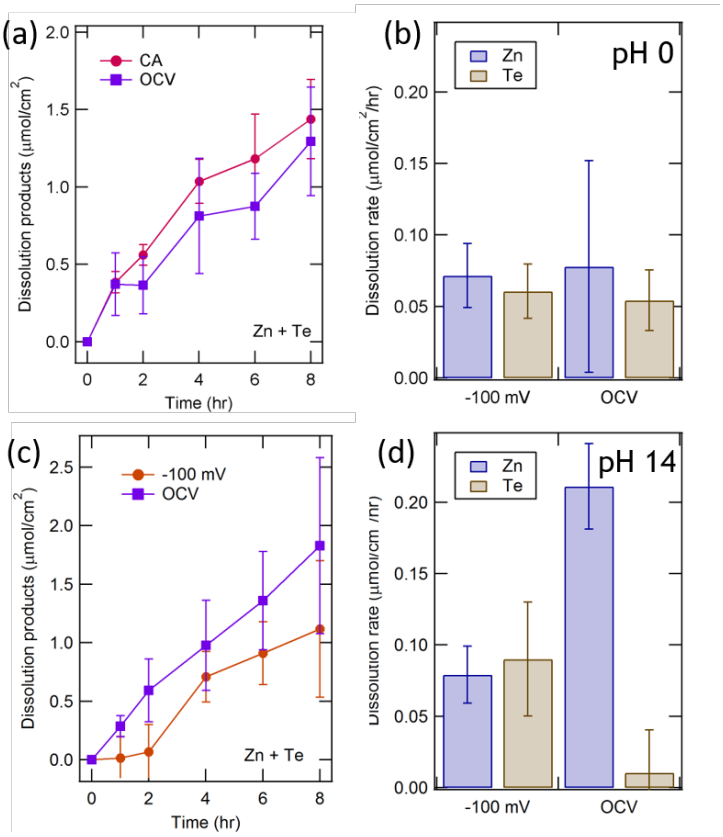

Figure 2.2. Dissolution products of ZnTe (a,c) Concentrations of dissolved Zn, Te species in the working compartment biased at -100 mV vs. RHE and OCV in the dark over 24 hours, normalized to the electrode area in H_2(g)-saturated (a) 1.0 M H_2SO_4(aq) and (b) 1.0 M KOH(aq). (b, d) the dissolution rate for the n-ZnTe electrodes in (b)1.0 M H_2SO_4(aq) and (d) 1.0 M KOH(aq).

Figure 2.2c shows the total dissolution product as a function of time of n-ZnTe electrodes in the dark biased at -100 mV *vs.* RHE ("CA", red) and under OCV (purple) in H_2(g)-saturated 1.0 M KOH(aq) over 8 hours. Similarly to the samples in 1.0 M H_2SO_4(aq), no initial spikes were observed in the first hour. Nevertheless, the total dissolution for the samples under OCV was slightly higher, increasing linearly from 0 to ~1.75 µmol cm^{-2} after 8 hours. The total dissolution concentration for the samples held at -100 mV *vs.* RHE linearly increased from 0 to 1.0 µmol cm^{-2} at 8 hours. Figure 2.2d shows the dissolution rate of Zn and Te species in H_2(g)-saturated 1.0 M KOH(aq). Since the dissolution products

increased linearly from the start, the rates were calculated from the whole time span of the experiments. Both Zn and Te dissolution rates were similar at ~0.08 μmol cm^{-2} hr^{-1} for the samples held under -100 mV *vs.* RHE. On the other hand, the Zn dissolution rate was substantially higher in the samples under OCV at ~0.20 μmol cm^{-2} hr^{-1} compared to ~0.01 μmol cm^{-2} hr^{-1} for Te.

After the electrochemical experiments, all samples were inspected under a scanning electron microscope (SEM) for changes in the surface morphology. Figure 2.3 shows the SEM images of the n-CdTe electrodes (a) before and (b-e) after electrochemical testing. Before the experiments, the n-CdTe electrode had a smooth surface. After being tested for 24 hours under -100 mV *vs.* RHE, the n-CdTe showed small amounts of pits and material deposits (Fig. 2.3b,c). The n-CdTe electrode tested in 1.0 M H_2SO_4(aq) (Fig. 2.3b) showed more pits than the one tested in 1.0 M KOH(aq) (Fig. 2.3c). Nevertheless, both surfaces did not show substantial etched pits. In contrast, n-CdTe samples tested under open-circuit potential contained higher morphology changes. The sample tested in 1.0 M H_2SO_4(aq) contained many microscopic deposits on the surface (Fig. 2.3d). The sample tested under OCV in 1.0 M KOH (aq) had etched pits throughout the surface (Fig. 2.3e).

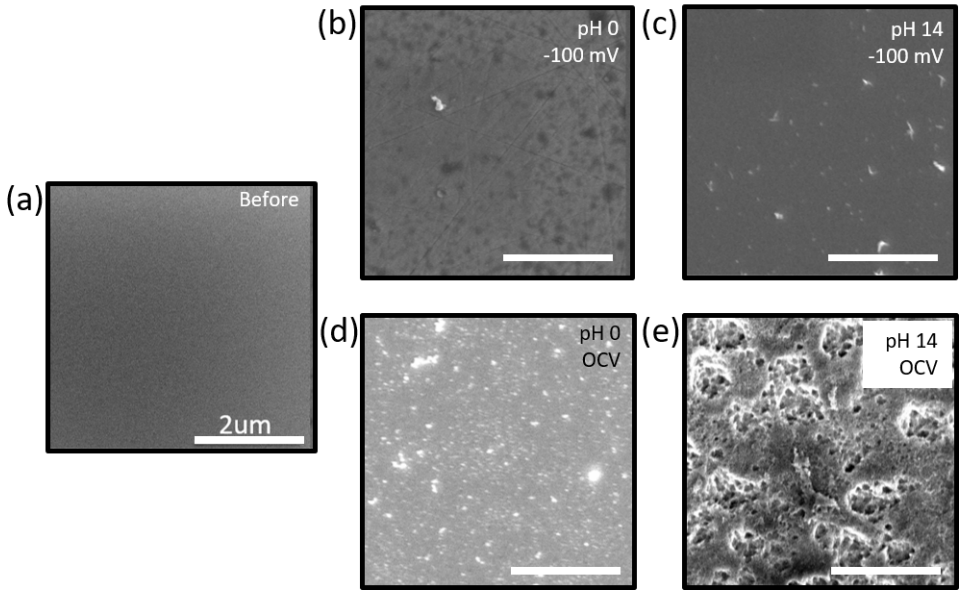

Figure 2.3. SEM images of n-CdTe electrodes (a) before test, and (b-e) after the chronoamperometry (b) biased at -100 mV *vs.* RHE in the dark over 24 hours in 1.0 M H_2SO_4(aq), (c) biased at -100 mV *vs.* RHE in the dark over 24 hours in 1.0 M KOH(aq), (d) under OCV in 1.0 M H_2SO_4(aq), and (e) under OCV in 1.0 M KOH(aq).

Figure 2.4 shows SEM images of the n-ZnTe electrodes (a) before and (b-e) after electrochemical testing. Before the experiments, the n-CdTe electrode had a relatively smooth surface, but still contained microscopic stripes on the surface which are most likely a result of wafer polishing (Fig. 2.4a). All n-ZnTe samples after testing contained some amount of etched pits at varying degrees. After being tested for 8 hours under -100 mV *vs.* RHE in 1.0 M H_2SO_4(aq), the sample developed triangular etched pits thoughout the surface (Fig. 2.4b). The sample tested under applied bias, but in 1.0 KOH (aq) showed fewer numbers of triangular etched pits, but with slightly larger in depth and lateral size (Fig. 2.4c). The sample tested under OCV in 1.0 M H_2SO_4(aq) mostly corroded uniformly throughout with no preferred etched orientation (Fig. 2.4d). The sample tested under OCV in 1.0 KOH (aq) also etched uniformly without any preferred orientation with more particle deposits on the surface.

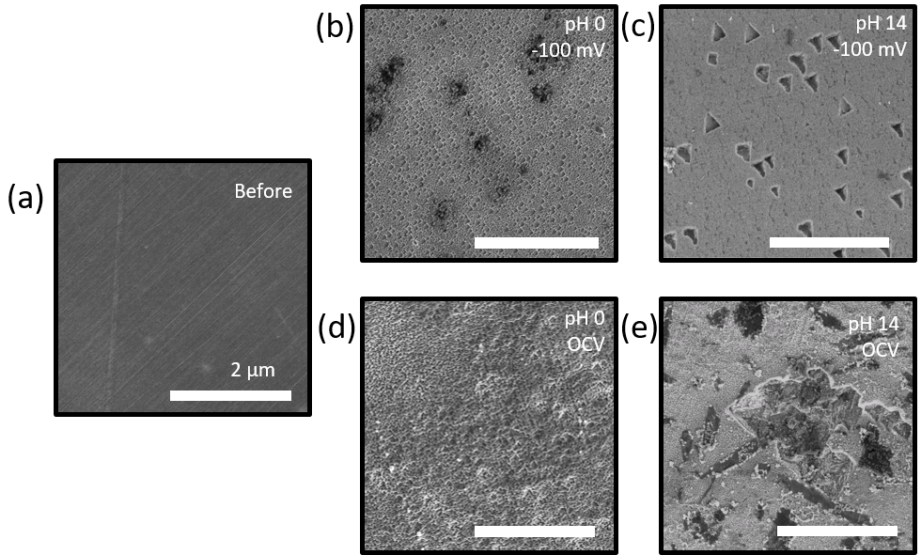

Figure 2.4. SEM images of n-ZnTe electrodes (a) before test, and (b-e) after the chronoamperometry (b) biased at -100 mV *vs.* RHE in the dark over 24 hours in 1.0 M H_2SO_4(aq), (c) biased at -100 mV *vs.* RHE in the dark over 24 hours in 1.0 M KOH(aq), (d) under OCV in 1.0 M H_2SO_4(aq), and (e) under OCV in 1.0 M KOH(aq).

Surface compositions of n-CdTe and n-ZnTe

After the electrochemical operation, the electrodes were disassembled and transferred *ex-situ* to the loading chamber for x-ray photoelectron spectroscopy (XPS). Figure 2.5 shows the Cd 3d (Fig. 2.5a) and Te 3d (Fig. 2.5b) XPS peaks of n-CdTe electrodes (dark) before and after 24-hour electrochemical tests at different conditions. No substantial changes were observed in the Cd 3d spectra. Some shifts in Te 3d peaks were observed. However, the shifts were reported to be very small relative to regular XPS shifts.[15] Before test, n-CdTe showed an elemental Te 3d 5/2 component at 572.8 eV, an elemental Te 3d 3/2 component at 583.1 eV, and a 3d 5/2 peak at 576.1 eV and a 3d 3/2 peak at 586.5 eV corresponding to TeO_2. For the samples tested under OCV in 1.0 M H_2SO_4(aq), the TeO_2 peaks are gone, with only the elemental Te peaks remaining. After biased at -100 mV *vs.* RHE in 1.0 M H_2SO_4(aq), the surface contained small amounts of

TeO_2 peaks and Te^0, similarly to the one before testing. In 1.0 M KOH(aq), the TeO_2 peaks remained in both applied potential and OCV cases. Nevertheless, new peaks at 572.2 eV, corresponding to Te^{2-}, also arose in both conditions. Besides the TeO_2 peaks, the n-CdTe after OCV in 1.0 M KOH(aq) had a Te 3d 5/2 peak at 572.5 eV and a Te 3d 3/2 peak at 583.0 eV which correspond to Te^0 and Te^{2-}.

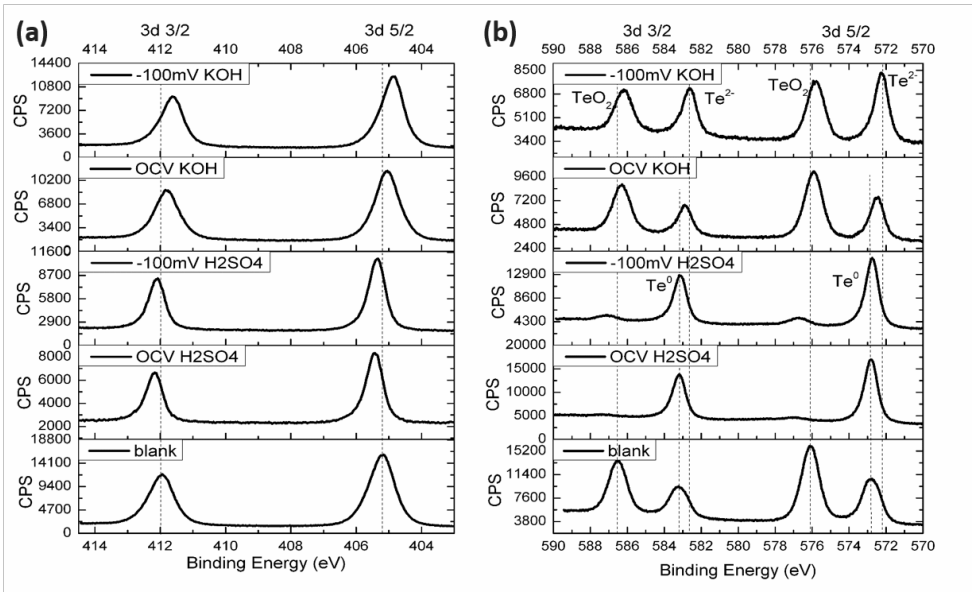

Figure 2.5. XPS of (a) Cd 3d, (b) Te 3d peaks of n-CdTe electrodes (dark). From top to bottom: after 24 hours biased at -100 mV vs. RHE in H_2(g)-saturated 1.0 M KOH(aq); after 24 hours left at open circuit voltage in H_2(g)-saturated 1.0 M KOH(aq); after 24 hours biased at -100 mV vs. RHE in H_2(g)-saturated 1.0 M H_2SO_4(aq); after 24 hours left at open circuit voltage in H_2(g)-saturated 1.0 M H_2SO_4(aq); before electrochemical test.

Similarly, n-ZnTe samples were transferred *ex-situ* to the loading chamber after testing. The Zn 2p XPS peaks were reported to contain little shift between each species.[16] Therefore, only Te 3d peaks were used for the analysis of the surface compositions of n-ZnTe samples. Figure 6 shows Te 3d XPS spectra for the samples tested in (a) 1.0 M H_2SO_4 (aq) and (b) 1.0 M KOH. For the samples in 1.0 M H_2SO_4 (aq), Te^{2-} peak and a small amount of Te-O (Te^{2+}) were observed at 577.5 eV and 582 eV, respectively. After 8 hours of electrochemical testing, more oxidative peaks at 582 eV were observed. On the

other hand, all oxidative peaks were reduced and the surface was only left with Te-Zn peak at 577.5 eV for the sample tested under -100 mV *vs.* RHE (Fig. 2.6a). For 1.0 M KOH (aq), the sample tested under applied potential showed the same surface composition where all the oxide was reduced into the Te-Zn peak. The sample left under OCV, however, contained a slightly shifted Te^0 peak at ~579 eV.

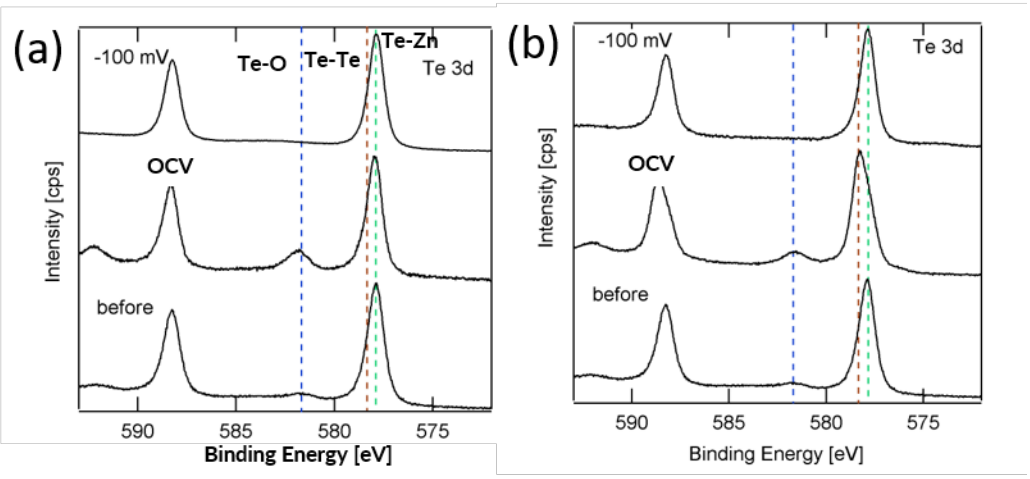

Figure 2.6. XPS of Te 3d peaks of n-ZnTe electrodes (dark) tested in (a) 1.0 M H_2SO_4(aq) and (b) 1.0 M KOH (aq). From top to bottom: after 8 hours biased at -100 mV *vs.* RHE, after 8 hours under OCV, and before electrochemical operation.

Corrosion behaviors of Pt-coated n-CdTe and n-ZnTe

For an analysis of the catalyst on the electrode's corrosion, the samples were coated with sputtered 2-nm layer of Pt before the electrochemical operation. Figure 2.7 shows (a) CdTe and (b) ZnTe dissolution concentrations of the samples held at -100 mV *vs.* RHE in the dark over 24 hours in H_2(g)-saturated 1.0 M KOH(aq). The concentrations were normalized to the electrode areas. The light red and light purple in both Fig. 2.7a and Fig. 2.7b represent the concentrations of the sample without Pt coating. For n-CdTe samples, dissolved Cd concentrations decreased from 0.008 μmol cm^{-2} to ~0 μmol cm^{-2} after 24 hours of testing. Similarly, dissolved Te concentrations decreased from

0.015 µmol cm^{-2} to 0.005 µmol cm^{-2}. On the other hand, both Zn and Te dissolution concentrations in the n-ZnTe stayed approximate at the same level (~0.5 µmol cm^{-2}).

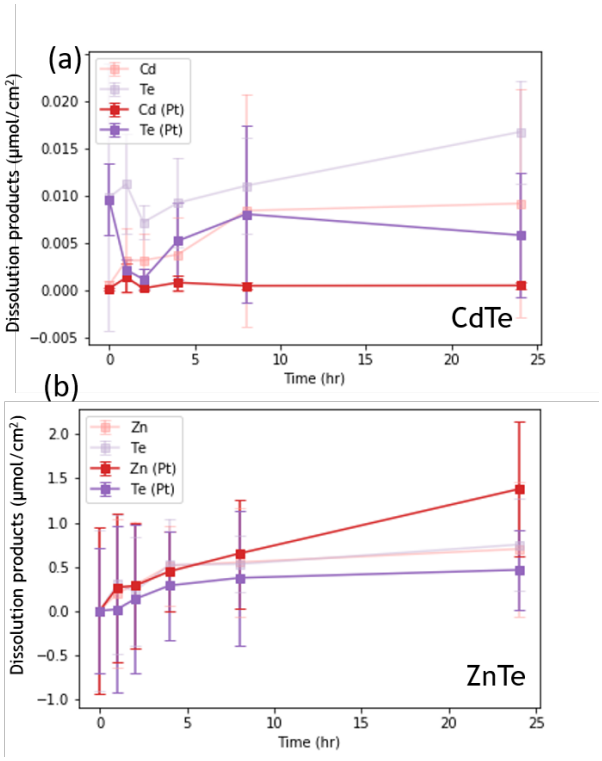

Figure 2.7. Dissolution products as a function of time for Pt-coated (a) CdTe and (b) ZnTe samples held at -100 mV vs. RHE in H_2(g)-saturated 1.0 M H_2SO_4 (aq).

Corrosion behaviors of TiO_2-coated n-ZnTe

Amorphous a-TiO_2 grown with atomic-layer deposition (ALD) was applied to n-ZnTe samples for an analysis of the protection layer. Figure 2.8 shows concentrations of the total dissolution products for a-TiO_2-coated n-ZnTe samples. Figure 8a shows the total dissolution products of bare n-ZnTe samples tested under -100 mV *vs.* RHE (light orange), under OCV (light green), a-TiO_2-coated n-ZnTe samples tested under -100 mV *vs.* RHE (orange), and under OCV (green). Both samples tested under applied bias and OCV showed decreases in the dissolution products after coated with a-TiO_2 (Fig. 2.8a).

Additionally, the total dissolution products can be further reduced by applying 2-nm Pt catalyst overlayer after coated with a-TiO_2 (Fig. 2.8b).

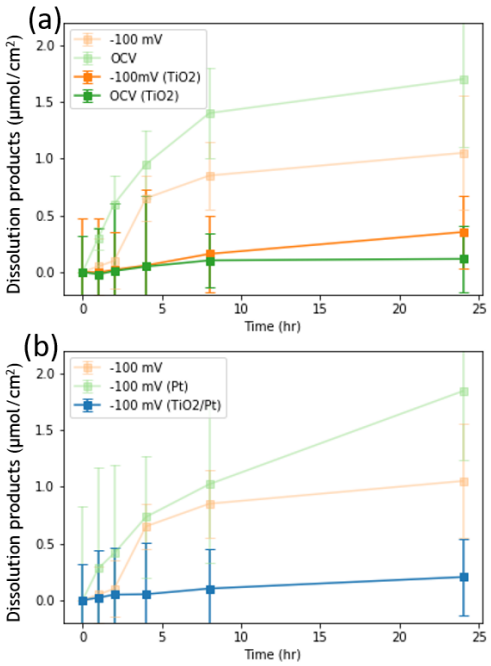

Figure 2.8. Dissolution of protected ZnTe electrodes (a,c) Concentrations of dissolved Zn, Te species in the working compartment biased at -100 mV vs. RHE and OCV in the dark over 24 hours, normalized to the electrode area in H_2(g)-saturated.

Discussion

CdTe has been reported to form a native oxide layer in air, mainly consisting of TeO_2 and $CdTeO_3$, and the thickness of native oxide evolves over time.[17] Chemical etching can obtain a consistent surface layer, and can decrease the surface roughness and remove structural damage resulting from the mechanical polishing process from factory production of CdTe substrates. Bromine/methanol (Br_2/CH_3OH) solutions of various concentrations are used as a common etchant.[18] During the etching process, Br_2 oxidizes the tellurium anions to neutrally charged tellurium, as shown in Equation 1.

$$Br_2 + Te^{2-} \longrightarrow 2Br^- + Te^0 \qquad \text{(Eq. 2.1)}$$

Br_2/CH_3OH etching results in an enrichment of elemental Te at the surface.[19] The enrichment of Te increases the leakage current[20], and the leakage current could potentially lead to a degradation of the semiconductor in photoelectrochemical cells[21]. Passivating the Br_2/CH_3OH etched, Te rich surface with hydrogen peroxide can develop a thin insulating oxide layer and minimize the leakage current.[22] The reaction is shown in Equations 2.2, 2.3, and 2.4. Similar etching steps were also performed on the n-ZnTe samples to remove any residual native oxide layer. Nevertheless, the enrichment of elemental Te^0 was not observed on the n-ZnTe samples (Fig. 6).

$$2H_2O_2 + Te^0 \longrightarrow TeO_2 + 2H_2O \qquad \text{(Eq. 2.2)}$$

$$3H_2O_2 + Te^{2-} + 2H^+ \longrightarrow TeO_2 + 4H_2O \qquad \text{(Eq. 2.3)}$$

$$3H_2O_2 + CdTe \longrightarrow CdTeO_3 + 3H_2O \qquad \text{(Eq. 2.4)}$$

To study the electrochemical stability of n-CdTe, the n-CdTe electrodes were biased at -100 mV vs. RHE for 24 hours (Fig. 2.1). Here, the current densities for all the tested electrodes were in a range of ~ 0.01 mA cm^{-2} in both 1.0 M H_2SO_4 (aq) and 1.0 M

KOH (aq), indicating sluggish HER kinetics on bare n-CdTe and n-ZnTe electrodes in the dark which were expected for bare electrodes without any HER catalysts.

To quantify the faradaic efficiencies of the corrosion, dissolution products were collected during the chronoamperometry measurements and analyzed using Inductively-Coupled Plasma Mass Spectrometry (ICP-MS). If the corrosion reaction was a 2-electron charge transfer corrosion process, the faradaic efficiencies, or the amount of charge transferred in the corrosion process divided by the total amount of charge passed by the potentiostat, would be 2.76% in 1.0 M H_2SO_4(aq), and 0.94% in 1.0 M KOH(aq) for n-CdTe samples. If the corrosion reaction was a 6-electron corrosion process, then the corrosion faradaic efficiencies would be 8.28% and 2.82%, respectively. These low faradaic efficiencies indicate that if the corrosion was electrochemically driven, then only a small portion of the currents came from corrosion, and most of the currents were going toward HER. The corrosion rates are also in good accord with the dissolution rate of the n-CdTe samples at 0.33 nm/h in 1.0 M H_2SO_4(aq), and about 0.10 nm/h in 1.0 M KOH(aq), respectively. In the Pourbaix diagram drawn by Zeng, C. et. al.[22], CdTe remains stable from pH -2 to 14 between 0 and -0.5 V vs. RHE, and in the Pourbaix diagram drawn by Dremlyuzhenko, S. G. et. al.[23], CdTe is in the form of Cd^{2+} + Te at -100 mV vs. RHE from pH -2 to 2, and in the form of CdTe at -100 mV. *vs.* RHE at pH 14. Another calculated Pourbaix diagram is plotted in Fig. S2.3, showing similar species in pH 0 and pH 14 ranges.[23] The CdTe Pourbaix diagram predicts that at -100 mV *vs.* RHE, the following reactions should occur between CdTe and H^+:

$$\text{pH 0:} \qquad CdTe + 2H^+ = H_2Te + Cd^{2+}. \qquad \text{(Eq. 2.5)}$$

Notably, at ~0 V vs. RHE and pH 0, the formation of Te^0 via an oxidation of Te^{2-} anions should occur:

$$\text{pH 0:} \qquad CdTe + 2H^+ = Te^0 + Cd^{2+} + H_2 \qquad \text{(Eq. 2.6)}$$

At E< -0.5 V vs. RHE, the electrochemical reduction of Cd^{2+} cations of CdTe into Cd^0 should occur:

$$\text{pH 0:} \qquad CdTe + 2H^+ + 2e^- = Cd^0 + H_2Te. \qquad \text{(Eq. 2.7)}$$

For pH 14, a stable region of a CdTe phase slightly overlaps with the region of pH 14 at $E<$ 0 V vs. RHE. For E < -0.1 V vs. RHE, the electrochemical reduction of Cd^{2+} cations into Cd^0 should occur as:

$$\text{pH 14:} \qquad CdTe + H_2O + 2e^- = Cd^0 + HTe^- + OH^- . \qquad \text{(Eq. 2.8)}$$

Experimentally, the n-CdTe electrode tested under bias at -100 mV *vs.* RHE in 1.0 M H_2SO_4 (aq) was less stable than in 1.0 M KOH(aq), both from the dissolution results and the change in the surface morphology (Fig. 2.3). The lower stability of the samples in 1.0 M H_2SO_4(aq) is likely caused by the Cd^{2+} ions chemically leaching out from the n-CdTe lattice.

At 0 hour of the blank samples, Cd concentration was close to 0, which agrees with the use of high purity acid or base, confirming no impurity was present in the setup, but Te concentrations were generally higher and contained larger error bars. The larger error is most likely due to both variations in the samples and sensitivity limits of the ICP-MS. In the standard calibration solutions used for ICP-MS, the most diluted standard solution for Cd had a concentration of 0.17 $\pm$ 6.1 μg/L, but for Te, it was 0.80 $\pm$ 46 μg/L. Since the aloquats for the ICP-MS measurements were diluted to 1/5 of the original concentration, Te errors can be magnified by 5 times to 233.464 μg L^{-1}. Nevertheless, this systematic error is small compared to the differences between the concentrations in different experimental conditions.

Since the corrosion faradaic efficiencies were small, less than 10% from previous calculations, to further investigate if the corrosion is driven by electrochemical reactions or chemical reactions, control samples of n-CdTe electrodes were tested at OCV in H_2(g)-saturated 1.0 M H_2SO_4(aq) and 1.0 M KOH(aq). In 1.0 M H_2SO_4 (aq), although the total dissolution products are similar for both OCV and applied potential, the dissolution rates for Cd and Te were different. Under applied potential, the dissolution rate for Cd was higher, and under OCV, the dissolution rate Te was higher (Fig. 2.1). The SEM images also show slightly more deposits on the surface after testing on the samples tested under OCV. Nevertheless, the Te 3d XPS peaks show similar surface composition for both samples.

Thus, Cd^{2+} likely leached out from the lattice under both conditions. However, on the OCV samples, the surface potential could be sufficiently high to allow dissolved Te to precipitate and form small deposits on the surface (Eq. 2.9). On the other hand, in the samples under applied potential, after Cd^{2+} was leached, Te ion in the lattice could react with the solution and form H_2Te (aq) (Eq. 10). High Te^0 in all samples are most likely from the etching step where $CdTeO_3$ from Br_2/CH_3OH etching and H_2O_2 treatment (Eq. 2.4) was reduced to Te^0 by the negative potential. This is in agreement with the Cd peak shifts in XPS (Fig. 2.5a) and the Te^0 on the surface (Fig. 2.5b). TeO_2 and $CdTeO_3$ from surface treatment (Eq. 2.3 and Eq. 2.4) dissolved both in OCV and under -100 mV *vs.* RHE bias, and most of this surface oxide likely dissolved after being in the electrolyte for 1 hour, leading to high dissolution measured by ICP-MS in the first hour.

$$CdTe_{(s)} + 2H^+_{(aq)} \leftrightarrow Cd^{2+}_{(aq)} + Te_{(s)} + H_2 \qquad \text{(Eq. 2.9)}$$

$$CdTe_{(s)} + 2H^+_{(aq)} \leftrightarrow Cd^{2+}_{(aq)} + H_2Te_{(aq)} \qquad \text{(Eq. 2.10)}$$

In 1.0 M KOH(aq), the dissolution of the samples under OCV was similar to that in 1.0 M H_2SO_4 (aq), while the dissolution of the samples under applied potential was substantially lower. For the samples held at OCV, almost all of the dissolution came from Te (Fig. 2.1d). The SEM image also shows much rougher morphology after testing for this sample. Unlike the samples in 1.0 M H_2SO_4, Te 3d XPS peaks representing TeO_x still remained after the testing. Hence, under OCV, the samples likely underwent oxidative corrosion, leaching Te^{2-} from the lattice, while leaving Cd to oxidize and form $Cd_2TeO_{6(s)}$ (Eq. 2.11). For the samples held at -100 mV *vs.* RHE, the dissolution rates for both species were similar. Nevertheless, at this potential, Cd^{2+} was observed to be reduced to Cd^0 (Fig. 2.5). The Te 3d XPS peaks show more Te^{2-} peaks compared to OCV. Hence, in addition to reduction of Cd^{2+} (Eq. 2.12, 2.14), reduction of residual metallic Te on the surface might also occur (Eq. 2.13).

$$3CdTe_{(s)} + 8H_2O + 4OH^- \leftrightarrow Cd_3TeO_{6(s)} + 2TeO_3^{2-}{}_{(aq)} + 10H_2 \qquad \text{(Eq. 2.11)}$$

$$CdTe_{(s)} + 3OH^- \leftrightarrow CdO_2^{2-}{}_{(aq)} + HTe^-{}_{(aq)} + H_2O \quad \text{(Eq. 2.12)}$$

$$Te_{(s)} + H_2 + OH^- \leftrightarrow H_2O_{(l)} + HTe^-{}_{(aq)} \quad \text{(Eq. 2.13)}$$

$$CdTe_{(s)} + H_2 + OH^- \leftrightarrow Cd_{(s)} + HTe^-{}_{(aq)} + H_2O \quad \text{(Eq. 2.14)}$$

For n-ZnTe, the thermodynamic Pourbaix diagram is plotted in Fig. S2.4.[23] The diagram predicts that at E = -0.1 V vs. RHE, the following reactions between ZnTe and H^+/OH^- should occur:

$$\text{pH 0: } ZnTe + 2H^+ = H_2Te + Zn^{2+} \quad \text{(Eq. 2.15)}$$

$$\text{pH 14: } ZnTe + 3OH^- = HTe^- + ZnO_2^{2-} + H_2O. \quad \text{(Eq. 2.16)}$$

At ~0 V vs. RHE and pH 0, the formation of Te^0 via an oxidation of Te^{2-} anions should occur as:

$$\text{pH 0: } ZnTe + 2H^+ = Te^0 + Zn^{2+} + H_2. \quad \text{(Eq. 2.17)}$$

At E< -0.5 V vs. RHE, the electrochemical reduction of Zn^{2+} cations of ZnTe into Zn^0 should occur:

$$\text{pH 0: } ZnTe + 2H^+ + 2e^- = Zn^0 + H_2Te \quad \text{(Eq. 2.18)}$$

$$\text{pH 14: } ZnTe + H_2O + 2e^- = Zn^0 + HTe^- + OH^-. \quad \text{(Eq. 2.19)}$$

Experimentally, unlike n-CdTe samples, all n-ZnTe electrodes sustained constant corrosion through the experiments. For the samples tested in 1.0 M H_2SO_4 (aq), the total dissolution for both samples under applied potential and under OCV increased linearly from 0 at the same rate. The dissolution rates for each species are also similar with Zn dissolution rate slightly higher for both potentials (Fig. 2.2). The SEM images show etched pits developed uniformly throughout the electrode surface (Fig. 2.4). The Te 3d peaks of the samples under both potential conditions are also similar with slightly higher TeO peaks in the samples tested under OCV (Fig. 2.6). Thus, the n-ZnTe electrodes most likely underwent chemical dissolution where Zn^{2+} ions were disassociated from the ZnTe lattice and leached into the solution (Eq. 2.20, 2.21). Although at this potential, the remaining Te^{2-} could be oxidized to form metallic $Te^0{}_{(s)}$ (Eq. 2.20), the dissolution rate of Zn from the

ZnTe was sufficiently high such that the surface morphology changed too fast to allow any $Te_{(s)}$ deposits.

$$ZnTe_{(s)} + 2H^{+}_{(aq)} \leftrightarrow Zn^{2+}_{(aq)} + Te_{(s)} + H_2 \quad \text{(Eq. 2.20)}$$

$$ZnTe_{(s)} + 2H^{+} \leftrightarrow Zn^{2+} + H_2\,Te_{(aq)} \quad \text{(Eq. 2.21)}$$

For the samples tested in 1.0 M KOH (aq), the total dissolution of the samples under OCV was slightly higher. Nevertheless, the electrodes under both conditions still showed similar behaviors with the dissolution increasing linearly from 0 hours (Fig. 2.2). For the samples tested under bias at -100 mV *vs.* RHE, the dissolution rates for both species were similar. The SEM image for this sample shows some triangular etched pits, but not uniformly throughout the surface, indicating one facet of the lattice is more likely to corrode. Nevertheless, the Te 3d XPS peaks show similar surface composition to the samples before testing. Thus, at this lower biased potential, the n-ZnTe electrodes likely either underwent chemical dissolution (Eq. 2.22), or reduced Zn^{2+} to form Zn^0 (Eq. 2.23). The reduction of Zn^{2+}, however, would still likely cause the remaining Te to leach out since the etched pits are a few μm wide (Fig. 2.4). It is unlikely to have preferential etching of one element in micrometer scale.

$$ZnTe_{(s)} + 3OH^{-} \leftrightarrow ZnO_2^{2-}{}_{(aq)} + HTe^{-}_{(aq)} + H_2O \quad \text{(Eq. 2.22)}$$

$$ZnTe_{(s)} + H_2 + OH^{-} \leftrightarrow Zn_{(s)} + HTe^{-}_{(aq)} + H_2O \quad \text{(Eq. 2.23)}$$

For the samples under OCV in 1.0 M KOH(aq), although the total dissolution was similar, the dissolution rate for Zn was substantially higher than the dissolution of Te. The SEM image of the surface also shows severe corrosion on the surface. However, many particle deposits were also observed (Fig. 2.4). Since Zn dissolution was higher, these deposits are most likely $Te_{(s)}$. The Te 3d XPS peaks for this electrode also show a small shift toward $Te^0_{(s)}$, which is in good accord with the hypothesized Te deposits. Thus, under

OCV, the Te^{2-} in the n-ZnTe lattice likely got oxidized and formed $Te^{0}_{(s)}$, and deposited onto the surface (Eq. 2.24).

$$ZnTe_{(s)} + 2OH^{-} \leftrightarrow Te_{(s)} + ZnO_2^{2-} + H_2 \quad \text{(Eq. 2.24)}$$

In 1.0 M H_2SO_4 (aq), both CdTe and ZnTe underwent similar chemical dissolution. Hence, applying catalyst on the surface would not change the corrosion kinetics of the samples, except physically providing additional protective coating. With ~2 nm Pt catalyst applied to samples tested in 1.0 M KOH (aq), the dissolution of Cd and Te was greatly reduced compared to without Pt, with very small corrosion rates close to 0.0 nm/h, indicating that in PEC cells with catalyst, the corrosion of CdTe could be negligible. However, the dissolution of ZnTe samples with 2 nm Pt catalyst still remain at the same level. This is likely because, in n-CdTe, the samples corroded via reduction of Cd^{2+}. When Pt catalyst was applied to the surface, the electrons were more kinetically favorable to drive HER through PT compared to reduction of Cd^{2+}. On the other hand, the corrosion of ZnTe in 1.0 M KOH (aq) is attributed to both reduction of Zn^{2+} and oxidation of Te^{2-}. Therefore, kinetically competing for the reducing electrons on n-ZnTe might be more challenging in 1.0 M KOH (aq).

ZnTe samples were further coated with amorphous a-TiO_2 films. The total dissolution in these samples decreased substantially in both applied potential and OCV conditions. Additionally, once the samples were coated with a-TiO_2, applying Pt still led to low dissolution. Hence, Pt likely does not catalyze oxidative and reductive corrosion of the n-ZnTe samples. Nevertheless, further investigation is still needed to fully understand the interfacial properties and the band energetics of the a-TiO_2-coated ZnTe electrodes.

Conclusion

Corrosion kinetics of CdTe and ZnTe cathodes tested in 1.0 M H_2SO_4 (aq) and 1.0 M KOH (aq) were quantified for the conditions relevant for HER, namely, under biased -100 mV *vs.* RHE and under open-circuit potential. In 1.0 M H_2SO_4 (aq), both CdTe

and ZnTe underwent chemical corrosion with dissolution rates of 0.3 nm hr^{-1} and 0.1 nm hr^{-1} for CdTe under bias and under OCV, and 11 nm hr^{-1} for ZnTe in both conditions. In 1.0 M KOH (aq), CdTe corroded at 0.5 nm hr^{-1} and 1 nm hr^{-1} for under applied bias and OCV, respectively. Under applied potential, Cd^{2+} is reduced to form Cd^{0}. The surface corroded uniformly under OCV. Electrochemical corrosion was also observed in ZnTe samples where the dissolution rates were substantially higher at 13 nm hr^{-1} and 30 nm hr^{-1} for under applied bias and OCV, respectively. Both oxidation of Te^{2-} and reduction of Zn^{2+} are the main corrosion mechanisms for ZnTe in 1.0 M KOH (aq). Pt catalyst overlayer offers a competing pathway for the carrier, reducing corrosion under applied potential, suggesting possible utilization of CdTe as a light-absorbing material for PEC cathodes . On the other hand, protective coating is needed to mitigate corrosion of ZnTe in alkaline solution.

References

(1) Walter, M.; Warren, E. Solar Water Splitting Cells. *Chem. Rev.* **2010**, *110*, 6446–6473.

(2) Tan, M. X.; Laibinis, P. E.; Nguyen, S. T.; Kesselman, J. M.; Stanton, C. E.; Lewis, N. S. Principles and Applications of Semiconductor Photoelectrochemistry. In *Progress in Inorganic Chemistry*; John Wiley & Sons, Inc., 1994; pp 21–144. https://doi.org/10.1002/9780470166420.ch2.

(3) Sun, K.; Saadi, F. H.; Lichterman, M. F.; Hale, W. G.; Wang, H.-P.; Zhou, X.; Plymale, N. T.; Omelchenko, S. T.; He, J.-H.; Papadantonakis, K. M.; Brunschwig, B. S.; Lewis, N. S. Stable Solar-Driven Oxidation of Water by Semiconducting Photoanodes Protected by Transparent Catalytic Nickel Oxide Films. *Proc. Natl. Acad. Sci. U. S. A.* **2015**, *112* (12), 3612–3617.

(4) Sun, K.; McDowell, M. T.; Nielander, A. C.; Hu, S.; Shaner, M. R.; Yang, F.; Brunschwig, B. S.; Lewis, N. S. Stable Solar-Driven Water Oxidation to O_2 (g) by Ni-Oxide-Coated Silicon Photoanodes. *J. Phys. Chem. Lett.* **2015**, *6* (4), 592–598. https://doi.org/10.1021/jz5026195.

(5) Luo, J.; Steier, L.; Son, M.-K.; Schreier, M.; Mayer, M. T.; Grätzel, M. Cu_2O Nanowire Photocathodes for Efficient and Durable Solar Water Splitting. *Nano Lett.* **2016**, *16* (3), 1848–1857. https://doi.org/10.1021/acs.nanolett.5b04929.

(6) Zhao, J.; Cai, L.; Li, H.; Shi, X.; Zheng, X. Stabilizing Silicon Photocathodes by Solution-Deposited Ni–Fe Layered Double Hydroxide for Efficient Hydrogen Evolution in Alkaline Media. *ACS Energy Lett.* **2017**, *2* (9), 1939–1946. https://doi.org/10.1021/acsenergylett.7b00597.

(7) Bae, D.; Shayestehaminzadeh, S.; Thorsteinsson, E. B.; Pedersen, T.; Hansen, O.; Seger, B.; Vesborg, P. C. K.; Ólafsson, S.; Chorkendorff, I. Protection of Si Photocathode Using TiO_2 Deposited by High Power Impulse Magnetron Sputtering for H_2 Evolution in Alkaline Media. *Sol. Energy Mater. Sol. Cells* **2016**, *144*, 758–765. https://doi.org/10.1016/j.solmat.2015.10.020.

(8) Hu, S.; Xiang, C.; Haussener, S.; Berger, A. D.; Lewis, N. S. An Analysis of the Optimal Band Gaps of Light Absorbers in Integrated Tandem Photoelectrochemical Water-Splitting Systems. *Energy Environ. Sci.* **2013**, *6* (10), 2984. https://doi.org/10.1039/c3ee40453f.

(9) Benck, J. D.; Lee, S. C.; Fong, K. D.; Kibsgaard, J.; Sinclair, R.; Jaramillo, T. F. Designing Active and Stable Silicon Photocathodes for Solar Hydrogen Production Using Molybdenum Sulfide Nanomaterials. *Adv. Energy Mater.* **2014**, *4* (18), 1400739. https://doi.org/10.1002/aenm.201400739.

(10) Ohashi, K.; McCann, J.; Bockris, J. M. Stable Photoelectrochemical Cells for the Splitting of Water. *Nature* **1977**, *266* (5603). https://doi.org/10.1038/266610a0.

(11) Jang, Y. J.; Lee, J.; Lee, J.; Lee, J. S. Solar Hydrogen Production from Zinc Telluride Photocathode Modified with Carbon and Molybdenum Sulfide. *ACS Appl. Mater. Interfaces* **2016**, *8* (12), 7748–7755. https://doi.org/10.1021/acsami.5b07575.

(12) Su, J.; Minegishi, T.; Domen, K. Efficient Hydrogen Evolution from Water Using CdTe Photocathodes under Simulated Sunlight. *J. Mater. Chem. A* **2017**. https://doi.org/10.1039/C7TA03761A.

(13) Ohashi, K.; Uosaki, K.; Bockris, J. O. Cathodes For Photodriven Hydrogen Generators: ZnTe and CdTe. *Int. J. Energy Res.* **1977**, *1* (1), 25–30. https://doi.org/10.1002/er.4440010104.

(14) Saadi, F. H.; Carim, A. I.; Verlage, E.; Hemminger, J. C.; Lewis, N. S.; Soriaga, M. P. CoP as an Acid-Stable Active Electrocatalyst for the Hydrogen-Evolution Reaction: Electrochemical Synthesis, Interfacial Characterization and Performance Evaluation. *J. Phys. Chem. C* **2014**, *118* (50), 29294–29300. https://doi.org/10.1021/jp5054452.

(15) Swartz, W. E.; Wynne, K. J.; Hercules, D. M. X-Ray Photoelectron Spectroscopic Investigation of Group VIA Elements. *Anal. Chem.* **1971**, *43* (13), 1884–1887. https://doi.org/10.1021/ac60307a044.

(16) Biesinger, M. C.; Lau, L. W. M.; Gerson, A. R.; Smart, R. S. C. Resolving Surface

Chemical States in XPS Analysis of First Row Transition Metals, Oxides and Hydroxides: Sc, Ti, V, Cu and Zn. *Appl. Surf. Sci.* **2010**, *257* (3), 887–898. https://doi.org/10.1016/j.apsusc.2010.07.086.

(17) Zázvorka, J.; Franc, J.; Beran, L.; Moravec, P.; Pekárek, J.; Veis, M. Dynamics of Native Oxide Growth on CdTe and CdZnTe X-Ray and Gamma-Ray Detectors. *Sci. Technol. Adv. Mater.* **2016**, *17* (1), 792–798. https://doi.org/10.1080/14686996.2016.1250105.

(18) Babar, S.; Sellin, P. J.; Watts, J. F.; Baker, M. A. An XPS Study of Bromine in Methanol Etching and Hydrogen Peroxide Passivation Treatments for Cadmium Zinc Telluride Radiation Detectors. *Appl. Surf. Sci.* **2013**, *264*, 681–686. https://doi.org/10.1016/j.apsusc.2012.10.095.

(19) Kotina, I. M.; Tukhkonen, L. M.; Patsekina, G. V.; Shchukarev, A. V.; Gusinskii, G. M. Study of CdTe Etching Process in Alcoholic Solutions of Bromine. *Semicond. Sci. Technol.* **1998**, *13* (8), 890–894. https://doi.org/10.1088/0268-1242/13/8/011.

(20) Bensalah, H.; Plaza, J. L.; Crocco, J.; Zheng, Q.; Carcelen, V.; Bensouici, A.; Dieguez, E. The Effect of Etching Time on the CdZnTe Surface. *Appl. Surf. Sci.* **2011**, *257* (10), 4633–4636. https://doi.org/10.1016/j.apsusc.2010.12.103.

(21) Nandjou, F.; Haussener, S. Degradation in Photoelectrochemical Devices: Review with an Illustrative Case Study. *J. Phys. D. Appl. Phys.* **2017**, *50* (12). https://doi.org/10.1088/1361-6463/aa5b11.

(22) Özsan, M. E.; Sellin, P. J.; Veeramani, P.; Hinder, S. J.; Monnier, M. L. T.; Prekas, G.; Lohstroh, A.; Baker, M. A. Chemical Etching and Surface Oxidation Studies of Cadmium Zinc Telluride Radiation Detectors. *Surf. Interface Anal.* **2010**, *42* (6–7), 795–798. https://doi.org/10.1002/sia.3146.

(23) Jain, A.; Ong, S. P.; Hautier, G.; Chen, W.; Richards, W. D.; Dacek, S.; Cholia, S.; Gunter, D.; Skinner, D.; Ceder, G.; Persson, K. A. Commentary: The Materials Project: A Materials Genome Approach to Accelerating Materials Innovation. *APL Mater.* **2013**, *1* (1), 011002. https://doi.org/10.1063/1.4812323.

Supporting Information

Experimental Methods

Materials and Chemicals

n-CdTe(111) wafers with a carrier concentration 5.5 x 10^{17} cm^{-3} were purchased from JX Nippon Minging and Metals Corporation. All the other chemicals were used as received, including sulfuric acid (H_2SO_4, BDH ARISTAR® ULTRA, 93-98%, ultrapure for trace metal analysis), potassium hydroxide (KOH, Acros Organics, 99.98%, trace metal basis), bromine (Br_2, Sigma-Aldrich, ≥99.99% trace metals basis), methanol (CH_3OH, ≥99.8% ACS, VWR Chemicals), and hydrogen peroxide solution (H_2O_2, 30 % w/w in H_2O, Sigma-Aldrich). Deionized H_2O with a resistivity of ≥18 MΩ·cm was obtained from a Barnstead Nanopure station (Thermo Scientific). A platinum target (Pt, Kurt J Lesker, 99.99%) was used in Pt deposition.

Electrode Preparation

CdTe pieces were cut from an n-CdTe(111) wafer that had been polished in factory. Then the back was soldered with In to make electrical contact. Pieces were etched for 30 s in a freshly prepared solution of 0.2%(v/v) Br_2 /CH_3OH, then rinsed vigorously with CH_3OH and dried with N_2, followed by 15 seconds exposure in 30 wt.% H_2O_2, then rinsed vigorously with water and dried with N_2, and immersed in CH_3OH until being dried with a stream of N_2(g) before use. Pt deposition was performed in a sputterer (AJA International) with a base pressure of < 10^{-6} torr under an Ar atmosphere at 5 mTorr using RF power. ~2 nm of Pt was deposited onto the front side of the prepared CdTe substrate.

The samples were scratched with Ga-In eutectic (Sigma Aldrich, 99.99%) onto the back, followed by use of Ag paint (SPI Supplies) to attach to a Cu wire (McMaster-Carr). The wire was threaded through a glass tube (Corning Incorporation, Pyrex tubing, 7740 glass). The area around the wire and the sample was coated with non-conductive epoxy (Hysol 9460) and allowed to dry overnight. Electrode areas were imaged using a high-

resolution optical scanner (Epson perfection V370 with a resolution of 2400 psi) and then analyzed by ImageJ software.

Electrochemical measurements

Electrochemical measurements were conducted in a home-made dark box in a custom two-compartment electrochemical cell with a membrane separating the working electrode (with the reference electrode) from the counter electrode. A Nafion membrane was used for measurements in 1.0 M H_2SO_4(aq) and an anion exchange membrane (AEM) was used for measurements in 1.0 M KOH(aq). Each compartment contained 25 mL electrolyte which was filled by a pipette (Fisher Scientific, 5mL). The electrochemical cell was cleaned with aqua regia, rinsed thoroughly with H_2O, dried in an oven, and cooled in air before use.

A carbon rod (Alfa Aesar, ≥99.9995%, metals basis) placed in a fritted glass tube (Aceglass Inc., gas dispersion tube Pro-D) was used as the counter electrode. A mercury/mercurous sulfate ($Hg/HgSO_4$ in saturated K_2SO_4(aq), CH Instruments, CH151) electrode and a mercury/mercury oxide (Hg/HgO in 1.0 M KOH(aq), CH Instruments, CH152) electrode were used as the reference electrode in 1.0 M H_2SO_4(aq) and in 1.0 M KOH(aq), respectively.

All the electrochemical data were collected on a MPG-2 multichannel potentiostat or a SP-200 potentiostat (BioLogic Science Instruments). Prior to the measurements, the electrolyte was purged with H_2(g) for 30 min to saturate H_2(g) and remove O_2(g). During the measurements, H_2(g) bubbling was maintained to keep a saturated H_2(g) and O_2(g)-free environment. Vigorous stirring was kept before and during the measurements since the H_2(g) purge started, using a magnetic stir bar driven by a model-train motor (Pittman). Chronoamperometric (CA) measurements were performed at a constant potential at -100 mV vs. reversible hydrogen electrode (RHE). Open Circuit Voltage (OCV) measurements were performed with no potential applied to the working electrode. Each electrochemical experiment was run for 24 hours. At 0, 1, 2, 4, 8, and 24 hours of each experiment, 1 mL solution was taken out from the working compartment by a pipette (Fisher Scientific,

1000μL) for further analysis by ICP-MS. The sample taken at 0 hour was after a 30 min purge of H_2(g) and right before the working electrode was put into the cell. After the samples were taken out, no solution was added to the compartment.

Atomic-Layer Deposition (ALD) of TiO_2 Thin Films

a-TiO_2 films were grown using tetrakis(dimethylamido)-titanium (TDMAT). For TiO_2 films prepared from the TDMAT precursor, a Cambridge Nanotech S200 or Oxford Instruments FlexAL ALD system was used for deposition outside and inside the cleanroom. Each ALD cycle consisted of a 0.10 s exposure to TDMAT (Sigma-Aldrich, 99.999%), a N_2(g) (Airgas, 99.999%) purge, a 0.015 s exposure to H_2O, and a final N_2(g) purge. Research grade 20 sccm N_2(g) was used for the N_2(g) purges, and each N_2(g) purge was 15 s in duration. During the deposition, the substrate and the TDMAT precursor were heated to 150 °C and 75 °C, respectively, while the H_2O remained at room temperature. Most samples were prepared with 400 cycles and 1000 ALD cycles, producing a nominal thickness of 22 nm and 55 nm, respectively. The film thickness and refractive index were measured via spectroscopic ellipsometry (J.A. Woollam Co., alpha-SE) and were fit to a Cauchy model.

Inductively-coupled plasma mass spectrometry (ICP-MS) analysis

Inductively coupled plasma mass spectrometry (ICP-MS) data were collected on an Agilent 8800 Triple Quadrupole ICP-MS system. Calibration solutions were prepared by diluting the multi-element standard solutions with deionized water. The solution samples were collected from the electrochemical experiments. Acidic samples were diluted from 1 mL to 5 mL using the deionized water, and alkaline samples were diluted from 1 mL to 5 mL with 2 mL 1.0 M H_2SO_4(aq) and 2 mL H_2O to make it acidic and appropriate for ICP-MS. The total amount of the dissolved Zn, Cd, and Te species respectively in the working compartment at different hours was calculated by the ICP-MS results with the adjustment of volumes being taken into account. Then this amount was normalized to the geometric electrode area for comparison and was used to calculate the corrosion rate in thicknesses.

The faradaic efficiencies of the cathodic corrosion was calculated by dividing the charges transferred in the corrosion process by the total charges passed in the electrochemical experiment.

Scanning-electron microscopy (SEM)

Scanning-electron microscopy (SEM) was performed using a FEI Nova NanoSEM 450 at an accelerating voltage of 5 kV with a working distance of 5 mm.

X-ray photoelectron spectroscopy (XPS)

X-ray photoelectron spectroscopy (XPS) data were collected using a Kratos Axis Nova system with a base pressure of $< 2\times10^{-9}$ Torr. A monochromatic Al Kα source was used to irradiate the sample with X-rays with an energy of 1486.7 eV at a power of 450 W. A hemispherical analyzer oriented for detection along the sample surface normal was used for maximum depth sensitivity. High-resolution spectra were acquired at a resolution of 50 meV with a pass energy of 10 eV.

Supporting Figures

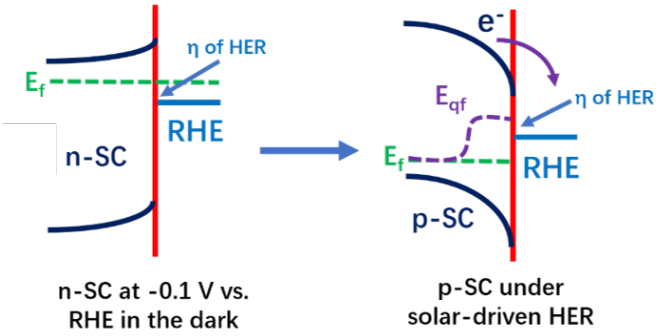

Figure S2.1. Band diagram of n-type semiconductors in dark (left) and p-type semiconductors under illumination (right).

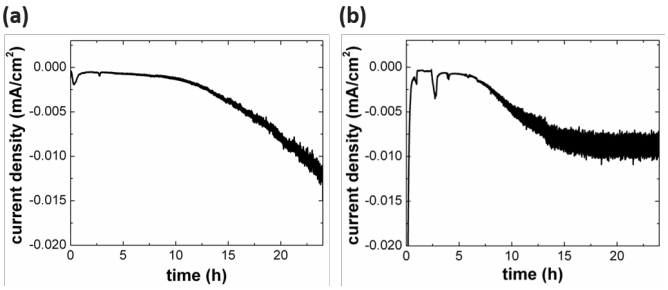

Figure S2.2. Chronoamperometry (current density vs. time) for the n-CdTe electrodes (dark) biased at -100 mV vs. RHE over 24 hours in H_2(g)-saturated (a) 1.0 M H_2SO_4(aq); (b) 1.0 M KOH(aq).

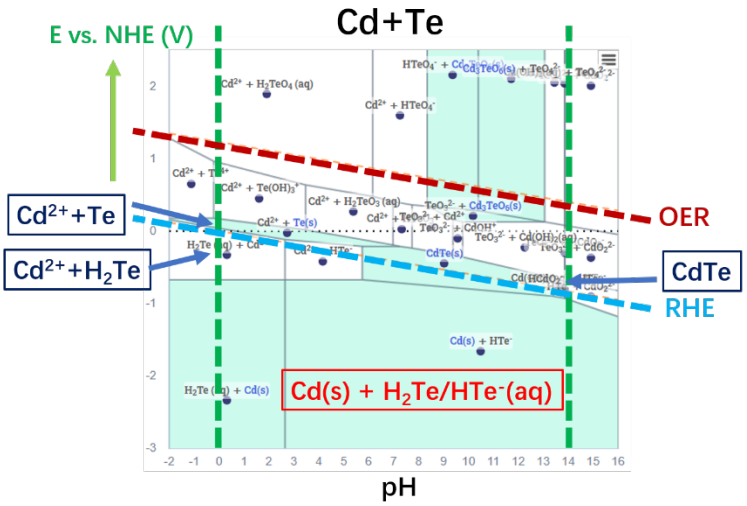

Figure S2.3. Thermodynamics Pourbaix diagram of CdTe in aquoes solution. Vertical green dashes represent the potential for 1.0 M H_2SO_4 (aq) and 1.0 M KOH (aq).

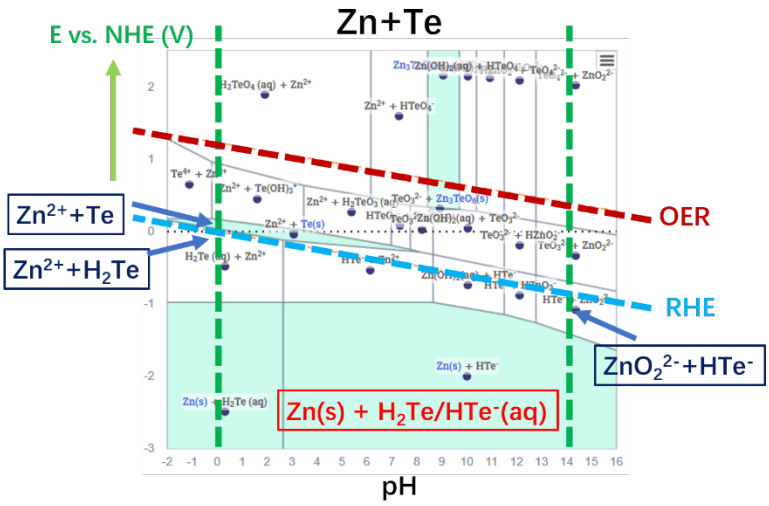

Figure S2.4. Thermodynamics Pourbaix diagram of ZnTe in aqueous solution. Vertical green dashes represent the potential for 1.0 M H_2SO_4 (aq) and 1.0 M KOH (aq).

Chapter 3

FAILURE MODES OF PROTECTION LAYERS PRODUCED BY ATOMIC LAYER DEPOSITION OF AMORPHOUS TIO_2 ON GaAs ANODES

The following chapter discusses the main short-term failure modes for amorphous ALD TiO_2 on GaAs substrates.

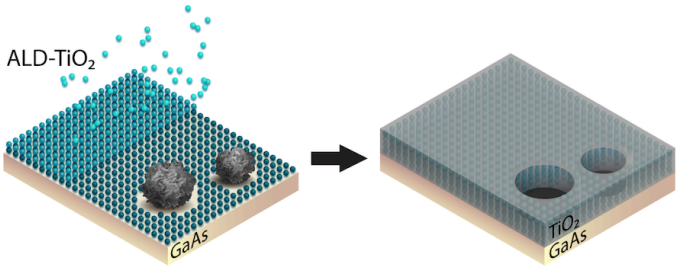

Content in this chapter is drawn from the following publication:

- **Buabthong, P.**, Ifkovits, Z. P., Kempler, P. A., Chen, Y., Nunez, P. D., Brunschwig, B. S., Papadantonakis, K. M., Lewis, N. S. "Failure Modes of Protection Layers Produced by Atomic Layer Deposition of Amorphous TiO_2 on GaAs Anodes." *Energy Environ. Sci.* (2020) **13**, 4269-427.

Abstract

Amorphous titanium dioxide (a-TiO_2) films formed by atomic layer deposition can serve as protective coatings for semiconducting photoanodes in water-splitting cells using strongly alkaline aqueous electrolytes. Herein, we experimentally examine the mechanisms of failure for p^+-GaAs anodes coated with a-TiO_2 films (GaAs/a-TiO_2). Galvanic displacement of exposed GaAs by Au allowed imaging of pinholes in the a-TiO_2 coatings, and enabled collection of quantitative and statistical data associated with pinhole defects. A combination of imaging, electrochemical measurements, and quantitative analyses of corrosion products indicated that extrinsic pinholes were present in the a-TiO_2 films before electrochemical operation. During electrochemical operation, these pinholes led to pitting corrosion of the underlying GaAs substrate. The dominant source of pinholes was the presence of atmospheric particulate matter on the GaAs surface during deposition of the a-TiO_2 layer. The pinhole density decreased substantially when the thickness of the a-TiO_2 coating increased beyond 45 nm, and approached zero when the thickness of the film exceeded 112 nm. The density of pinholes in films thinner than 45 nm decreased when the a-TiO_2 coating was deposited in an environmentally controlled cleanroom. Pinhole-free GaAs/a-TiO_2 devices were also tested via chronoamperometry to quantify the rate of pinhole formation during electrochemistry. The time-to-failure increased with thickness, suggesting that the failure mechanism may involve diffusion or migration through the film. However, other mechanisms may also contribute to the degradation of thicker films (> 112 nm). Nevertheless, as previously hypothesized, extrinsic pinhole defects formed during deposition and testing control the short-term protective performance of the a-TiO_2 film for GaAs anodes evolving O_2 from water.

Introduction

Thick (~100 nm) films of amorphous-TiO_2 (a-TiO_2) formed by atomic layer deposition have emerged as promising protective coatings for semiconducting photoanodes in photoelectrochemical (PEC) water-splitting and CO_2-reduction cells that contain strongly alkaline aqueous electrolytes.[1–4] a-TiO_2 coatings stabilize semiconducting photoanodes that form passivating surface oxides under water-oxidation conditions, such as Si and InP, as well as Group III-V materials that corrode by dissolving under water-oxidation conditions, such as GaAs and GaP.[1,5] The ability to stabilize materials that corrode by dissolution distinguishes a-TiO_2 from many other photoanode protection strategies and allows for the fabrication of III-V stacks of high efficiency monolithic tandem light absorbers. These tandem light absorbers are envisioned as the core of integrated solar fuels systems. Although a-TiO_2 films substantially increase the stability of water-splitting and CO_2-reduction cells with III-V photoanodes, their performance nevertheless degrades over time as manifested by a decrease in photocurrent density accompanied by corrosion of the substrate.[1,5,6] This degradation process has been hypothesized to result from pinhole defects that form during the deposition of the ALD films and/or during electrochemical operation of the electrodes protected by the ALD films.[5–7] Additionally, diffusion of OH^- through ALD a-TiO_2 films during PEC operation has been proposed as a mechanism for the formation of pinholes in a-TiO_2.[8,9]

Pinholes or other extrinsic defects formed during the deposition of a-TiO_2 on III-V or Group IV semiconductors have not yet been imaged, characterized, or quantified. Pinholes have not been observed by scanning-electron microscopy (SEM) or atomic force microscopy (AFM) in freshly prepared thick coatings of a-TiO_2. Furthermore, plan-view images do not provide information on whether surface defects span the entire thickness of the film. If pinhole defects are the primary cause of failure of a-TiO_2 protective coatings, the ability to image and quantify pinhole defects is important for assessment of potential mitigation strategies to reduce the occurrence of pinholes in the films.

Pinhole defects formed in Al_2O_3 coatings during the ALD process have been studied for applications such as gas-diffusion barriers,[10] corrosion-resistant coatings,[11] and high-K gate dielectrics.[12] The origin of the pinholes is ascribed to the nature of the manufacturing process.[13] Pinholes in thicker films (> 10 nm) typically arise from extrinsic contamination of the substrate, whereas pinholes in thinner films (< 10 nm) typically are due to the ALD process itself, particularly inefficient nucleation.[14] Analysis of microscopic pinhole defects in ALD layers is accomplished by first decorating the defects to amplify their visibility in subsequent imaging techniques. Examples of techniques used to amplify the visibility of defects include oxygen-plasma etching of the substrate,[15] electroplating metal,[16] or fluorescent tagging.[17] These techniques require that the film being studied is insulating, as is the case for Al_2O_3, and that the substrate is either conductive or a polymer, neither of which are applicable to III-V photoanodes coated with thick, a-TiO_2 protection layers.

Electroless gold deposition provides a simple process to deposit metallic contacts on functioning III-V semiconductor devices.[18] In the electroless process, the reduction of Au^{3+} in solution is paired to oxidation of the GaAs substrate. Consequently, galvanic displacement of GaAs by Au should provide high selectivity for the deposition of Au at sites where the GaAs substrate is exposed by film-spanning pinholes in thick, a-TiO_2 coatings, and should moreover provide a means to amplify the visibility of the defects by SEM.

Herein, we provide a detailed investigation of the stability of p^+-GaAs anodes protected by thick, a-TiO_2 coatings formed by (GaAs/a-TiO_2) in contact with 1.0 M KOH(aq). We demonstrate that galvanic displacement by Au is a useful technique to decorate pinholes, and use the technique to quantify the pinholes in the films and their dependence on the thickness of the a-TiO_2 film and the sample-preparation environment. We also examine the stability of a-TiO_2 films that were initially pinhole-free as indicated by the galvanic displacement and staining method.

Results and Discussion

Corrosion of p^+-GaAs/a-TiO_2

For analysis of the onset potential for oxygen evolution, 2 nm of Ni was sputtered onto the surface of GaAs/a-TiO_2 electrodes prior to electrochemical testing. Figure 3.1a shows the current density vs. potential behavior of a bare p^+-GaAs electrode in contact with 1.0 M KOH(aq) in the dark. As the potential (E) was swept positive of 0.6 V vs. the reversible hydrogen electrode (RHE), the current density (J) increased from ~ 0 mA cm^{-2} to > 100 mA cm^{-2}. The observation of substantial current densities at $E < E°(O_2/H_2O)$ is consistent with corrosive dissolution of the GaAs electrode. Figure 3.1b compares representative J-E behavior for p^+-GaAs electrodes coated with a-TiO_2-2000x (2000 ALD cycles) and 2 nm of Ni (GaAs/a-TiO_2-2000x/Ni) in contact with 1.0 M KOH(aq). Two types of electrochemical behavior were observed for the p^+-GaAs/a-TiO_2-2000x/Ni electrodes: (i) negligible change in J until the Ni redox peaks appeared at E ~ 1.4 V versus RHE, followed by a steep rise in J near E ~ 1.5 V due to the onset of water oxidation, and (ii) a steep rise in J to > 10 mA cm^{-2} near E = 0.6 V versus RHE, with J relatively constant for the rest of the anodic sweep. Similar electrochemical behaviors were also observed on the electrodes prepared without Ni (Fig. S3.1), with the only differences being the absence of Ni redox peaks and water oxidation, suggesting that Ni does not substantially influence the corrosion kinetics of GaAs.

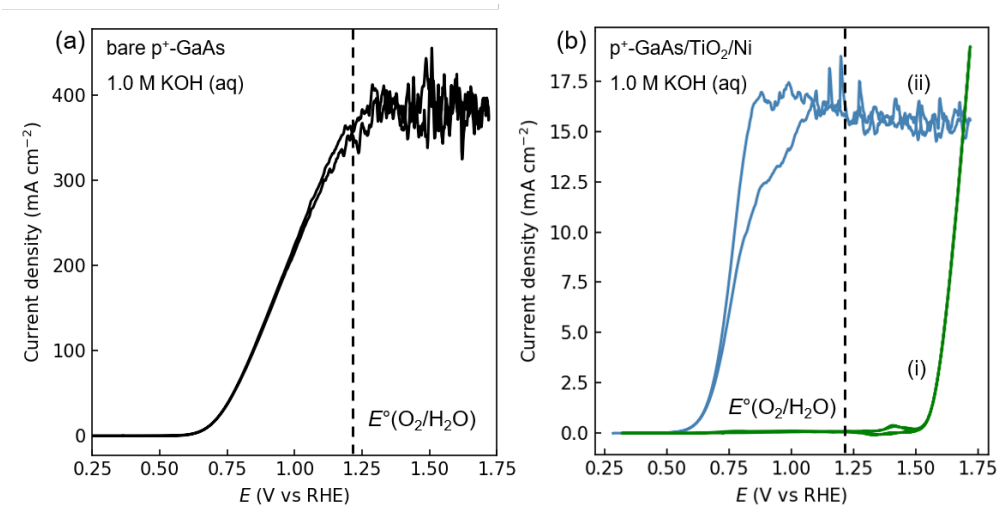

Figure 3.1. Current density vs. potential (*J*-*E*) behavior of (a) bare p^+-GaAs and (b) two different p^+-GaAs samples coated with a-TiO_2-2000x (2000 ALD cycles) and sputtered Ni (GaAs/a-TiO_2-2000x/Ni). The scan rate was 40 mV s^{-1}. Two types of electrochemical behavior were observed for the GaAs/a-TiO_2-2000x/Ni samples prepared similarly: (i) no apparent corrosion current and (ii) substantial corrosion currents.

For the analysis of a-TiO_2 degradation, a-TiO_2-coated p^+-GaAs (with no Ni) substrates were used to minimize possible effects from the Ni overlayer that could confound interpretation of the corrosion kinetics of a-TiO_2, such as loss of catalyst or the Ni film forming an additional protective coating to the a-TiO_2. In an alkaline solution, GaAs substrates at open-circuit undergo dissolution:

$$GaAs_{(s)} + 10OH^-_{(aq)} \rightarrow GaO_3^{3-}{}_{(aq)} + AsO_2^-{}_{(aq)} + 6e^- + 5H_2O_{(l)} \quad \text{(Eq. 3.1)}$$

$$6H_2O_{(l)} + 6e^- \rightarrow 3H_{2(g)} + 6OH^-_{(aq)}. \quad \text{(Eq. 3.2)}$$

Figure 3.2a–c shows *J* as a function of time for a bare p^+-GaAs electrode as well as for two different p^+-GaAs/a-TiO_2-1000x electrodes held at E = 1.13 V vs. RHE in contact with 1.0 M KOH(aq). Figure 3.2d–f shows the concentration of dissolved Ga and As species in the electrolyte, as measured using ICP-MS, during the chronoamperometry experiments shown in Figure 3.2a–c and the expected corrosion calculated based on the

charge passed and six-electron oxidation of As as described in Eq. 3.1. Figure 3.2g–i shows scanning-electron micrographs (SEMs) of the electrode surfaces after the chronoamperometry experiments shown in Figure 3.2a–c.

For the bare GaAs electrode, J was initially 350 mA cm^{-2} and varied substantially with time, but remained > 100 mA cm^{-2} throughout the 30 min experiment (Fig. 3.2a). The concentrations of both Ga and As species in the electrolyte increased linearly and stoichiometrically with time; the concentration of Ga and As species reached 900.2 ± 9.1 and 908.3 ± 8.1 μmol cm^{-2}, respectively, after 30 min of operation, in accord with the expected dissolution (Fig. 3.2d). After testing, the surface appeared roughened, but not pitted (Fig 3.2g). Thus, the bare GaAs electrode corroded uniformly during the 30 min at E = 1.13 V versus RHE while in contact with 1.0 M KOH (aq). The variability in the current density observed over time likely resulted from changes in the active surface area of the GaAs during corrosion.

For a p^+-GaAs/a-TiO_2-1000x electrode that exhibited electrochemical behavior similar to type (i) in Figure 3.1b, J was ~ 0 mA cm^{-2} and remained constant through the 30 min of operation, although some transient peaks in current density that occurred during the brief obstruction of the electrode surface by bubbles in the electrolyte were observed (Fig. 3.2b). The concentrations of both Ga and As species in the electrolyte remained below the detection limit throughout the 30 min experiment (Fig. 3.2e), and the surface appeared unchanged after operation (Fig. 3.2h). Thus, no corrosion was evident after 30 min for this type of GaAs/a-TiO_2-1000x electrode.

For a p^+-GaAs/a-TiO_2-1000x electrode that exhibited type (ii) electrochemical behavior is shown in Figure 1b; J was initially ~1 mA cm^{-2} but increased approximately linearly with time to ~3 mA cm^{-2} after 30 min of operation (Fig. 3.2c). The concentrations of Ga and As species in the electrolyte increased with time but remained ~100 times smaller than concentrations observed for the bare GaAs electrode, reaching 6.2 ± 0.4 μmol cm^{-2} for Ga and 5.5 ± 0.5 μmol cm^{-2} for As, in accord with the amount of

dissolution calculated based on the charge passed and Eq. 3.1 (Fig. 3.2f). After 30 min of operation, the electrode showed evidence of pitting (Fig 3.2i).

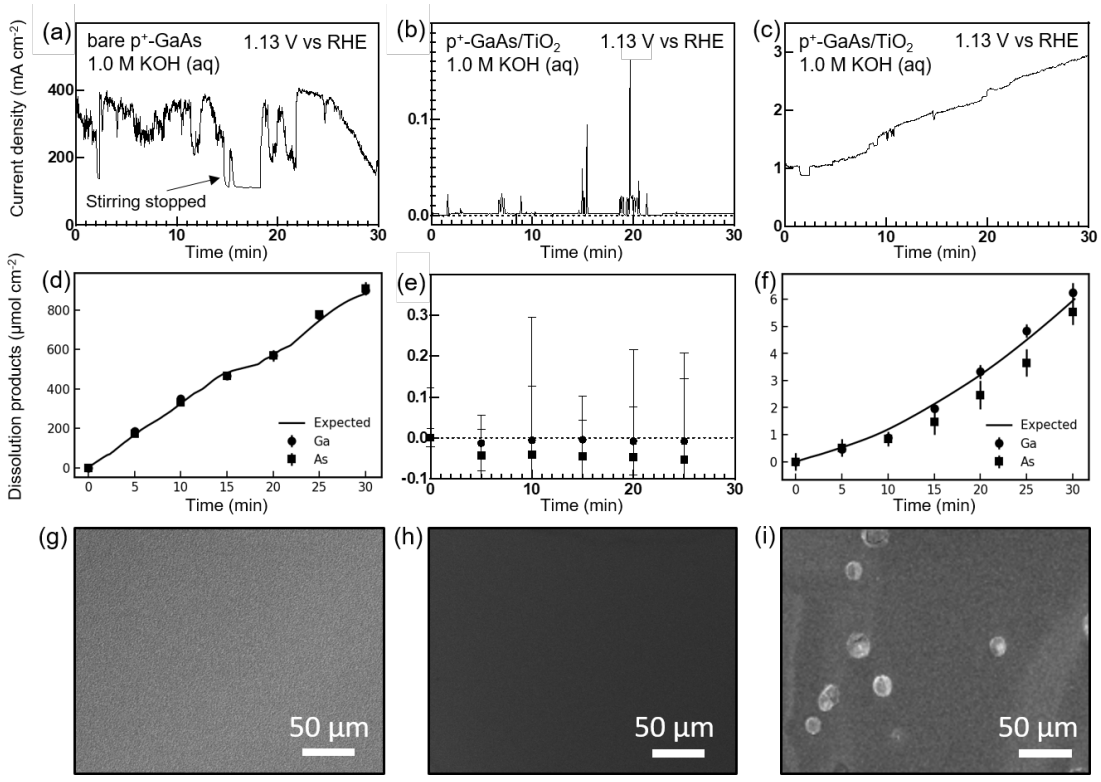

Figure 3.2. Current density as a function of time in contact with 1.0 M KOH(aq) while held potentiostatically at E = 1.13 V versus RHE for (a) bare GaAs, and (b,c) GaAs/TiO_2-1000x electrodes. In (b,c) samples, two different electrochemical behaviors were observed: (b) no apparent corrosion current and (c) corrosion current increase over time. (d–f) Concentrations of Ga and As species dissolved in the electrolytes over time as measured using ICP-MS during the experiments shown in (a–c) with the solid lines represent the expected dissolved GaAs calculated from the charge passed by the 6-electron GaAs dissolution. (g–i) SEMs of the electrodes after the 30 min chronoamperometry experiments shown in (a–c).

The collective results of Figure 3.1 and Figure 3.2 demonstrate that when operated in contact with 1.0 M KOH(aq) at a potential less positive than $E°(O_2/H_2O)$, some GaAs/a-TiO_2 samples undergo immediate pitting of the GaAs substrate (type ii), whereas other GaAs/a-TiO_2 samples exhibit no immediate evidence of corrosion (type i).

We hypothesized that the sites of pitting corrosion corresponded to pinhole defects that were randomly and sparsely distributed in the as-prepared ALD a-TiO_2 films. This would accordingly result in some pinhole-free GaAs/a-TiO_2 electrodes that exhibited stable electrochemical behavior and some GaAs/a-TiO_2 electrodes that contained pinholes and exhibited pitting corrosion. To confirm the existence of pinholes in the ALD a-TiO_2 films, galvanic displacement of GaAs by Au was used to tag the pinholes and amplify the contrast in the subsequent scanning-electron micrographs.

Electroless deposition of Au

Figure 3.3a–b shows SEMs of a bare p^+-GaAs substrate before and after, respectively, galvanic displacement in an acidic solution containing 1 mM $HAuCl_4$(aq). After galvanic displacement, the surface of the sample was covered uniformly by Au (Fig. 3.3b). The Au film was then peeled off of the sample, and the appearance of the underlying GaAs substrate was consistent with uniform corrosion (Fig. 3.3c) due to the oxidative corrosion process of galvanic displacement. Figure 3.3d shows an SEM of a p^+-GaAs/a-TiO_2-1000x sample that had been scribed and then subjected to galvanic displacement by Au. The Au selectively deposited at the exposed GaAs crevice. Moreover, no Au deposited galvanically onto an a-TiO_2 sample obtained by oxidizing a Ti foil (Fig S3.2), confirming the selectivity of the galvanic displacement for exposed GaAs sites on the GaAs/a-TiO_2 samples.

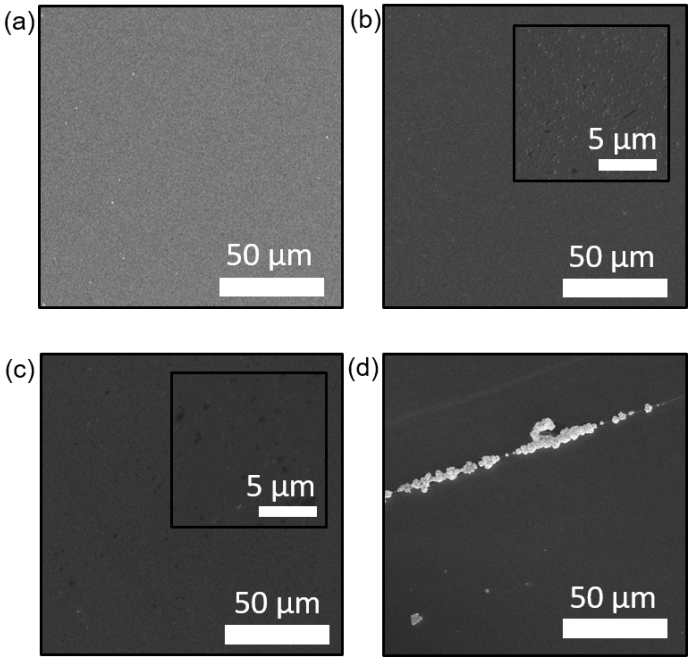

Figure 3.3. Scanning-electron micrographs of (a) GaAs before deposition, (b) GaAs after Au deposition (c) GaAs after Au deposition with the Au film removed, and (d) a-TiO_2/GaAs with a line scratch after Au deposition.

Figure 3.4a shows a cross-sectional SEM of a Au deposit formed on a p^+-GaAs/a-TiO_2-1000x sample after 30 min of galvanic displacement. The Au deposit had a fibrous, dendritic structure. Figure 3.4b-d shows that as the duration of the galvanic displacement increased, the amount of Au deposited increased. Figure 3.5 also shows quantification of the density and diameters of the Au deposits. The number of Au spots per unit electrode surface area increased as the duration of the galvanic displacement reaction increased from 0 to ~20 min (Fig 3.5a). No new pinholes were decorated during the galvanic displacement process after ~20 min and thereafter the spots increased in diameter until ultimately merging after 45 min (Fig. 3.5b). The exponential-like relationship between the diameter of Au deposits and the deposition time is consistent with a gradual increase in the average diameter in the beginning (< 20 min) as more pinhole sites are being decorated. Once all pinholes have been decorated, a more rapid increase in the average diameter was

observed, as expected when more surface area from the Au deposits is available for further deposition. The growth of the Au deposits with time is consistent with the fibrous nature of the Au deposits that allowed the Au solution to continue to contact and corrode the GaAs substrate. Scanning-electron micrograph images (Fig. 3.4b-d) showed that after 10 min of galvanic displacement, the Au completely covered the portion of the GaAs exposed through the orifice in the a-TiO_2 film. This behavior implies that the diameters of the pinholes are proportional to the size of the Au spots.

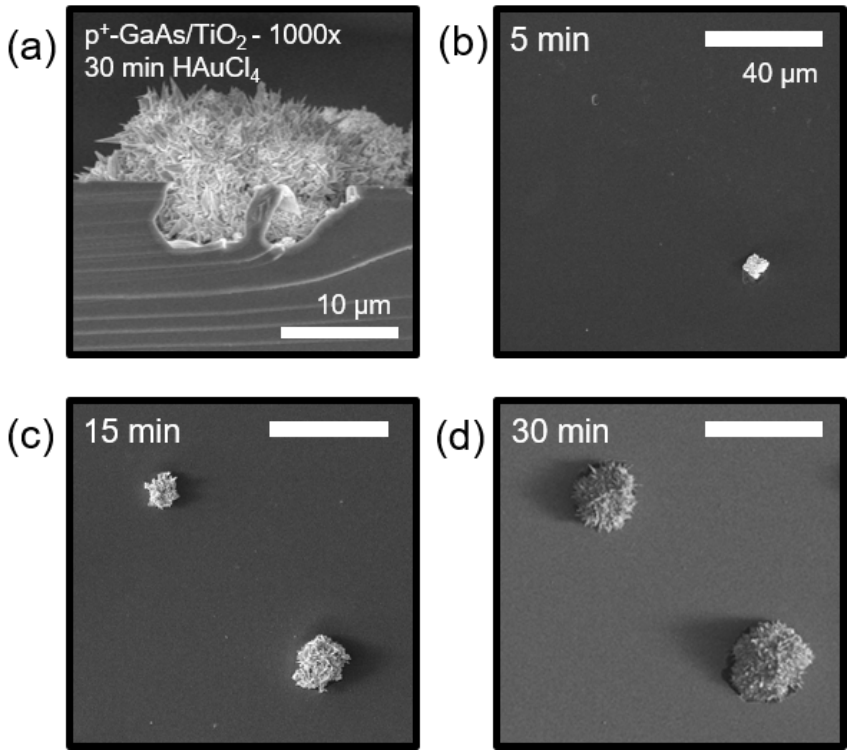

Figure 3.4. Scanning-electron micrographs of (a) a cross section of a GaAs/a-TiO_2-1000x substrate after 30 min of galvanic displacement by Au. Plan-view images of Au deposits on the surfaces of GaAs/a-TiO_2-1000x samples after galvanic displacements for (b) 5, (c) 15, and (d) 30 min

Pinholes formed during a-TiO_2 deposition

To compare the size distribution of the pinholes, galvanic displacement of Au was applied to GaAs/a-TiO_2-1000x samples immediately after a-TiO_2 deposition. Figure 3.5c shows the size distribution for 224 Au spots measured on GaAs/a-TiO_2-1000x samples after 10 min of galvanic displacement. The diameters of Au spots were sorted into 30 bins (~400 nm bin size), and the number of spots in each bin was counted. The ~400–800 nm bin contained the largest number of spots, exceeding by nearly 50% the number of spots in the next largest bin (~800–1200 nm). The distribution had a peak at ~800 nm and a tail toward larger diameters. The average diameter of the Au spots was 1.8 ± 1.6 μm for the 224 Au spots measured. The number and distribution of pinholes in a-TiO_2 layers of varied thickness were then analyzed using a Au deposition time of 30 min. Figure 3.5d shows the density of Au spots on GaAs/a-TiO_2 after 30-min galvanic displacement as a function of a-TiO_2 cycles. The density of the pinholes decreased with the thickness of the a-TiO_2 film (Fig. 3.5d).

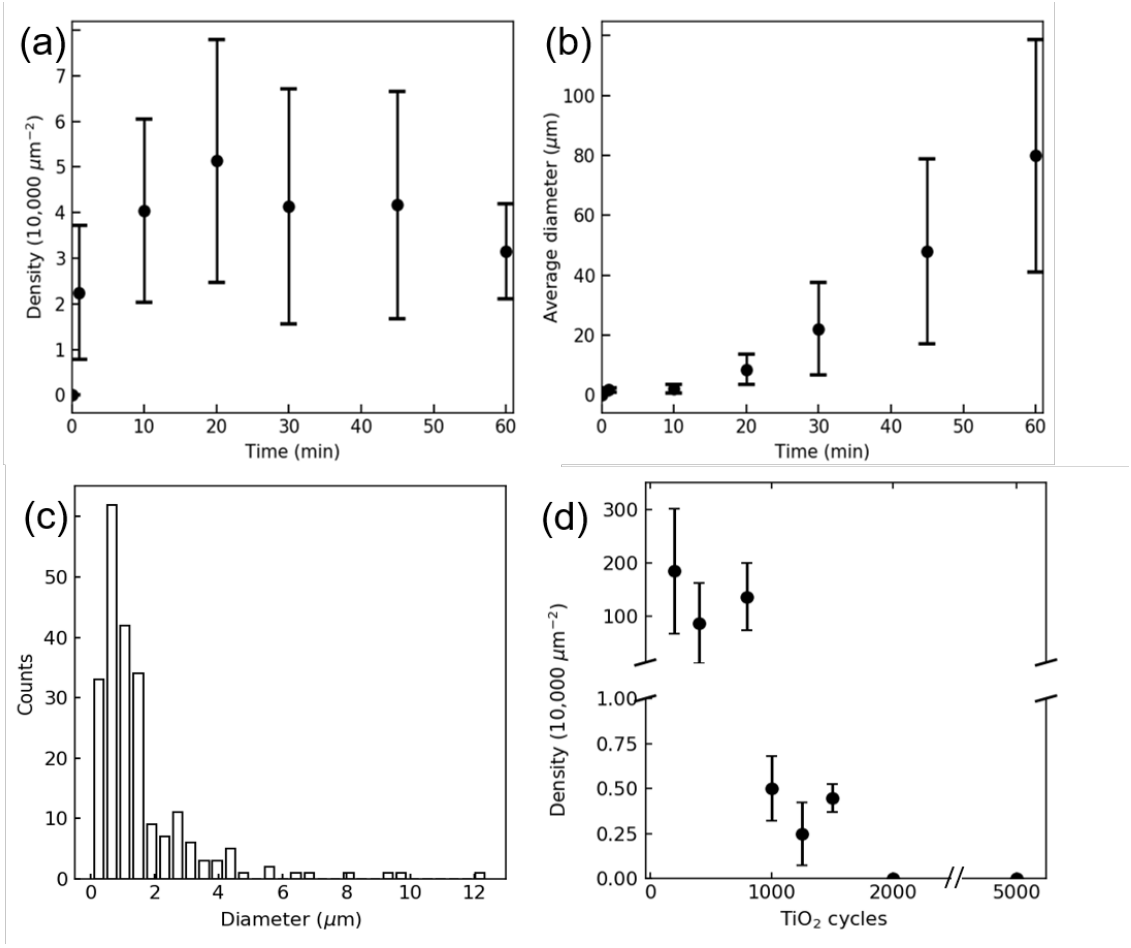

Figure 3.5. Properties of gold deposition. (a)-(b) Analysis of Au spots observed on GaAs/1000x- a-TiO_2 as a function of the duration of galvanic displacement, showing (a) the average number of spots per unit electrode area, and (b) the average diameter of the Au spots on the surface in a 100 µm x 100 µm square. The error bars represent one standard deviation of the measurements from different areas of the electrode surface. (c) Distribution of the diameters of the plated Au spots after 10 min of deposition on 1000x-a-TiO_2/GaAs. (d) The density of Au spots on GaAs/a-TiO_2 samples after 30-min galvanic displacement as a function of the number of a-TiO_2 cycles.

Pinholes were observed to form in ALD films both randomly and in clusters, leading to high variability in the pinhole density.[15] Although the mean value of the distribution of Au spots is considerably larger than the size distribution of the actual pinholes, the shape of the distribution, having a long tail toward larger diameters, is

consistent with the hypothesis that the pinholes predominantly originate from external atmospheric particulates present during a-TiO_2 film deposition.[15,19] Moreover, the defect density decreased substantially after 800 cycles of a-TiO_2 (~45 nm), which could be a result of the a-TiO_2 film covering the majority of defects resulting from atmospheric particulate matter. The defect density continued to decrease with increases in thickness of the a-TiO_2 film, and approached zero after 2000 ALD cycles (~112 nm), indicating that a pinhole-free coating over the electrode area may be achieved at this thickness.

Figure 3.6 compares the density of Au spots formed by galvanic displacement on GaAs samples covered with thin a-TiO_2 films (400 ALD cycles) to the Au spot density for a second set of samples grown using nominally the same deposition conditions but in a class-100 environmentally controlled cleanroom. The density of Au spots was much lower for the samples grown in the cleanroom (0.21±0.14 counts per 10^4 μm^{-2}) than for samples grown outside the cleanroom (86.8±74.9 counts per 10^4 μm^{-2}). This result clearly supports the hypothesis that the dominant source of pinholes in the a-ALD TiO_2 films is atmospheric particulates that are present during the deposition of the a-TiO_2.

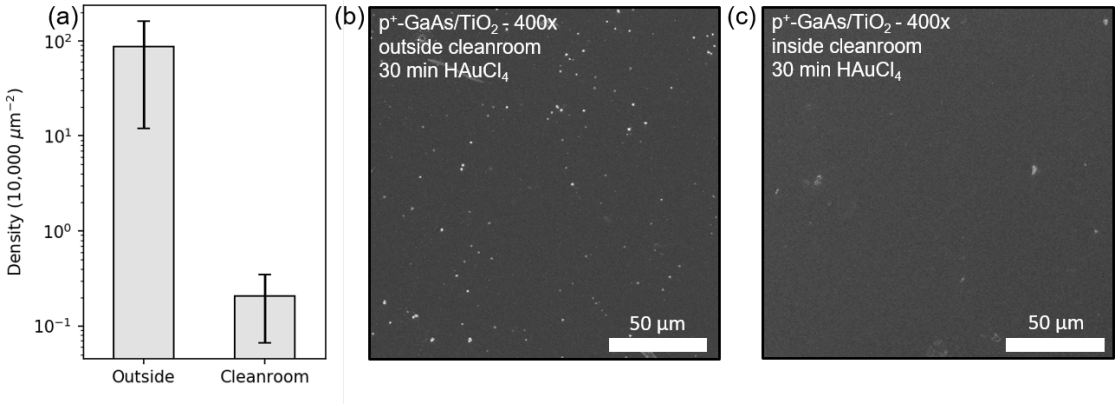

Figure 3.6. (a) Comparison of the density of pinholes in a-TiO_2 films that were grown either inside or outside an environmentally controlled cleanroom. Samples were p^+-GaAs/a-TiO_2-400x, and Au spots were counted after 30 min of galvanic displacement. Representative SEMs of samples prepared (b) outside the cleanroom, and (c) inside the cleanroom.

Pinholes formed during electrochemical operation

For substrates that actively corrode under oxidizing conditions, such as III-V semiconductors, pinholes formed in protective coatings during the ALD process will have an immediate deleterious effect on the electrochemical stability of the protected semiconductor electrodes. However, additional pinholes might also form during electrochemical operation. Figure 3.7a shows J measured as a function of time for a p^+-GaAs/a-TiO_2-2000x sample held at E = 1.13 V versus RHE while in contact with 1.0 M KOH(aq). After 8.2 h, J increased from ~ 0 mA cm^{-2} to 0.19 mA cm^{-2}, and after another hour, J increased to 0.26 mA cm^{-2}. After ~15 h of potential control, J increased steadily to > 1.5 mA cm^{-2}. The initial lack of substantial corrosion current density implies that not all corrosion defects were initially present before the electrolysis, whereas the stepwise increase in the GaAs corrosion current density at 8.2 h suggests that either new defects can form over time or inactive defects can become activated during electrolysis. Exposure of the GaAs substrate after an electrochemical experiment is also consistent with the increase in the corrosion current observed in a J-E scan for a p^+-GaAs/a-TiO_2/Ni sample after 6 h of potential control (Fig. 3.7b). Similar behavior was also observed in a sample without Ni (Fig. S3.3). Due to the irreversible nature of electroless Au deposition, imaging these pinholes formed during electrochemical testing would require an operando SEM and is beyond the scope of this work.

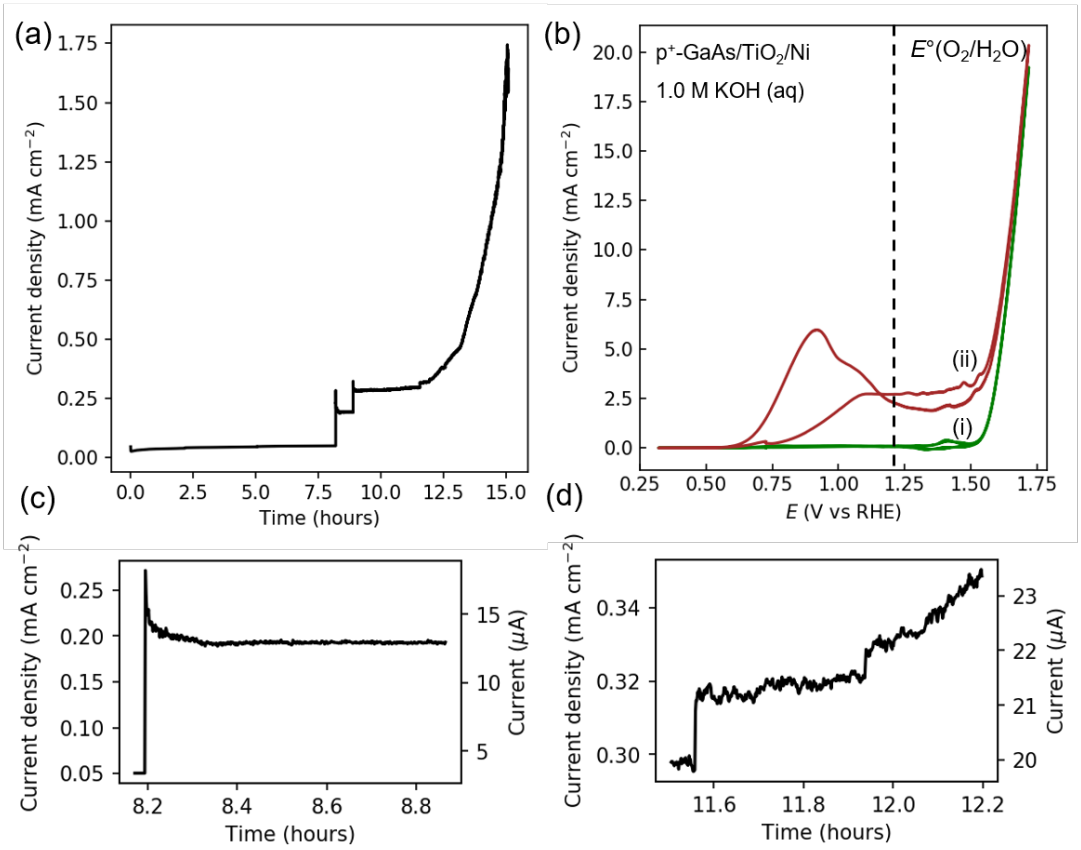

Figure 3.7. (a) Current density as a function of time of GaAs/a-TiO_2-2000x held at 1.13 V vs. RHE in 1.0 M KOH(aq) (b) *J-E* behavior of p^+- GaAs samples coated with a-TiO_2 (2000 ALD cycles) and sputtered Ni (GaAs/ a-TiO_2-2000x/Ni) at (i) 0 h and (ii) 6 h. The scan rate was 40 mV s^{-1}. (c,d) Current density as a function of time of GaAs/2000x-a-TiO_2 held at 1.13 V vs. RHE in 1.0 M KOH(aq) showing time window of Fig. 3.6a between (c) 8.17-8.87 hours and (d) 11.50-12.20 hours.

When a step increase in current density occurred, two different electrochemical behaviors were observed: (A) a large stepwise increase followed by a transient decay until the current density reached a new steady-state, and (B) a small stepwise increase followed by a continuous and gradual increase in current density. Figure 3.7c shows a time window of Figure 3.7a between 8.17 h and 8.87 h representing "A" behavior in which *J* increased from 0.05 mA cm^{-2} to 0.26 mA cm^{-2} followed by a decay to steady-state with J = 0.19 mA cm^{-2}. Figure 3.7d shows a time window between 11.50 h and 12.20 h of 3.7a,

representing "B" behavior, in which J increased from 0.298 mA cm^{-2} to 0.318 mA cm^{-2} followed by a small increase in J, and another stepwise increase from 0.321 mA cm^{-2} to 0.330 mA cm^{-2} followed by a continuous linear increase in J.

In "A" behavior, the transient decay indicates a decrease in corrosion rate after the initial spike, which likely indicates limited OH^- mass transport through pinholes (from the pinholes to the underlying etch pit). This mass-transport controlled of OH^- was evaluated using an axis-symmetric two-dimensional multiphysics model. The initial configuration of the sample contained a flat GaAs substrate, an insulating a-TiO_2 film with a fixed diameter orifice, and bulk electrolyte on top of the film (Figure S3.4). The transport of OH^- was governed by Nernst-Plank equation and the continuity equation

$$\frac{\partial c_i}{\partial t} + \nabla \cdot J_i(x) = R_i$$

$$\frac{\partial c_i}{\partial t} + \nabla \cdot (-D_i \nabla c_i - z_i u_{m,i} F c_i \nabla V) = R_i \qquad \text{(Eq. 3.3)}$$

where $J_i(x)$, D_i, c_i, z_i, and $u_{m,i}$ are the flux, the diffusion coefficient, concentration, charge number, and mobility, respectively, of species i within the electrolyte, and F, V, and R_i are the Faraday constant, the static electric field, and the chemical reaction rate of the corresponding species. In the simulation, the a-TiO_2 layer was modeled as an insulating layer. The anodic electrochemical reaction (Eq. 3.1) occurs at the interface between the electrolyte and GaAs. The kinetics of the reaction can be described with the concentration-associated anodic Tafel equation,

$$i = \frac{c_{OH^-}}{c^*_{OH^-}} i_0 \times 10^{\eta / A_a} \qquad \text{(Eq. 4)}$$

where c_{OH^-} and $c^*_{OH^-}$ represent the local and bulk OH^- concentrations, respectively, A_a represents the anodic Tafel slope, η represents the overpotential, and i_0 represents the

exchange-current density, which was set to 100 mA cm^{-2} to ensure facile corrosion kinetics and force mass-transport controlled behavior in the simulation.

Figure 3.8a shows the simulated current as a function of time for pinholes with four different radii but the same a-TiO_2 thickness (112 nm). For all pinhole sizes, the simulated current shows an initial transient spike that decays and reaches a steady state after a few seconds. Different pinhole radii lead to different maximum currents in the intial spike and steady-state electrolyte currents. The steady-state current increases with pinhole size, due to the decrease in OH^- diffusion resistance, whereas differences in the current of the intial spike are due to the amount of electrolyte that is contained in the pinhole. At the start of the simulation, the OH^- concentration at the GaAs surface is 1.0 M but rapidly decays and, with the depletion of the OH^- concentration within the pinhole, the current reaches a steady-state level controlled by the mass transport of OH^- through the pinhole. The time to reach a steady state in the simulation reflects the large assumed exchange-current density i_0 in Eq. 3.4 that was used to maximize the corrosion kinetics and leads to rapid consumption of OH^- at the interface. The large i_0 is not meant to represent the observed rate. The magnitude of the initial and steady-state currents are close to those observed experimentally and the characteristic electrochemical behavior of the simulation is representative of the experimental observations. Figure 3.8b-c shows the simulated concentration map of the concentration of OH^- , c_{OH^-}, in the electrolyte after 2.4 s of corrosion assuming a 3-μm radius pinhole. The value of c_{OH^-} at the surface of the corroding GaAs varies from 37 mM (near the intersection of the GaAs and a-TiO_2 surface) to 50 mM (at the lowest point of the GaAs surface), and remains at 1.0 M in the bulk electrolyte away from the pinhole. A much smaller difference in the ratio of c_{OH^-} between the bulk electrolyte and the top of the pinhole also shows that, at 1.0 M, the transport of OH^- from the bulk electrolyte to the pinhole is not the main limiting factor. The steady-state current that appears within 2 s indicates that even with the facile GaAs corrosion kinetics (large i_0), the rate of corrosion is quickly dominated by the OH^- concentration gradient, and thus the mass transport, of OH^- through the orifice in the a-TiO_2 film. This behavior is consistent with the “A” behavior

observed in Fig 3.6a, where the opening of a new fixed-diameter pinhole leads to corrosion of the substrate.

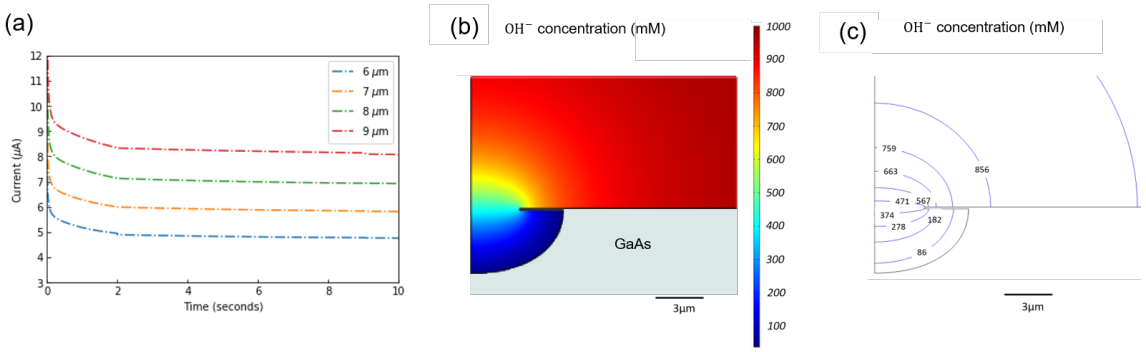

Figure 8. (a) The simulated corrosion current as a function of time for different pinhole sizes with the thickness of a-TiO_2 fixed at 112 nm in the simulation. (b) Color map and (c) contour plot of the OH^- concentration in the electrolyte after 2.4 s of corrosion.

In contrast, "B" behavior suggests a smaller initial pinhole, because of the smaller stepwise increase in *J*, but with a gradual increase in pinhole size as a function of time. The increase in the pinhole area likely comes from either expanding the diameter of the pinhole or its merging with nearby pinholes. After the formation of multiple pinholes, the merging of existing pinholes to form a larger channel can lead to an exponential increase in corrosion current as observed after 12.5 h of operation (Fig. 3.7a,d). These "A" and "B" corrosions can also be observed on a representative micrograph showing both ("A") spherical underlying etch pits with a fixed-diameter pinhole and ("B") merging pinholes (Fig. S3.5). The current density continues to increase as more areas of GaAs are being etched until the electrolyte eventually reaches the back contact after 20 h, producing a very large stepwise increase in *J* (from ~ 2.5 mA cm^{-2} to ~ 15 mA cm^{-2} in Fig. 3.9a).

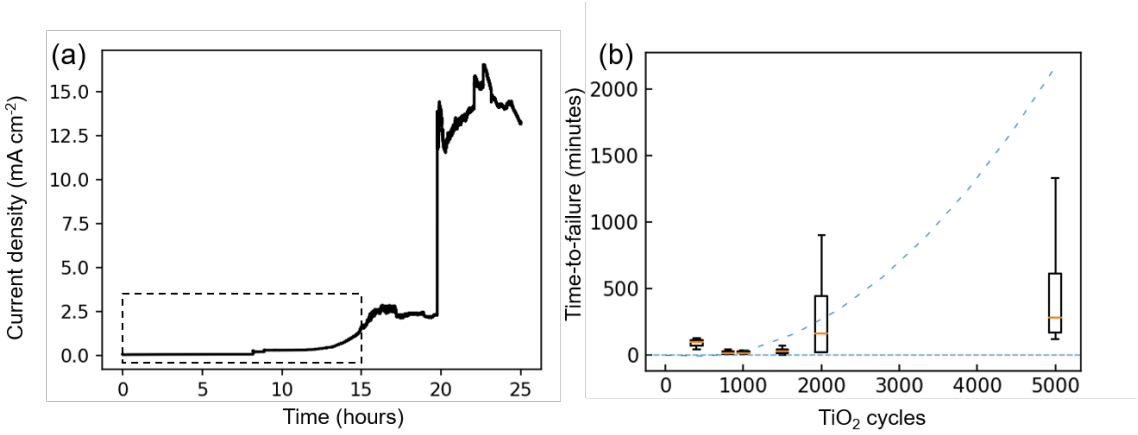

Figure 3.9. (a) Current density as a function of time of GaAs/2000x- a-TiO_2 held at 1.13 V vs. RHE in 1.0 M KOH(aq) with the time extended to 25 h. The dashed box shows the region plotted in Fig. 3.7. (b) Elapsed time until the first step-wise increase in the current density as a function of a-TiO_2 cycles. The orange lines represent the medians; the box extends from the lower to the upper quartiles; the whiskers represent the range of the data. The blue long dashed line represents a fit of the data to a [thickness]^2 dependence using the data up to 2000 ALD TiO_2 cycles.

If all pinholes are separated, the first pinhole formed after 8.2 h would continue to etch isotopically with a fixed diameter, and ~55 h would be required to etch through the substrate and reach back contact. However, the shorter time elapsed between the first pinhole formation and the electrolyte reaching back contact (~20 h) is expected because merging of multiple pinholes leads to a larger exposed substrate area, representing a classic characteristic of corrosion by pitting.

Although extrinsic pinhole defects clearly constitute the predominant short-term failure mode of ALD a-TiO_2 protection layers, pinhole-free thick ALD a-TiO_2 films may still be subject to long-term failure processes. Figure 3.9b shows an analysis of the time-to-failure as a function of the number of ALD cycles, where time-to-failure was defined as the time elapsed before the first increase in J for p^+-GaAs/a-TiO_2 samples held at E = 1.13 V versus RHE while in contact with 1.0 M KOH(aq). All a-TiO_2 films formed using < 400 ALD cycles (> 22 nm) on p^+-GaAs showed electrochemical evidence of initial pinholes.

The time-to-failure increased substantially after 1500 cycles, showing that the time-to-failure depended on film thickness.

The dependence of time-to-failure on thickness is consistent with a mechanism involving transport of reactive species through the film, by either diffusion or migration, as has been proposed for a-TiO_2/Si.[8,9] To investigate the transport of reactive species, the oxygen profile in the a-TiO_2 was studied using XPS depth-profile analysis on pinhole-free p^+-GaAs/a-TiO_2-400x samples. The analysis was done on the region that did not show evidence of corrosion. Figure S3.6 shows the area under the peaks for the Ti 2p, O 1s, Ga 3d, and As 3d signals, respectively, as a function of sputtering time on the samples before testing as well as after 1 h or 12 h of testing. In all three samples, Ga 3d and As 3d signals remained zero until ~600 min of sputtering time at which point the p^+-GaAs/a-TiO_2 interface was exposed. A slightly higher intensity for the Ga 3d and As 3d signals and lower intensity for the O 1s and Ti 2p signals in the first sputtering step are likely due to surface contamination and residues from the electrochemical experiment. Both the Ti 2p and O 1s signals slowly decreased from the beginning to ~200 min of sputtering time and continued to decrease again at ~600 min of sputtering time at the p^+-GaAs/a-TiO_2 interface.

No substantial compositional change was observed in the film after both 1 h and 12 h of testing. Ar-ion bombardment during the sputtering process has been shown to alter the Ti 2p spectrum leading to reduction of Ti^{4+} (to Ti^{2+}, Ti^{3+}), thus not accurately representing the underlying composition of TiO_2.[20] This behavior is representative of the initial decrease during the first ~200 min of sputtering time in all samples. To accurately quantify the transport of oxygen species through the film and to distinguish the oxygen arising from the electrolyte from oxygen in the a-TiO_2 film would require secondary ion mass spectrometry (SIMS) coupled with labeled oxygen isotopic analysis.

In addition, although the time-to-failure was observed to depend on the film thickness, the time-to-failure for p^+-GaAs/a-TiO_2-5000x (150–1200 min) films was shorter than expected (~2000 min) if diffusion through the a-TiO_2 were the only cause of the failure (Fig. 9b). Hence other mechanisms, such as local dissolution of the a-TiO_2 film or a

degradation of the mechanical integrity of the a-TiO_2 film likely contribute to the long-term failure of a-TiO_2 films as well. Further investigations of the mechanisms of degradation of a-TiO_2 films during long-term electrochemical operation are therefore required to fully understand and mitigate long-term failure of ALD a-TiO_2 protective coatings for oxygen-evolving photoanodes that undergo corrosion by dissolution. If the long-term failure mode is dominated by localized defective regions instead of an intrinsic property of an a-TiO_2 film, then isolating the defects and/or passivating the defective region to prevent further corrosion would increase the overall stability of the III-V devices. Evidence in support of intrinsic long-term durability of the a-TiO_2 is provided from the use of a-TiO_2 protection layers in the n-Si/a-TiO_2 system. The a-TiO_2 coating increased the stability of Si microwire photoanodes to >2200 h of continuous operation, attesting to the intrinsic long-term durability of protective a-TiO_2 films on photoanodes that are effecting the oxygen-evolution reaction.[3,21]

Conclusions

Pinhole defects in a-TiO_2 coatings formed during ALD lead to immediate failure and pitting corrosion of the underlying GaAs substrate when operated electrochemically in contact with 1.0 M KOH (aq). Galvanic displacement by Au facilitated imaging the sites of pinholes using scanning-electron microscopy, and enabled an analysis of the number of pinholes per unit electrode area, and of the dependence of the pinhole density on film thickness. The measurements and analyses suggest that the dominant source of pinholes in a-TiO_2 coatings is external atmospheric particulate matter present during the preparation and deposition steps. a-TiO_2 films with substantially lower pinhole densities were obtained when the thickness of the a-TiO_2 coating exceeded 45 nm, and nearly pinhole-free a-TiO_2 films could be fabricated when the a-TiO_2 thickness exceeded 112 nm. A similar result can also be achieved by careful preparation and a-TiO_2 film deposition in an environmentally controlled cleanroom. Long-term failure modes also exist in ALD a-TiO_2 films. Electrochemical measurements showed that pinholes can form or be exposed over time on electrodes that were initially pinhole-free. The time-to-failure increased as the thickness of the a-TiO_2 film increased, implying that transport of reactive species across the film could contribute to the failure of thick a-TiO_2 protective coatings that were initially nearly pinhole-free. Further understanding of the long-term failure mechanism, as well as differences between photoanodes that corrode vs. photoanodes that passivate, is required to rationally develop mitigation strategies that allow for extended long-term operation of protected photoanodes for evolution of O_2(g) from water.

Experimental Methods

Materials and chemicals

Water with a resistivity ρ > 18 MΩ·cm obtained from a Barnstead Millipore purification system was used throughout. All chemicals, including hydrochloric acid (ACS Grade, VWR), potassium hydroxide (TraceSELECT, ≥30% in water, Honeywell Fluka), and gold(III) chloride hydrate $HAuCl_4$ (~50%, Chem-Impex International Inc.) were used as received unless otherwise noted. Crystalline single-side polished GaAs substrates, p^+-GaAs (100) (350±25 μm), were degenerately doped with zinc to a majority-carrier density of 0.5-5 × 10^{19} cm^{-3} (AXT Inc.).

Preparation of substrates

The GaAs wafers were cleaned with 10% HCl(aq) for 30 min to remove native oxide on the surface.[22] The samples were then rinsed with copious amounts of deionized H_2O and dried using a stream of N_2(g).

Atomic-layer deposition (ALD) of TiO_2 thin films

a-TiO_2 films were grown using tetrakis(dimethylamido)-titanium (TDMAT). For TiO_2 films prepared from the TDMAT precursor, a Cambridge Nanotech S200 or Oxford Instruments FlexAL ALD system was used for deposition outside and inside the cleanroom. Each ALD cycle consisted of a 0.10 s exposure to TDMAT (Sigma-Aldrich, 99.999%), a N_2(g) (Airgas, 99.999%) purge, a 0.015 s exposure to H_2O, and a final N_2(g) purge. Research grade 20 sccm N_2(g) was used for the N_2(g) purges, and each N_2(g) purge was 15 s in duration. During the deposition, the substrate and the TDMAT precursor were heated to 150 °C and 75 °C, respectively, while the H_2O remained at room temperature. Most samples were prepared with 400 cycles and 1000 ALD cycles, producing a nominal thickness of 22 nm and 55 nm, respectively. The film thickness and refractive index were measured via spectroscopic ellipsometry (J.A. Woollam Co., alpha-SE) and were fit to a Cauchy model.

Radio-frequency sputtering deposition

A radio-frequency sputtering system (AJA International Inc.) was used to deposit Ni and Cu for preparation of oxygen-evolution reduction (OER) catalysts as well as to produce back ohmic contacts to p^+-GaAs. The base pressure was kept at $<1x10^{-7}$ Torr, and the deposition pressure was kept at 5 mTorr. An radio-frequency (rf) power of 100 W was used during the deposition.

Electrode fabrication

Electrodes were fabricated by using a scribe to cleave the samples into ~ 0.1 cm^2 pieces. Ohmic contact was made by sequentially depositing Ni/Cu films onto the unpolished back sides of the p^+-GaAs samples.[1] The back contact to the sample was affixed to a Cu wire with Ag paste. The Cu wire was threaded through a glass tube (Corning Incorporation, Pyrex tubing, 7740 glass), and all but the front of the sample was encapsulated with Loctite epoxy (Hysol 9462). After curing, the electrode was scanned with an Epson scanner (V19) and analyzed with ImageJ software, to determine the area of the exposed region.

Scanning-electron microscopy

Scanning-electron micrographs (SEMs) were obtained with an FEI Nova NanoSEM 450 at an accelerating voltage of 5.00 kV with a working distance of 5 mm and an in-lens secondary electron detector.

Inductively coupled plasma mass spectroscopy

Inductively coupled plasma mass spectrometry (ICP-MS) data were collected using an Agilent 8800 Triple Quadrupole ICP-MS system. ICP-MS samples were collected periodically throughout electrochemical corrosion experiments. Samples were diluted 50x with 2% nitric acid before analysis. ICP-MS concentration standards were made with serial dilutions of a known concentration standard (Sigma-Aldrich) with 2% nitric acid. Each concentration standard had KOH added in a 50:1 volumetric ratio of nitric acid: KOH (2%,

1.0 M, respectively) to match the solution matrix of the ICP-MS samples. Quantification was verified by independently making four additional samples of known concentration, two for As and two for Ga, and analyzing them at the beginning, middle, and end of all ICP-MS analysis. ICP-MS results were only used when the samples of known concentration were measured to be consistent throughout the ICP-MS run. The samples of known concentration were also made on a mass basis and were matrix-matched with the same 50 nitric acid:1 KOH volumetric ratio as both the unknown samples and the concentration standards. The total amount of dissolved Ga and As from the electrodes was then calculated and normalized to the geometric electrode area.

X-ray photoelectron spectroscopy

X-ray photoelectron spectroscopy (XPS) was performed using a Kratos Axis Ultra system with a base pressure of 1 x 10^{-9} torr in the analysis chamber. A monochromatic Al Kα source was used to irradiate the sample with X-rays (1486.7eV) at 150 W. For depth profiling, Ar+ ions with an energy of 2 keV were used. A hemispherical analyzer oriented for detection along the sample surface normal was used for maximum depth sensitivity. Depth profile spectra were acquired with a pass energy of 160 eV and acquisition time of 20 seconds each. The data were analyzed using CasaXPS computer software.

XPS data were obtained ex-situ, i.e., after a short sample transfer through air, which could potentially confound linking the surface composition and oxidation states found in UHV to the ones present during electrochemistry.

Electroless gold deposition

Electrodes were immersed in 10 mL of 1.0 M HCl(aq) for 1 min, then 10 mL of a 2 mM $HAuCl_4$ stock solution was added to the solution to produce a nominal concentration of 1 mM $HAuCl_4$.[18] Unless noted otherwise, all depositions were performed for 30 min at open circuit.

Image processing and pinhole density calculation

Scanning-electron micrographs of the surface after galvanic displacement of Au were analyzed using ImageJ software, with each processing step shown in Fig. S3.7. First, the raw image was converted into an 8-bit image. The image was then further converted into a black/white image with a specific threshold. The threshold was adjusted in each image depending on its contrast and brightness to include all gold deposits. The built-in particle analysis function was used to obtain the counts and the size distribution of the particles.

Electrochemical characterization

Electrochemical data were obtained using a BioLogic SP-200 potentiostat in a three-electrode configuration with 1.0 M KOH(aq) as the electrolyte, and a Hg/HgO electrode (CH Instruments, Inc., CHI-152) was used as the reference electrode for the alkaline solution. A carbon rod (Strem Chemicals, 99.999%) inside a porous fritted gas dispersion tube (Sigma Aldrich, Z408727) was used as the counter electrode. *J-E* data were collected between -0.6 V and 0.8 V vs. Hg/HgO at a 20-mV s^{-1} scan rate. Chronoamperometry (CA) data were collected every 1 s while holding the electrode potential at 0.212 V vs. Hg/HgO, unless noted otherwise. For a study of pinhole-free TiO_2 films, the chronoamperometry at 0.212 V vs. Hg/HgO from the first 1 min was closely monitored and had to exhibit a stable current density below 1 mA cm^{-2}.

Simulation of an etched pit

The electrolyte was modeled as a stagnant liquid, in which transport of electrolyte species was controlled by the diffusion and migration terms in the Nernst-Plank equation and the continuity equation (Eq. 3.3) and the corrosion kinetics by the Tafel equation (Eq. 3.4). The anodic Tafel slope, A_a, and the overpotential, η, were taken to be 120 mV dec^{-1} and 300 mV respectively. At each time step, the consumption of OH^- at the surface was calculated by Faraday's law using the current density from the previous time

step (Eq. 3.4). The addition of OH^- was then calculated using Eq. 3.3. Then, the current density at the surface was re-calculated from the new OH^- concentration, c_{OH^-}.

As time passes, the chemical etching on GaAs takes place with a velocity in the normal direction, *v*, according to

$$v = \frac{i}{6F}\frac{M}{\rho} \qquad \text{(Eq. 3.5)}$$

where M is the molar mass (145 g mol^{-1}) and ρ is the density (5320 kg m^{-3}) of gallium arsenide.

The OH^- concentration is fixed at 1 M on the top surface of the electrolyte domain, which accounts for the solution mixing. The cathode was set far apart from the anode and is not shown in Fig. S4.

The standard FEM solver in the COMSOL multi-physics package was used to obtain the modeled electrochemical behavior. The maximum element size and the maximum element growth rate for this 2-D axis-symmetric model were 72 nm and 1.1, respectively, for the region near the electrolyte electrode interface, and were 1.4 μm and 1.2, respectively, for the rest of the system. A relative tolerance of the corresponding variable of 0.001 was applied as the convergence criterion for all simulations.

References

(1) Hu, S.; Shaner, M. R.; Beardslee, J. A.; Lichterman, M.; Brunschwig, B. S.; Lewis, N. S. Amorphous TiO_2 Coatings Stabilize Si, GaAs, and GaP Photoanodes for Efficient Water Oxidation. *Science* **2014**, *344* (6187), 1005–1009. https://doi.org/10.1126/science.1251428.

(2) Zhou, X.; Liu, R.; Sun, K.; Chen, Y.; Verlage, E.; Francis, S. A.; Lewis, N. S.; Xiang, C. Solar-Driven Reduction of 1 Atm of CO_2 to Formate at 10% Energy-Conversion Efficiency by Use of a TiO_2-Protected III–V Tandem Photoanode in Conjunction with a Bipolar Membrane and a Pd/C Cathode. *ACS Energy Lett.* **2016**, *1* (4), 764–770. https://doi.org/10.1021/acsenergylett.6b00317.

(3) Shaner, M. R.; Hu, S.; Sun, K.; Lewis, N. S. Stabilization of Si Microwire Arrays for Solar-Driven H_2O Oxidation to O_2(g) in 1.0 M KOH(Aq) Using Conformal Coatings of Amorphous TiO_2. *Energy Environ. Sci.* **2015**, *8* (1), 203–207. https://doi.org/10.1039/C4EE03012E.

(4) Lichterman, M. F.; Carim, A. I.; McDowell, M. T.; Hu, S.; Gray, H. B.; Brunschwig, B. S.; Lewis, N. S. Stabilization of N-Cadmium Telluride Photoanodes for Water Oxidation to O_2(g) in Aqueous Alkaline Electrolytes Using Amorphous TiO_2 Films Formed by Atomic-Layer Deposition. *Energy Environ. Sci.* **2014**, *7* (10), 3334–3337. https://doi.org/10.1039/C4EE01914H.

(5) Verlage, E.; Hu, S.; Liu, R.; Jones, R. J. R.; Sun, K.; Xiang, C.; Lewis, N. S.; Atwater, H. A. A Monolithically Integrated, Intrinsically Safe, 10% Efficient, Solar-Driven Water-Splitting System Based on Active, Stable Earth-Abundant Electrocatalysts in Conjunction with Tandem III–V Light Absorbers Protected by Amorphous TiO_2 Films. *Energy Environ. Sci.* **2015**, *8* (11), 3166–3172. https://doi.org/10.1039/C5EE01786F.

(6) Bae, D.; Seger, B.; Vesborg, P. C. K.; Hansen, O.; Chorkendorff, I. Strategies for Stable Water Splitting via Protected Photoelectrodes. *Chem. Soc. Rev.* **2017**, *46* (7), 1933–1954. https://doi.org/10.1039/C6CS00918B.

(7) Bae, D.; Shayestehaminzadeh, S.; Thorsteinsson, E. B.; Pedersen, T.; Hansen, O.; Seger, B.; Vesborg, P. C. K.; Ólafsson, S.; Chorkendorff, I. Protection of Si Photocathode Using TiO_2 Deposited by High Power Impulse Magnetron Sputtering for H_2 Evolution in Alkaline Media. *Sol. Energy Mater. Sol. Cells* **2016**, *144*, 758–765. https://doi.org/10.1016/j.solmat.2015.10.020.

(8) Yu, Y.; Sun, C.; Yin, X.; Li, J.; Cao, S.; Zhang, C.; Voyles, P. M.; Wang, X. Metastable Intermediates in Amorphous Titanium Oxide: A Hidden Role Leading to Ultra-Stable Photoanode Protection. *Nano Lett.* **2018**, *18* (8), 5335–5342. https://doi.org/10.1021/acs.nanolett.8b02559.

(9) Ros, C.; Carretero, N. M.; David, J.; Arbiol, J.; Andreu, T.; Morante, J. R. Insight into the Degradation Mechanisms of Atomic Layer Deposited TiO_2 as Photoanode Protective Layer. *ACS Appl. Mater. Interfaces* **2019**, *11* (33), 29725–29735. https://doi.org/10.1021/acsami.9b05724.

(10) Dameron, A. A.; Davidson, S. D.; Burton, B. B.; Carcia, P. F.; Scott McLean, R.; George, S. M. Gas Diffusion Barriers on Polymers Using Multilayers Fabricated by Al_2O_3 and Rapid SiO_2 Atomic Layer Deposition. *J. Phys. Chem. C* **2008**, *112* (12), 4573–4580. https://doi.org/10.1021/jp076866+.

(11) Abdulagatov, A. I.; Yan, Y.; Cooper, J. R.; Zhang, Y.; Gibbs, Z. M.; Cavanagh, A. S.; Yang, R. G.; Lee, Y. C.; George, S. M. Al_2O_3 and TiO_2 Atomic Layer Deposition on Copper for Water Corrosion Resistance. *ACS Appl. Mater. Interfaces* **2011**, *3* (12), 4593–4601. https://doi.org/10.1021/am2009579.

(12) Spahr, H.; Bülow, T.; Nowak, C.; Hirschberg, F.; Reinker, J.; Hamwi, S.; Johannes, H. H.; Kowalsky, W. Impact of Morphological Defects on the Electrical Breakdown of Ultra Thin Atomic Layer Deposition Processed Al_2O_3 Layers. *Thin Solid Films* **2013**, *534*, 172–176. https://doi.org/10.1016/j.tsf.2013.02.076.

(13) Lahtinen, K.; Lahti, J.; Johansson, P.; Seppänen, T.; Cameron, D. C. Influence of Substrate Contamination, Web Handling, and Pretreatments on the Barrier Performance of Aluminum Oxide Atomic Layer-Deposited BOPP Film. *J. Coatings*

Technol. Res. **2014**, *11* (5), 775–784. https://doi.org/10.1007/s11998-014-9584-9.

(14) Zhang, Y.; Seghete, D.; Abdulagatov, A.; Gibbs, Z.; Cavanagh, A.; Yang, R.; George, S.; Lee, Y.-C. Investigation of the Defect Density in Ultra-Thin Al_2O_3 Films Grown Using Atomic Layer Deposition. *Surf. Coatings Technol.* **2011**, *205* (10), 3334–3339. https://doi.org/10.1016/j.surfcoat.2010.12.001.

(15) Yersak, A. S.; Lee, Y.-C. Probabilistic Distributions of Pinhole Defects in Atomic Layer Deposited Films on Polymeric Substrates. *J. Vac. Sci. Technol. A Vacuum, Surfaces, Film.* **2016**, *34* (1), 01A149. https://doi.org/10.1116/1.4938496.

(16) Zhang, Y.; Bertrand, J. A.; Yang, R.; George, S. M.; Lee, Y. C. Electroplating to Visualize Defects in Al_2O_3 Thin Films Grown Using Atomic Layer Deposition. *Thin Solid Films* **2009**, *517* (11), 3269–3272. https://doi.org/10.1016/j.tsf.2008.12.052.

(17) Zhang, Y.; Zhang, Y. Z.; Miller, D. C.; Bertrand, J. A.; Jen, S. H.; Yang, R.; Dunn, M. L.; George, S. M.; Lee, Y. C. Fluorescent Tags to Visualize Defects in Al_2O_3 Thin Films Grown Using Atomic Layer Deposition. *Thin Solid Films* **2009**, *517* (24), 6794–6797. https://doi.org/10.1016/j.tsf.2009.05.037.

(18) Hormozi Nezhad, M. R.; Aizawa, M.; Porter, L. A.; Ribbe, A. E.; Buriak, J. M. Synthesis and Patterning of Gold Nanostructures on InP and GaAs via Galvanic Displacement. *Small* **2005**, *1* (11), 1076–1081.

(19) Clark, W. E.; Whitby, K. T. Concentration and Size Distribution Measurements of Atmospheric Aerosols and a Test of the Theory of Self-Preserving Size Distributions. *J. Atmos. Sci.* **1967**, *24* (6), 677–687. https://doi.org/10.1175/1520-0469(1967)024<0677:CASDMO>2.0.CO;2.

(20) Hashimoto, S.; Tanaka, A. Alteration of Ti 2p XPS Spectrum for Titanium Oxide by Low-Energy Ar Ion Bombardment. *Surf. Interface Anal.* **2002**, *34* (1), 262–265. https://doi.org/10.1002/sia.1296.

(21) Shaner, M. R.; Fountaine, K. T.; Ardo, S.; Coridan, R. H.; Atwater, H. A.; Lewis, N. S. Photoelectrochemistry of Core–Shell Tandem Junction n–p + -Si/n-WO 3 Microwire Array Photoelectrodes. *Energy Environ. Sci.* **2014**, *7* (2), 779–790.

https://doi.org/10.1039/C3EE43048K.

(22) Yang, F.; Nielander, A. C.; Grimm, R. L.; Lewis, N. S. Photoelectrochemical Behavior of N-Type GaAs(100) Electrodes Coated by a Single Layer of Graphene. *J. Phys. Chem. C* **2016**, *120* (13), 6989–6995.

Supporting Information

Estimate of time to etch through GaAs wafer

The time to etch through the wafer was estimated using Eq. S3.1, assuming one pinhole orifice with a fixed diameter and isotropic spherical etching. The background current density (J_{before} = 0.05 mA cm^{-2}) was subtracted from the steady-state current density after the stepwise increase (J_{after} = 0.19 mA cm^{-2}). The electrode area was A_{el} = 0.068 cm^2. The thickness of the GaAs wafer was r_{etch} = 350 µm (ρ=5.32 g cm^{-3}, N_{GaAs} = 145 g mol^{-1}, the volume etched was $V_{etch} = \frac{1}{2}\left(\frac{4}{3}\pi r_{etch}^3\right)$)

$$T = \frac{V_{etch}\rho_{GaAs}M_{GaAS}N_{St}N_A}{(J_{after} - J_{before})A_{el}} \qquad \text{(Eq. S3.1)}$$

$$= \left(\frac{1}{2}\left(\frac{4}{3} * \pi * (350\ \mu m)^3\right)\right) * \left(\frac{1}{10000}\ \frac{cm}{\mu m}\right)^3$$

$$* \left(5.3176\ \frac{g}{cm^3}\right) * \left(\frac{1}{144.65}\ \frac{mol_{GaAs}}{g}\right) * \left(\frac{6\ mol_{e^-}}{1\ mol_{GaAs}}\right)$$

$$* \left(6.022 * 10^{23}\ \frac{e^-}{mol_{e^-}}\right) * \left(1.602 * 10^{-19}\frac{C}{e^-}\right)$$

$$* \left(1000\ \frac{mA}{s}\ \frac{1}{C}\right) * \left(\frac{1}{(0.19 - 0.05)}\ \frac{cm^2}{mA}\right)$$

$$* \left(\frac{1}{0.068\ cm^2}\right) * \left(\frac{1}{3600}\ \frac{hr}{s}\right) = \mathbf{55.64\ hr}$$

Dissolution of TiO_2

ICP-MS could not be utilized to monitor analytically the formation of pinholes in the TiO_2 layer by measuring the Ti concentration of the electrolyte. Assuming a pinhole has

approximately a 100 nm radius, and the complete formation of a pinhole through the entire layer creates a perfectly cylindrical void, the void would have a volume of $0.1^2 \times \pi \times 0.1 = 0.003\ \mu m^3$. This is an *equivalent* volume to 3.14×10^{-15} cm^3. TiO_2 has a density of 4.23 g cm^{-3}, resulting in this representative pinhole having lost a total mass of TiO_2 of 1.3×10^{-14} g = 1.3×10^{-5} ng. Titanium represents 60% of the mass of TiO_2, so the mass of titanium from one pinhole is approximately 8×10^{-6} ng. In a solution of 20 mL, this is a concentration of 4×10^{-4} ng L^{-1}, well below the minimum detection limit of ~1 ng L^{-1}. Furthermore, the sample is diluted with nitric acid during sample preparation, reducing the concentration by an additional order of magnitude.

Challenges in time-series scanning electron microscopy (SEM)

Although a time-series SEM can provide insights on the evolution of a new pinhole, sample preparation and transport can alter the surface chemistry and morphology of samples. Figure S3.8a shows current density as a function of time of p^+-GaAs/a-TiO_2-2000x under operation with a stepwise increase suggesting a new pinhole formation at 7.5 min. Figure S3.8b shows the corresponding SEM taken after the increase in current density.

The sample was taken out, rinsed with deionized water, and blow-dried with N_2 gas to prevent further corrosion from electrolyte contact. The SEM shows possible film breakage from the preparation step over the corrosion pit. Subsequently, when the sample was put back to electrochemical operation, a substantial increase in the corrosion current density was observed (from 0.7 mA cm^{-2} to 1.4 mA cm^{-2}). The increase in current density is likely due to an increase in the surface area from the torn a-TiO_2 film and oxidized exposed GaAs which is more soluble in 1.0 M KOH(aq). To accurately monitor the evolution of the pinhole, an operando SEM capability is needed to avoid changing the surface morphology and chemical state during the electrochemical operation.

Supporting Figures

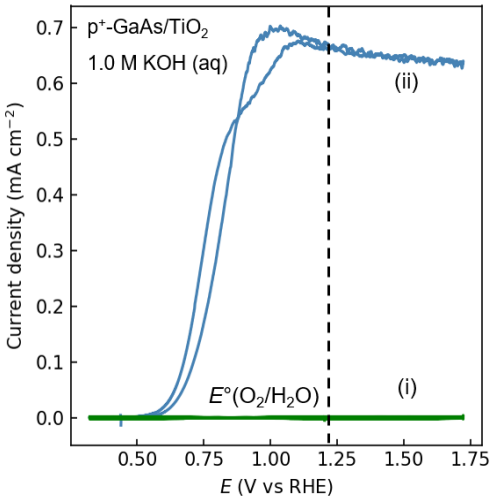

Figure S3.1. Current density vs. potential (*J*-*E*) behavior of p^+-GaAs samples coated with a-TiO_2-2000x (2000 ALD cycles) but without Ni (GaAs/a-TiO_2-2000x). The scan rate was 40 mV s^{-1}. Two types of electrochemical behaviors were observed for the GaAs/a-TiO_2-2000x samples: (i) no apparent corrosion current and (ii) substantial corrosion currents.

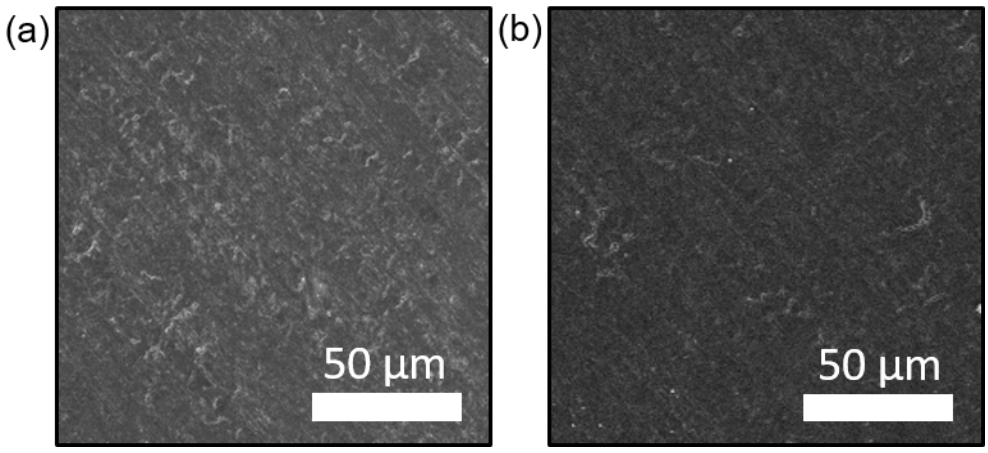

Figure S3.2. Scanning-electron micrographs of (a) a-TiO_2/Ti foil before Au deposition and (b) a-TiO_2/Ti after Au deposition.

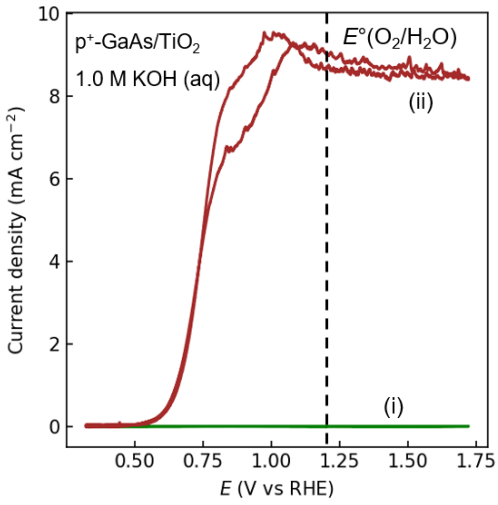

Figure S3.3. Current density as a function of time for p^+- GaAs samples coated with a-TiO_2 (2000 ALD cycles) but without Ni (GaAs/ a-TiO_2-2000x) at (i) 0 h and (ii) 1 h. The scan rate was 40 mV s^{-1}.

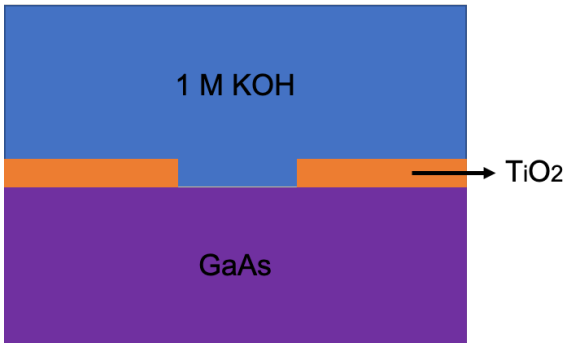

Figure S3.4. Schematic of the initial geometry used in COMSOL simulation (out of scale).

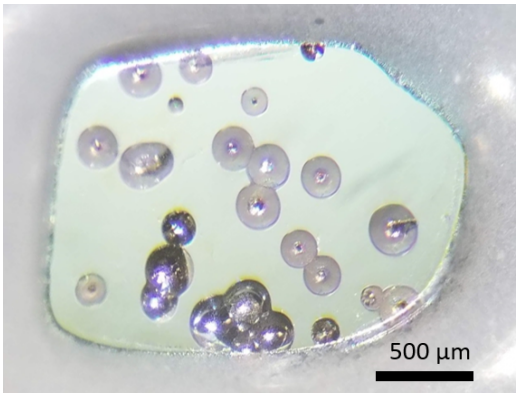

Figure S3.5. Micrograph of the p^+-GaAs/TiO_2-2000x after electrochemical testing.

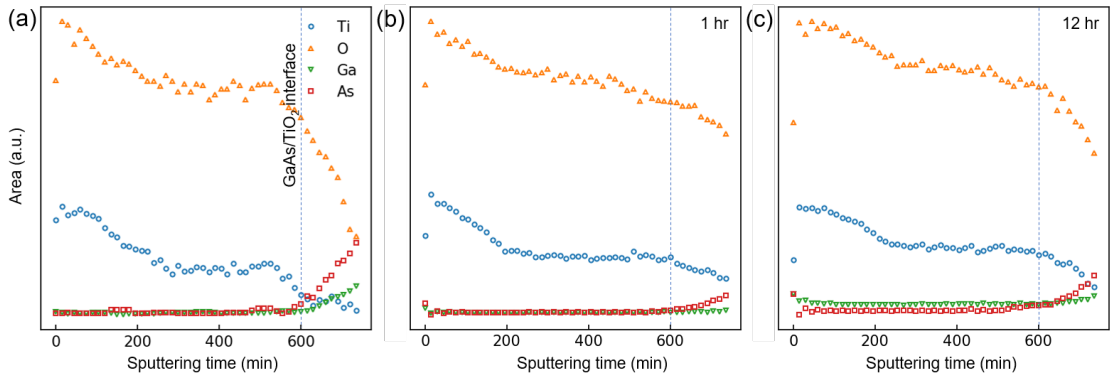

Figure S3.6. Area of under the peaks for Ti 2p (blue circles), O 1s (orange triangles), Ga 3d (green inverted triangles), and As 3d (red squares) signals as a function of sputtering time on p^+-GaAs/TiO_2-400x samples measured (a) before testing, (b) 1 h after testing, and (c) 12 h after testing.

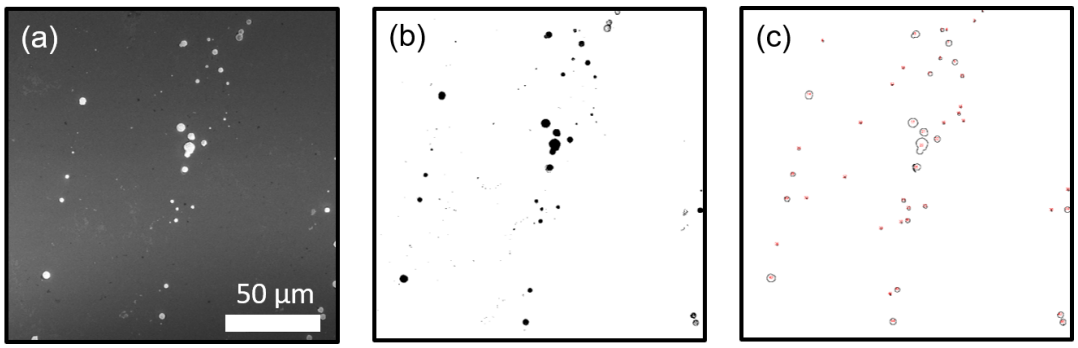

Figure S3.7. Image processing steps to determine the density of plated Au in pinholes (a) raw scanning-electron micrograph, (b) conversion to 8-bit image, and (c) outlines of the gold sites counted by the software.

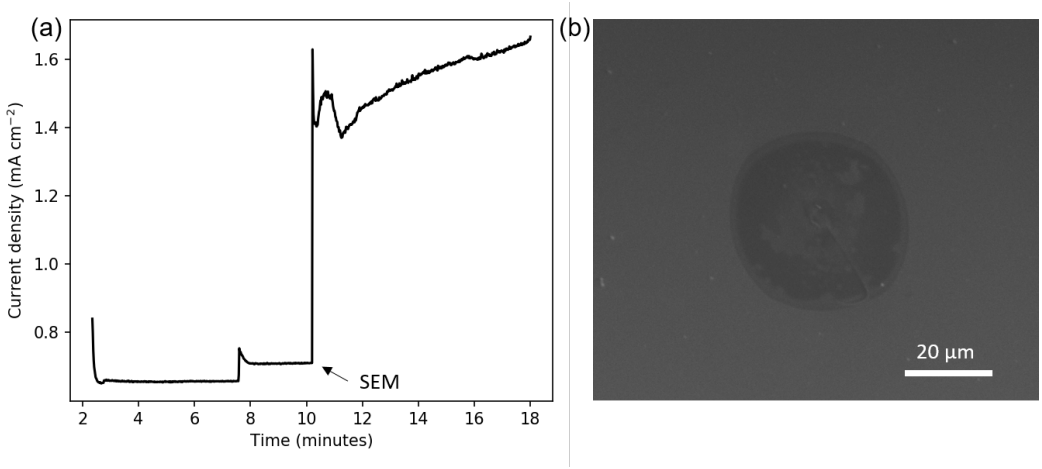

Figure S3.8. (a) Current density as a function of time of p^+-GaAs/a-TiO_2-2000x held at 1.13 V vs. RHE in 1.0 M KOH(aq). (b) the corresponding scanning-electron micrograph taken at ~10 min.

Chapter 4

GaAs MICRO-ISLAND ANODES PROTECTED BY AMORPHOUS TiO_2 FILMS MITIGATE CORROSION SPREADING DUE TO PITTING AND ENHANCE ANODE DURABILITY FOR WATER OXIDATION IN ALKALINE ELECTROLYTES

The following chapter discusses the evolution of defect spots and pinhole formation of a-TiO_2 and the fabrication of GaAs micro-island structures.

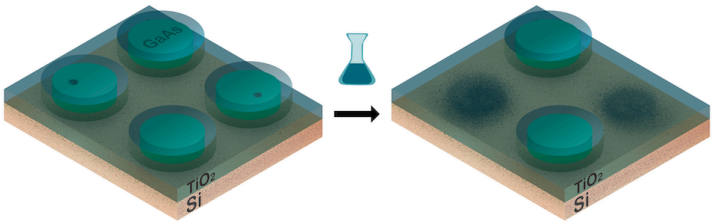

Content in this chapter is drawn from the following publication:

- **Buabthong, P.**, Evans, J., Rinaldi, K. Z., Kennedy, K. M., Fu, H. J., Ifkovits, Z. P., Kuo, T.-J., Brunschwig, B. S., Lewis, N. S. "GaAs Micro-island Anodes Protected by Amorphous TiO2 Films Mitigate Corrosion Spreading Due to Pitting and Enhance Anode Durability for Water Oxidation in Alkaline Electrolytes". *in preparation*.

Abstract

Micro-island structures of ~200 μm diameter GaAs circles were fabricated and used to spatially isolate defects from laterally spreading deleterious corrosion processes during electrochemical operation as an anode in aqueous alkaline electrolytes. The micro-island structures allowed measurement of the rate and distribution of pinhole formation on electrodes protected by amorphous titanium dioxide (*a*-TiO_2) films formed by atomic-layer deposition, and allowed for evaluation of short- and medium-term failure mechanisms to enable further enhancements in the durability of such electrode materials. Although no crystalline homogeneity was measured on the surface of the *a*-TiO_2 films, a limited number of defects were present in the *a*-TiO_2 layer and developed into new microscopic pinholes within the first 20 h of electrochemical operation. No new pinholes were observed to form after all of the defect spots had developed. The spatial distribution and rate of new pinhole formation showed that the defect spots were randomly distributed on the electrode surface. The *a*-TiO_2 film dissolved at a rate of < 13 nm per day, and hence intrinsic film dissolution was not the primary mode of pinhole formation or anode failure during the first 20 h of the electrochemical operation. The fabrication processes used to make the GaAs micro-island structures presented herein only utilized chemical etching and mechanical polishing, and consequently should be readily transferrable to the fabrication of the more complicated np^+-GaAs structures and beneficially applied to enhance the stability of other semiconductor electrodes that have a primary failure mode of pit corrosion through defects in *a*-TiO_2 protective coatings.

Introduction

Small band gap semiconductors undergo either passivation or corrosion by dissolution while anodically evolving oxygen from water.[1–5] The most appropriate strategies for mitigating corrosion will differ depending on the underlying corrosion mechanism.[1] For example, amorphous TiO_2 (*a*-TiO_2) films deposited by atomic layer deposition (ALD) facilitate hole conduction and have extended the lifetime of n-Si photoanodes to >1000 h of continuous operation, because Si undergoes passivation at any defect sites in the *a*-TiO_2 protection layer.[6] Macroscopic samples of GaAs anodes and photoanodes show limited lifetimes under the same conditions because GaAs undergoes pit corrosion at defect sites in *a*-TiO_2 films.[6,7] The short-term failure mode of *a*-TiO_2-protected GaAs photoanodes has been ascribed to pinholes associated with atmospheric particulates present during deposition of the *a*-TiO_2 film, but diffusion of OH^- through metastable crystalline regions has also been proposed as a mechanism for the formation of pinholes in *a*-TiO_2.[7–10] Such pinholes and extrinsic film defects are unlikely to be completely eliminated over large areas in any large-scale film deposition process.[7] *a*-TiO_2-protected GaAs nanowires are stable for over 600 h of continuous operation as photoanodes for water oxidation because the defects are electrically isolated and can not physically propagate a failure in the protection layer across the entire photoelectrode material.[11]

If the pinhole density is sufficiently low, a substantial fraction of spatially isolated macroscopic areas of a photoanode sample should exhibit extended stability while oxidizing water to O_2(g).[12] Galvanic deposition of Au allows for staining of pinholes in *a*-TiO_2 films on GaAs, and indicates that pinhole densities in the *a*-TiO_2 films can readily be reduced to below 1 defect per 10^{-3} cm^2 even if the *a*-TiO_2 films are deposited under ambient atmosphere in the laboratory.[8] Consequently, we describe herein the use of ~200 μm diameter circular islands of TiO_2-protected GaAs anodes to demonstrate the benefits of spatially isolating extrinsic defects in protected semiconductor electrodes that undergo pit corrosion, as well as to further define and understand the short- and mid-term failure modes of *a*-TiO_2-protected GaAs anodes for production of O_2 from water.

Results and Discussions

Crystallinity of amorphous a-TiO_2

Figure S4.1 shows a representative Raman spectrum of a GaAs sample coated with 800 cycles of *a*-TiO_2 (GaAs/*a*-TiO_2-800x) from tetrakis(dimethylamido)-titanium (TDMAT) as the Ti source. The sets of the red (short-dash) and blue (long-dash) lines show the Raman shift positions for the crystalline anatase and rutile structures, respectively. The two peaks at ~253 cm^{-1} and 275 cm^{-1} correspond to the Raman shifts from the GaAs substrates.[13]

No peaks ascribable to crystalline TiO_2 were observed from films deposited by ALD from TDMAT at 150 °C. The observed homogeneity contrasts with crystalline regions observed in TiO_2 films that have been deposited using different precursors and deposition temperatures than those used herein. [9,10] Planar p^+-GaAs samples that had been coated with *a*-TiO_2 films grown under these conditions (TDMAT, 150 °C) with minimal pinholes from atmospheric particulate contamination nevertheless develop pinhole sites after ~10 h of electrochemical operation.[8] Defect spots equivalent to those observed as a metastable crystalline phase,[9,10] which manifest as new pinholes developed during electrochemistry, likely exist on the film but are not evident as crystalline regions detectable using Raman spectroscopy.

Fabrication of micro-island GaAs structures

Micro-island structures of ~200 μm diameter circular p^+-GaAs were fabricated and explored as a strategy to spatially isolate potential defects and minimize the propagation of pit corrosion sites across the electrode sample. Figure 4.1 shows a schematic of the steps used to fabricate the micro-island structures, with the detailed fabrication procedures provided in the Supporting Information. Briefly, p^+-GaAs wafers were cleaned and dried (Fig. 4.1a). A 30-nm thick Ni mask was then sputtered using a micro-pattern stencil (an array of 200-μm-diameter circles on a 350-μm pitch) (Fig. 4.1b). The sample was then

etched to achieve 30-µm-tall micro-island structures (Fig. 4.1c). Cross-sectional scanning electron micrographs (SEM) confirmed that this chemical etching process yielded sharp and anisotropic etching in the (100) direction (Fig. S4.2a).

After removal of the Ni mask, the sample was flipped and affixed to a polishing stub by crystal bond, with the island structures facing downward (Fig. 4.1d). The backside of the samples were then mechanically polished and thinned until the underlying island structures were visible (Fig. 4.1e). The stub was transferred to the sputterer to deposit back ohmic contact. Ag epoxy was then used to attach the stub to a cleaned p^+-Si substrate (Fig. 4.1f). The sample was removed from the polishing stub by sonication and was then rinsed rigorously in acetone to remove any residual crystal bond (Fig. 4.1g). After etching in HCl(aq) to remove any residual oxide from the GaAs micro-islands, the sample was transferred to the ALD chamber and *a*-TiO_2 was deposited (Fig. 4.1h). To separate the electrolyte from the area around GaAs micro-islands, the sample was coated with a thin layer of polydimethylsiloxane (PDMS).

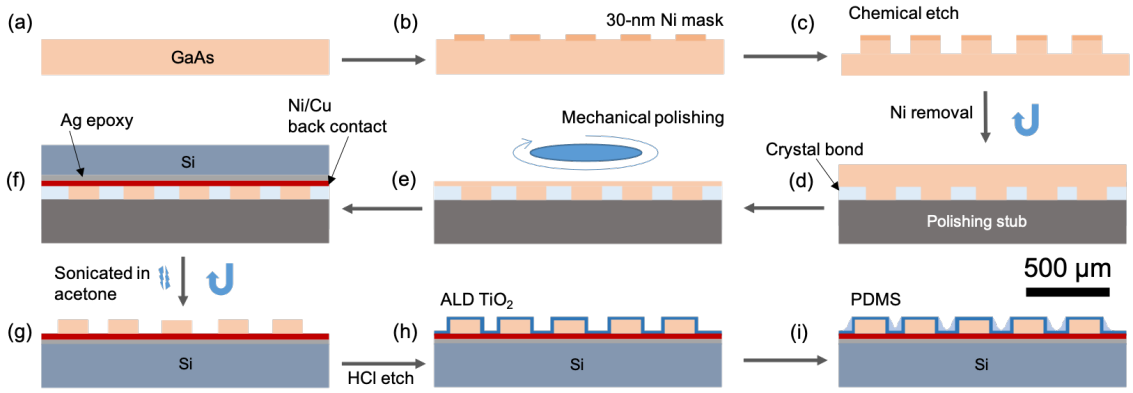

Figure 4.1. A schematic overview of the fabrication processes (a-i) for p^+-GaAs micro-island structures.

Top-down SEM images showed that the majority of the islands retained the circular shape from the stencil. Some islands contained a few indentations at the circular edges,

which is likely due to improper adhesion of the Ni mask at the edge of the mask (Fig S4.2). Cross-sectional SEM images of the final structure also showed that the PDMS film fully coated the area around the islands but left the top surface of the islands exposed (Fig. S4.2c-d). The final micro-island structures were ~15-μm tall, slightly shorter than the original etched structure (Fig. S4.2a) likely due to the thinning step.

Formation of pinholes during electrochemistry

In an alkaline solution, GaAs substrates undergo dissolution at open-circuit:

$$GaAs_{(s)} + 10OH^-_{(aq)} \rightarrow GaO_3^{3-}{}_{(aq)} + AsO_2^-{}_{(aq)} + 6e^- + 5H_2O_{(l)} \quad \text{(Eq. 4.1)}$$

$$6H_2O_{(l)} + 6e^- \rightarrow 3H_{2(g)} + 6OH^-_{(aq)} \quad \text{(Eq. 4.2)}$$

a-TiO_2-coated p^+-GaAs micro-island structures (with no Ni) were used to minimize possible effects from the Ni overlayer that could confound interpretation of the corrosion kinetics of *a*-TiO_2, such as loss of Ni catalyst or the Ni film providing an additional protective coating to the *a*-TiO_2. The absence of a thin Ni catalyst layer has been shown previously to have no detectable effect on the corrosion kinetics of GaAs.[8] Figure 4.2 shows the current density *vs.* potential behavior of (a) bare p^+-GaAs micro-island structures and (b) p^+-GaAs micro-island structures coated with 2000x-*a*-TiO_2 in contact with 1.0 M KOH(aq) in the dark. For the bare micro-island structures, as the potential (*E*) was swept positive of 0.6 V *vs.* the reversible hydrogen electrode (RHE), the current density (*J*) increased from ~0 mA cm^{-2} to ~26 mA cm^{-2}. In contrast, the p^+-GaAs micro-island structures coated with 2000 cycles *a*-TiO_2 (2000x-TiO_2) did not show substantial corrosion current throughout the potential range. The *J-E* characteristics of the micro-island structures are in good accord with the *J*-behavior previously reported for planar p^+-GaAs electrodes.[8] Hence, no substantial potential drop was present across the micro-island device stack, ensuring that the micro-islands/electrolyte interface was essentially an isopotential surface.

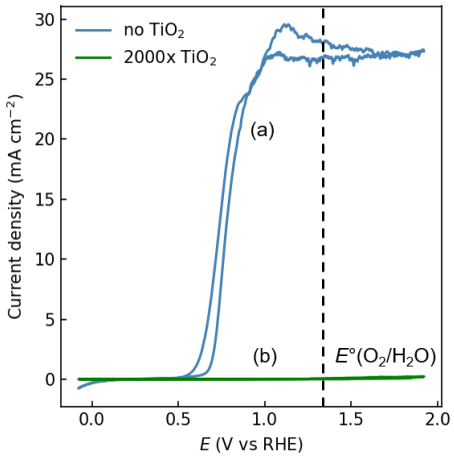

Figure 4.2. Current density vs potential (*J*-*E*) behavior of p^+-GaAs micro-island structures (a) without and (b) with amorphous a-TiO_2 (GaAs/a-TiO_2-2000x). The scan rate was 40 mV s^{-1}.

p^+-GaAs micro-island electrodes were held at $E = 1.13$ V *vs.* RHE and pinhole formation during electrochemistry was assessed with an optical microscope that allowed for monitoring the morphological evolution of the electrode surface. p^+-GaAs micro-island structures coated with 2000x of *a*-TiO_2 (GaAs/*a*-TiO_2-2000x) were used to minimize the initial pinhole density arising from atmospheric particulates during the ALD film deposition process.[8] Detailed procedures for the analysis are provided in the Supporting Information. Briefly, the island array was mapped onto a grid for spatial reference. Each frame was then compared to the previous time step, and any newly failed islands were recorded manually.

Figure 3a shows the number of remaining micro-islands on the GaAs/*a*-TiO_2-2000x electrode surface as a function of time during electrochemical operation. Immediately after starting the electrochemical experiment, some micro-islands failed, leaving 98.50±0.22% of the islands intact on the surface. Between 1 and 20 h of operation, more micro-islands gradually failed, leaving 95.88±0.26% of the micro-islands remaining intact on the electrode surface. After 20 h, the number of islands on the surface remained constant until ~35 h, at which point substantially more micro-islands began to fail. Figure 4.3b shows an

illustration of the micro-island array on a representative electrode (Fig. S4.3a), with the color indicating the time-to-failure of each micro-island. The sequence and the spatial distribution at which each micro-island failed appeared to be stochastic, with no particular cluster of micro-islands failing before any other set of islands (Fig 4.3b). The group of micro-islands that failed immediately after starting the electrochemical experiment is likely due to residual pinholes from atmospheric particulates (Fig 4.3a). In contrast, the micro-islands that failed between 1 and 20 h of operation failed more gradually, and almost no micro-islands failed after that time, indicating that the micro-islands corroded as a result of pinhole sites that are most likely developed from a limited number of pre-existing defect spots. The defect spots only developed into pinholes after being in contact with the electrolyte, and once all of the pre-existing defect spots had developed, no more new pinholes or failed micro-islands were observed. The sparse distribution of the failed islands (Fig. 4.3b) also suggests that the micro-islands most likely failed from new pinholes developed from defect spots as opposed to propagation of defective regions from neighboring failed micro-islands.

After ~35 h of operation, the increased failure rate of the micro-islands is likely due to corrosion initiated by failure of the underlying Ag epoxy layer. The optical micrograph of the electrode surface after 45 h of operation showed that the micro-islands had failed in a cluster at the top-left area of the electrode (Fig. S4.3b), which is expected if the electrolyte had corroded the micro-islands from the bottom layer. The cross-sectional SEM of the micro-islands that failed after 35 h of operation (Fig. S4.3c,d) showed the PDMS layer remained intact both at the area with no micro-islands as well as at the sealing interface between micro-islands and the PDMS film. The observations were consistent with a failure mode in which the electrolyte seeped through the slightly porous underlying Ag epoxy layer as opposed to failure from the sidewalls of the micro-islands. Hence, further improvements in electrode stability should be obtainable if the porosity of the adhesion layer is reduced.

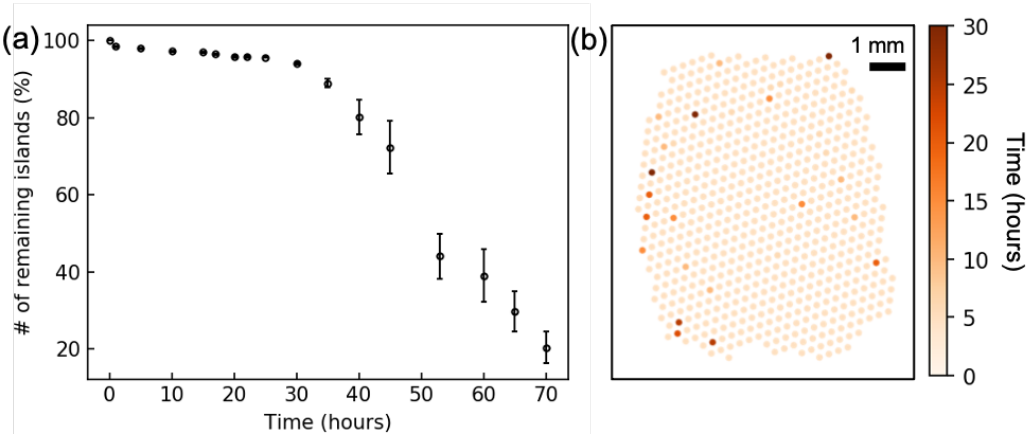

Figure 4.3. (a) The number of remaning islands as a function of time. (b) illustration of GaAs islands positions on the electrode surface shown in Fig S2. with the color representing the time at which each island fails.

TiO_2 dissolution as the origin of the pinholes

In addition to intrinsic defects in the *a*-TiO_2 film, dissolution of the *a*-TiO_2 layer could also constitute a failure mode as a result of the formation of new pinholes during electrochemical operation. Measurement of the rate of dissolution of Ti on *a*-TiO_2-coated GaAs is difficult due to the rapid dissolution of GaAs in 1.0 M KOH(aq).[8] Hence, herein *a*-TiO_2 deposited under nominally identical conditions but onto passivating p^+-Si surfaces was used to allow measurements of the Ti dissolution rate. Figure S4.4 shows the Ti dissolution as a function of time for *a*-TiO_2-coated p^+-Si (p^+-Si/TiO_2-1500x) held at the open-circuit potential (E_{oc}, black-empty circles) or held cyclically at E = 1.63 V *vs.* RHE for 6 h followed by $E = E_{oc}$ for 18 h (cycled, green-filled circles). The dissolution of Ti species in the electrolyte increased linearly with time to 12.58 nm and 8.74 nm at 24 h, respectively, under either potential condition, and increased more slowly thereafter.

Although the *a*-TiO_2 layer dissolved gradually over time under both conditions, <13 nm of the film dissolved within the first 24 h in either case In contrast, in the same period, 4.12±0.26% of the micro-island structures coated 2000x *a*-TiO_2 (110 nm) failed,

indicating that dissolution of the *a*-TiO_2 was not the dominant mode for the formation of new pinholes during this initial period (<30 h) of electrochemical operation.

Intrinsic vs Extrinsic Failure Modes of Semiconductor Anodes Protected by a-TiO_2 Films

Intrinsic failure modes of *a*-TiO_2 protection layers deposited by ALD permit extended photoelectrode operation in excess of months under simulated 1 Sun of illumination, as confirmed by observations that Si microwire arrays protected by *a*-TiO_2 sustain the photoanodic oxidation of water to O_2(g) in 1.0 M KOH(aq) for over 1000 h of continuous operation.[14] Si photoanodes undergo passivation in alkaline media by formation of Si oxide, and thus are able to provide extended production of O_2(g) even if extrinsic defects are present or are formed in the TiO_2 protection layer. Protective electrolytes can moreover be beneficially used to mitigate corrosion processes in the dark under open-circuit conditions as well as under continuous illumination.[15] The benefits of operating photoanodes under passivating conditions are also demonstrated by the behavior of p^+n-InP photoanodes operated at near-neutral pH conditions, under which a passsivating oxide forms. Under such conditions, p^+n-InP photoanodes protected by NiO_x exhibit stable operation for photoanodic O_2 evolution on macroscopically sized electrodes, whereas NiO_x protected n-InP photoanodes exhibit catastrophic failure after ~1-2 days of continuous operation in 1.0 M KOH(aq), in which the semiconductor electrode material exhibits corrosion by dissolution and pitting at defect sites.[16] Staining of extrinsic defect sites on GaAs anodes has confirmed that the short-term failure mechanism on *a*-TiO_2-protected GaAs results from pinholes in the *a*-TiO_2 film, and has revealed that the low spatial density of these defects can be achieved by routine deposition and fabrication procedures in low atmospheric ambients in the laboratory.[8] The >600 h stability under 1 Sun illumination of n-GaAs nanowire arrays protected by *a*-TiO_2 films confirms the benefits associated with suppression of short-term failure modes due to pit corrosion by spatial isolation of the semiconducting light absorber material.[11] The work herein provides a general strategy for mitigating failure due to extrinsic defects in protection layers, involving etching and

spatially isolating macroscopic areas of a protected semiconductor electrode, and underscores the improvements in durability that can be obtained through understanding and then systematically mitigating the failure modes of semiconductors that undergo different types of corrosion or passivation processes in contact with electrolytes of concern for solar fuels production.

Conclusions

Raman spectroscopy showed uniform lack of crystallinity throughout the *a*-TiO_2 layers grown by ALD with TDMAT at 150 °C, but the TiO_2 protection layers nevertheless contained defects that later developed into pinholes during electrochemical operation. GaAs micro-islands that were fabricated using a combination of chemical etching and mechanical polishing allowed for quantification of the evolution of the defects on the films as well as analysis of the failure modes for samples that spatially isolated defects from propagating laterally across macroscopic regions of the GaAs electrode. Analysis of the failed micro-islands on such GaAs structures suggests that the new pinholes that formed during electrochemical operation developed from a limited number of pre-existing defect regions in the *a*-TiO_2 film. These defect regions were randomly distributed across the electrode surface. ICP-MS measurements indicated that dissolution of the *a*-TiO_2 was not the predominant failure mode or mechanism of pinhole formation during the electrochemistry. As opposed to growth from a patterned seeding layer, a straightforward etching process was used to define the micro-island structures, so the processes described in this work could be beneficially translated to fabrication of micro-islands structures on more complicated GaAs stacks, such as p^+n-GaAs homojunction devices, while achieving extended stability and electrode durability as well as high performance even for samples that have pinholes in protective electrode coatings.

References

(1) Bae, D.; Seger, B.; Vesborg, P. C. K.; Hansen, O.; Chorkendorff, I. Strategies for Stable Water Splitting via Protected Photoelectrodes. *Chem. Soc. Rev.* **2017**, *46* (7), 1933–1954. https://doi.org/10.1039/C6CS00918B.

(2) Jin, J.; Walczak, K.; Singh, M. R.; Karp, C.; Lewis, N. S.; Xiang, C. An Experimental and Modeling/Simulation-Based Evaluation of the Efficiency and Operational Performance Characteristics of an Integrated, Membrane-Free, Neutral PH Solar-Driven Water-Splitting System. *Energy Environ. Sci.* **2014**, *7* (10), 3371–3380. https://doi.org/10.1039/C4EE01824A.

(3) Pourbaix, M. *Atlas of Electrochemical Equilibria in Aqueous Solutions*; 1974. https://doi.org/10.4028/www.scientific.net/MSF.251-254.143.

(4) Gerischer, H. Electrolytic Decomposition and Photodecomposition of Compound Semiconductors in Contact with Electrolytes. *J. Vac. Sci. Technol.* **1978**, *15* (4), 1422–1428. https://doi.org/10.1116/1.569800.

(5) Allongue, P.; Blonkowski, S. Corrosion of III–V Compounds; a Comparative Study of GaAs and InP. *J. Electroanal. Chem. Interfacial Electrochem.* **1991**, *317* (1–2), 77–99. https://doi.org/10.1016/0022-0728(91)85004-9.

(6) Hu, S.; Shaner, M. R.; Beardslee, J. A.; Lichterman, M.; Brunschwig, B. S.; Lewis, N. S. Amorphous TiO_2 Coatings Stabilize Si, GaAs, and GaP Photoanodes for Efficient Water Oxidation. *Science* **2014**, *344* (6187), 1005–1009. https://doi.org/10.1126/science.1251428.

(7) Verlage, E.; Hu, S.; Liu, R.; Jones, R. J. R.; Sun, K.; Xiang, C.; Lewis, N. S.; Atwater, H. A. A Monolithically Integrated, Intrinsically Safe, 10% Efficient, Solar-Driven Water-Splitting System Based on Active, Stable Earth-Abundant

Electrocatalysts in Conjunction with Tandem III–V Light Absorbers Protected by Amorphous TiO_2 Films. *Energy Environ. Sci.* **2015**, *8* (11), 3166–3172. https://doi.org/10.1039/C5EE01786F.

(8) Buabthong, P.; Ifkovits, Z. P.; Kempler, P. A.; Chen, Y.; Nunez, P. D.; Brunschwig, B. S.; Papadantonakis, K. M.; Lewis, N. S. Failure Modes of Protection Layers Produced by Atomic Layer Deposition of Amorphous TiO 2 on GaAs Anodes. *Energy Environ. Sci.* **2020**, *13* (11), 4269–4279. https://doi.org/10.1039/D0EE02032J.

(9) Ros, C.; Carretero, N. M.; David, J.; Arbiol, J.; Andreu, T.; Morante, J. R. Insight into the Degradation Mechanisms of Atomic Layer Deposited TiO_2 as Photoanode Protective Layer. *ACS Appl. Mater. Interfaces* **2019**, *11* (33), 29725–29735. https://doi.org/10.1021/acsami.9b05724.

(10) Yu, Y.; Sun, C.; Yin, X.; Li, J.; Cao, S.; Zhang, C.; Voyles, P. M.; Wang, X. Metastable Intermediates in Amorphous Titanium Oxide: A Hidden Role Leading to Ultra-Stable Photoanode Protection. *Nano Lett.* **2018**, *18* (8), 5335–5342. https://doi.org/10.1021/acs.nanolett.8b02559.

(11) Shen, X.; Yao, M.; Sun, K.; Zhao, T.; He, Y.; Chi, C.-Y.; Zhou, C.; Dapkus, P. D.; Lewis, N. S.; Hu, S. Defect-Tolerant TiO_2 -Coated and Discretized Photoanodes for >600 h of Stable Photoelectrochemical Water Oxidation. *ACS Energy Lett.* **2021**, *6* (1), 193–200. https://doi.org/10.1021/acsenergylett.0c02521.

(12) Kennedy, K. M.; Kempler, P. A.; Cabán-Acevedo, M.; Papadantonakis, K. M.; Lewis, N. S. Primary Corrosion Processes for Polymer-Embedded Free-Standing or Substrate-Supported Silicon Microwire Arrays in Aqueous Alkaline Electrolytes. *Nano Lett.* **2021**. https://doi.org/10.1021/acs.nanolett.0c04298.

(13) Mooradian, A.; Wright, G. B. First Order Raman Effect in III–V Compounds. *Solid State Commun.* **1966**, *4* (9), 431–434. https://doi.org/10.1016/0038-1098(66)90321-8.

(14) Shaner, M. R.; Hu, S.; Sun, K.; Lewis, N. S. Stabilization of Si Microwire Arrays for Solar-Driven H2O Oxidation to O_2(g) in 1.0 M KOH(Aq) Using Conformal Coatings of Amorphous TiO2. *Energy Environ. Sci.* **2015**, *8* (1), 203–207. https://doi.org/10.1039/C4EE03012E.

(15) Fu, H. J.; Moreno-Hernandez, I. A.; Buabthong, P.; Papadantonakis, K. M.; Brunschwig, B. S.; Lewis, N. S. Enhanced Stability of Silicon for Photoelectrochemical Water Oxidation through Self-Healing Enabled by an Alkaline Protective Electrolyte. *Energy Environ. Sci.* **2020**, *13* (11), 4132–4141. https://doi.org/10.1039/D0EE02250K.

(16) Sun, K.; Kuang, Y.; Verlage, E.; Brunschwig, B. S.; Tu, C. W.; Lewis, N. S. Sputtered NiO_x Films for Stabilization of p^+ n-InP Photoanodes for Solar-Driven Water Oxidation. *Adv. Energy Mater.* **2015**, *5* (11), 1402276. https://doi.org/10.1002/aenm.201402276.

Supporting Information

Experimental Methods

Materials and chemicals

Water with a resistivity ρ > 18 MΩ·cm was obtained from a Barnstead Millipore purification system. All chemicals were used as received, including potassium hydroxide (TraceSELECT, ≥30% in water, Honeywell Fluka), buffered oxide etchant (BOE, 6:1 NH_4F to HF, Transene Company, Inc.), gallium-indium eutectic (Alfa Aesar, 99.99%), nickel etchant (Ni Etch TFG, Transene Company, Inc.), GaAs etchant (GA Etch 300, Transene Company, Inc.), polydimethylsiloxane (PDMS) (Sylguard), PDMS curing agent (Sylguard 184), toluene (Millipore Sigma, GR ACS), and Ag epoxy adhesive (MG Chemicals, 8331). Crystalline single-side polished (100)-oriented, 350±25-μm-thick p^+-GaAs substrates were degenerately doped with zinc to a majority-carrier density of 0.5-5×10^{19} cm^{-3} (AXT Inc.). (100) oriented, 500-μm-thick p^+-Si wafers were degenerately doped with boron, and had a resistivity of 0.001-0.005 Ω cm (Addison Engineering).

Preparation of substrates

The GaAs wafers were cleaned with 10% (1.16 M) HCl(aq) for 30 min to remove native oxide on the surface.[1] The Si wafers were submerged in BOE for 1 min to remove native oxide. The samples were then rinsed with copious amounts of deionized H_2O and dried using a stream of N_2(g).

Atomic layer deposition (ALD) of TiO_2 thin films

a-TiO_2 films were grown using tetrakis(dimethylamido)-titanium (TDMAT). For *a*-TiO_2 films prepared from the TDMAT precursor, a Cambridge Nanotech S200 or Oxford Instruments FlexAL ALD system was used for deposition outside and inside the cleanroom. Each ALD cycle consisted of a 0.10 s exposure to TDMAT (Sigma-Aldrich, 99.999%), a N_2(g) (Airgas, 99.999%) purge, a 0.015 s exposure to H_2O, and a final N_2(g)

purge. Research-grade 20 sccm N_2(g) was used for the N_2(g) purges, and each N_2(g) purge was 15 s in duration. During the deposition, the substrate and the TDMAT precursor were heated to 150 °C and 75 °C, respectively, while the H_2O remained at room temperature. Most samples were prepared with 2000 ALD cycles to produce films that were nominally 110 nm thick. The film thickness and refractive index were measured via spectroscopic ellipsometry (J.A. Woollam Co., alpha-SE) and were fit to a Cauchy model.

Radio-frequency sputtering deposition

A radio-frequency sputtering system (AJA International Inc.) was used to deposit Ni and Cu for back ohmic contacts to p^+-GaAs. The base pressure was $<1\times10^{-7}$ Torr, and the deposition pressure was 5 mTorr. A radio-frequency (rf) power of 100 W was maintained during the deposition.

Electrode fabrication

Electrodes were fabricated by using a scribe to cleave the samples into pieces of ~0.1 cm^2 in geometric area. Ohmic contact was made by sequentially depositing Ni/Cu films onto the unpolished back sides of the p^+-GaAs samples.[2] The back contact to the sample was affixed to a Cu wire with Ag paste. The Cu wire was threaded through a glass tube (Corning Incorporation, Pyrex tubing, 7740 glass), and all but the front of the sample was encapsulated with either Loctite epoxy (Hysol 9462) or Gorilla Glue (Gorilla Glue, Co). After curing, the electrode was scanned with an Epson scanner (V19) and analyzed with ImageJ to determine the area of the exposed region.[3]

Scanning electron microscopy

Scanning electron micrographs (SEMs) were obtained with an FEI Nova NanoSEM 450 at an accelerating voltage of 5.00 kV with a working distance of 5 mm and an in-lens secondary electron detector.

TiO_2 dissolution

To measure the dissolution of ALD TiO_2, a film of nominally ~80-nm-thick (1500 cycles) of TiO_2 was deposited onto p^+-Si. In-Ga was applied as the back contact and Ag paste was applied to affix the sample onto a Cu wire. To minimize residual TiO_2 contamination from the Hysol epoxy, Gorilla Glue instead of Hysol 9462 epoxy was used to seal to the sample from the electrolyte.

The electrodes were evaluated in 30 mL of 1.0 M KOH(aq) and were either maintained at the open-circuit potential (E_{oc}) or at E = 1.63 V vs RHE. 1 mL aliquots were taken at each interval. No electrolyte was replenished during the experiment. ICP-MS was used to analyze the Ti dissolution products in the aliquots.

Inductively-coupled plasma mass spectroscopy

Inductively coupled plasma mass spectrometry (ICP-MS) data were collected using an Agilent 8800 Triple Quadrupole ICP-MS system. ICP-MS samples were collected periodically throughout electrochemical corrosion experiments. Samples were diluted 50x with 2% (0.32 M) nitric acid before analysis. ICP-MS concentration standards were made with serial dilutions of a known concentration standard (Sigma-Aldrich) with 2% nitric acid. Each concentration standard had KOH added in a 50:1 volumetric ratio of nitric acid: KOH (2%, 1.0 M, respectively) to match the solution matrix of the ICP-MS samples. Quantification was verified by independently making four additional samples of known concentrations and analyzing the samples at the beginning, middle, and end of all ICP-MS analysis. ICP-MS results were only used when the samples of known concentration were measured to be consistent throughout the ICP-MS run. The samples of known concentration were also made on a mass basis and were matrix-matched with the same 50 nitric acid:1 KOH volumetric ratio as both the unknown samples and the concentration standards. The total amount of dissolved Ti from the electrodes was then calculated and normalized to the geometric electrode area.

X-ray photoelectron spectroscopy

X-ray photoelectron spectroscopy (XPS) was performed using a Kratos Axis Ultra system with a base pressure of 1×10^{-9} torr in the analysis chamber. A monochromatic Al Kα source was used to irradiate the sample with X-rays (1486.7eV) at 150 W. A hemispherical analyzer oriented for detection normal to the sample surface was used for maximum depth sensitivity. The data were analyzed using CasaXPS computer software.

XPS data were obtained ex-situ, i.e., after a short sample transfer through air, which could potentially confound linking the surface composition and oxidation states found in ultra-high vacuum to the surface conditions present during electrochemistry.

Electrochemical characterization

Electrochemical data were obtained using a BioLogic SP-200 potentiostat in a three-electrode configuration with 1.0 M KOH(aq) as the electrolyte. A Hg/HgO electrode (CH Instruments, Inc., CHI-152) was used as the reference electrode for the alkaline solution. A carbon rod (Strem Chemicals, 99.999%) inside a porous fritted gas dispersion tube (Sigma Aldrich, Z408727) was used as the counter electrode. *J-E* data were collected between -0.6 V and 0.8 V vs. Hg/HgO at a 20-mV s^{-1} scan rate. Chronoamperometry (CA) data were collected every 1 s while holding the electrode potential at 0.212 V vs. Hg/HgO, unless noted otherwise.

Raman spectroscopy methods

Raman spectra were collected with a Renishaw inVia Raman microprobe (Renishaw, Wotton-under-Edge, United Kingdom) equipped with a Leica DM 2500 M microscope (Leica Microsystems, Wetzlar, Germany), a Leica N Plan 50x objective (numerical aperture = 0.75), a 1800 lines mm^{-1} grating, and a 2D CCD detector configured in a 180° backscatter geometry. A 532 nm diode-pumped solid-state (DPSS) laser (Renishaw RL532C50) was used as the excitation source and a 2 mW radiant flux was incident on the surface of the sample. A line-focus lens was utilized to transform the

circular incident beam in one dimension to generate an ~50 μm wide line at the sample. Spatially-resolved data were acquired by both rasterizing the sample underneath the line-shaped excitation and dispersing scatter collected along the line over one axis of the detector, perpendicular to the direction of frequency dispersion. Resolution in the direction perpendicular to the long axis was defined by the mechanical sample movement and in the direction parallel was defined by the pixel size of the detector. The sampling resolution was consequently 1.5 × 1.5 μm^2. Three 100 × 100 μm^2 Raman maps were obtained for each sample (2000x, 800x, 200x), to probe the uniformity across the sample.

Detailed Fabrication Procedures

General Considerations on the Overall Fabrication Processes

p^+-GaAs wafers were initially cleaned with 10% HCl (1.16 M) for 30 min and bonded onto p^+-Si substrates that had been cleaned with BOE for 1 min. The bonding process was performed in an environmentally controlled cleanroom, repeated from previously reported room-temperature direct wafer bonding.[4–6] The GaAs/Si stacks were then mechanically thinned and polished to reduce the thickness of the p^+-GaAs to ~50 μm. The mask was subsequently deposited onto the stack, followed by the chemical etching process. The mechanical thinning and polishing step was detrimental to the p^+-GaAs surface and led to a substantial amount of micro-/nano-scale etch pits (Fig. S4.5a). These etch pits eventually led to corrosion within the masked areas, thus resulting in ill-defined micro-island structures. Additionally, in some cases, the etch pits within the Ni masked areas may lead to metal-assisted chemical etching[7] in which the Ni masks catalyze the etching process under the mask area as opposed to the area outside the masked area (Fig. S4.5b). Hence, the micro-island etching was made to be the first process step, ensuring that the GaAs etchant only reacted with a pristine p^+-GaAs (100) surface, thus leading to sharp and well-defined micro-island structures (Fig. S4.2a).

Etching

A Ni mask was sputtered onto cleaned p^+-GaAs substrates for 30 min with a micro-island pattern stencil (an array of 200-μm-diameter circle and 350-μm pitch), yielding a mask thickness of ~30 nm. The samples were mounted onto a thin glass slide using nail polish. A bath containing a commercial GaAs etchant (Transene, GA Etch 300) was heated to 45 °C and stirred at 600 rpm. The masked samples were then submerged in the etchant for 30 min to obtain ~ 30-μm-tall micro-island structures.

Due of the lower precision over the control of the etchant transport in wet etch compared to dry etch, the chemical etching process might have higher tendency for undesirable isotropic etching and inconsistency in the etched structures (Fig. S4.6a,b). The optimal setup for the etching bath was obtained when the samples were placed off-center and slightly tilted to facilitate transport of the etchant (Fig. S4.6c,d)

Thinning

Before the thinning process, the Ni masks were removed from the surface by etching for 2 min in a commercial Ni etchant (Transene, Ni Etch TFG). Optical microscopy images of the samples coated with patterned Ni masks before and after the etch showed that the etchant entirely removed the masks while leaving the underlying p^+-GaAs substrate intact (Fig. S4.7a,b). X-ray photoelectron spectroscopy (XPS) of the Ni 2p region on the sample before and after the Ni etch also confirmd that the majority of the surface Ni was removed (Fig. S4.7c).

The samples were mounted onto a polishing stub using finely ground crystal bond (Fig. S4.8a). After the crystal bond had dried, the samples were thinned using 320-grit polishing paper until parts of the micro-island structures were exposed (Fig. S4.8b). The samples were then carefully thinned down using 600-grit and 1000-grit polishing papers until all of the micro-island structures were exposed (Fig. S4.8c,d).

Assembling with p^+-Si substrates

The polishing stub with the micro-island structures embedded in crystal bond was transferred to the sputterer for the deposition of a Ni/Cu back ohmic contact. In preparation for the p^+-Si substrates, the wafer was etched for 1 min in BOE, and In-Ga ohmic contact was applied to the front side of the p^+-Si substrates. Then, Ag epoxy was applied to the p^+-Si substrates, which were subsequently placed on top of the micro-island structures. The samples were cured on a hot plate at 70 °C for 30 min while a constant pressure of ~50 N m^{-2} was applied by placing an appropriate weight on top of the sample. The weight reduced small gaps and air pockets between the p^+-Si substrate and the micro-island structures. The samples were then removed from the polishing stub by heating the stub at 130 °C for 15 min on a hot plate, followed by sonicating in acetone to remove any residual crystal bond.

PDMS coating

The PDMS coating process was modified from a previously reported recipe.[8] Briefly, the micro-island structures were infilled with a mix of PDMS, toluene, and Sylguard 184 silicone elastomer curing agent in a ratio of 10:50:1. After sonicating the mixture for 15 min, the samples were placed on a spin coater, cleaned by drop-casting toluene at 3000 rpm for 1 min, and then infilled by covering the micro-island structures with the PDMS mixture followed by spin coating at 3000 rpm. The samples were then cured on a glass slide on a hot plate at 150 °C for 1.5 h.

Image Processing

During the electrochemical experiments, optical micrographs of the surface were taken every 5 min. A hexagonal array pattern was then superimposed onto the first micrograph for a positional reference (Fig. S4.9). Each frame was compared to the subsequent one where the timestamp and the positions of new failed micro-islands were

recorded manually. The distribution of failed micro-islands was plotted onto a digital replication of the electrode surface using Matplotlib library (Fig. 4.3b).

Supporting figures

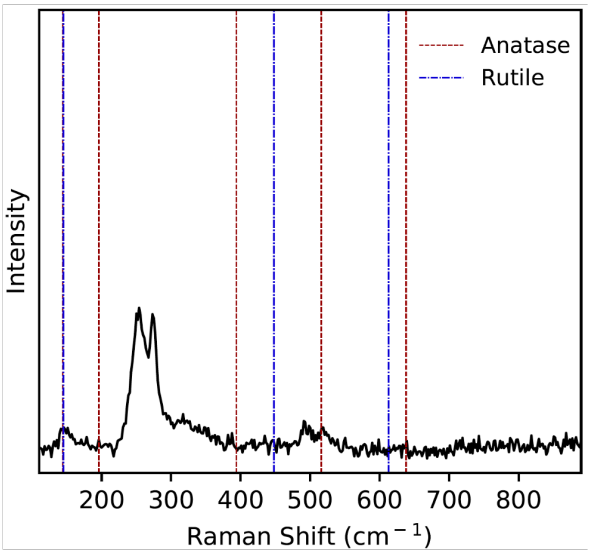

Figure S4.1. Representative Raman spectrum measured on p^+-GaAs samples coated with amorphous *a*-TiO_2-800x (GaAs/*a*-TiO_2-800x) with the dashe lines representing the respective peak positions for crystalline anatase and rutile TiO_2.

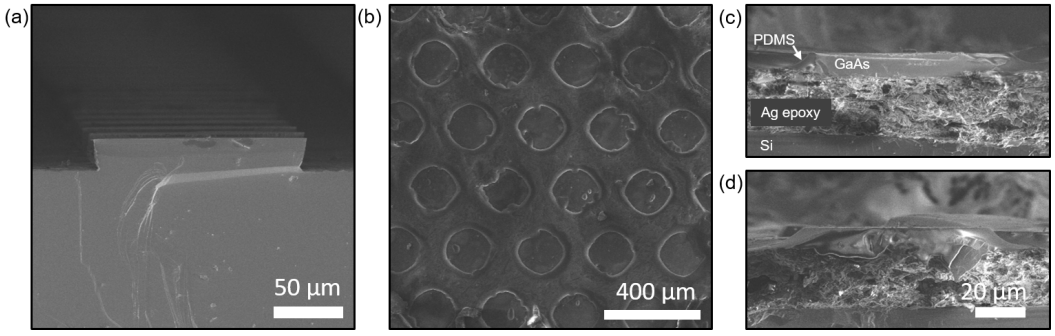

Figure S4.2. (a) Cross-sectional SEM of GaAs structure after etching (Fig. 4.1c) and SEM of (b) top surface (c, d) cross-sectional SEM of the final structure (Fig. 1i).

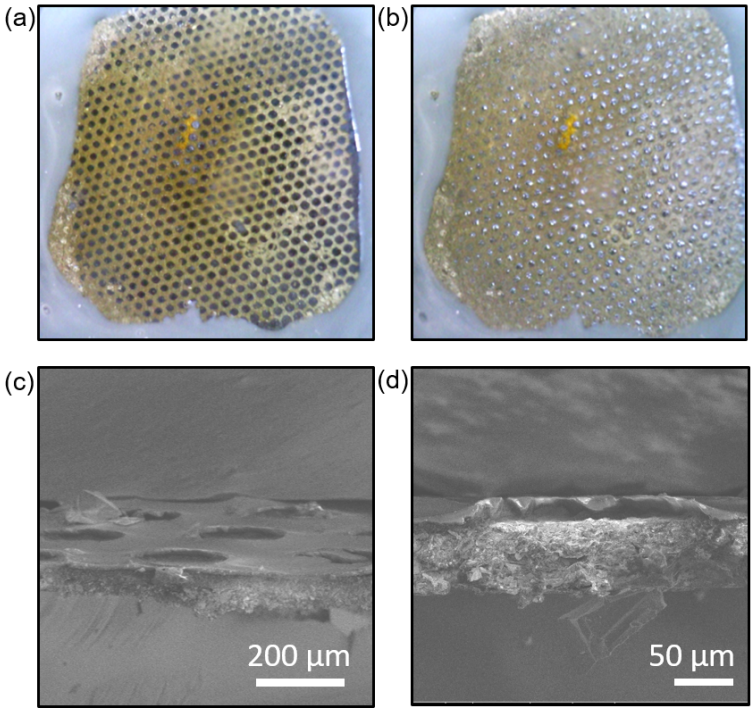

Figure S4.3. (a, b) Electrode surface (a) before and (b) after electrochemical operation. (c, d) Cross-sectioned SEM of the islands that failed after 40 h.

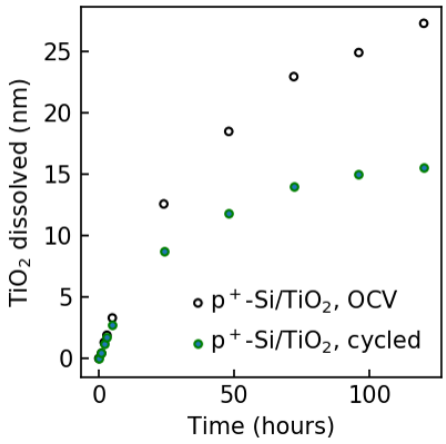

Figure S4.4. Dissolved Ti as a function of time for *a*-TiO_2-coated p^+-Si (p^+-Si/TiO_2-1500x) evaluated (black empty circles) at the open-circuit potential and (green filled circles) at 1.63 V vs RHE for 6 h followed by at the open-circuit potential for 18 h, alternatingly.

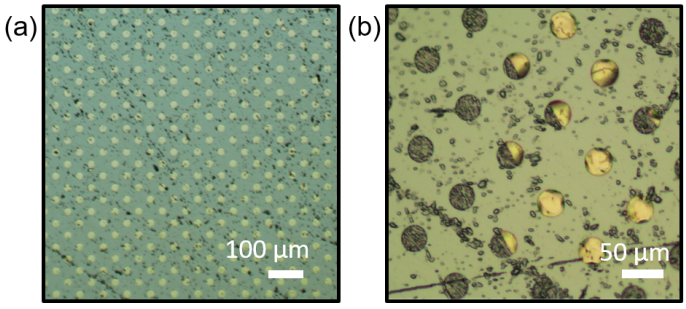

Figure S4.5. Optical micrographs of the electrode surfaces showing (a) etch pits resulting from the thinning step and (b) metal-assisted chemical etching underneath Ni masks.

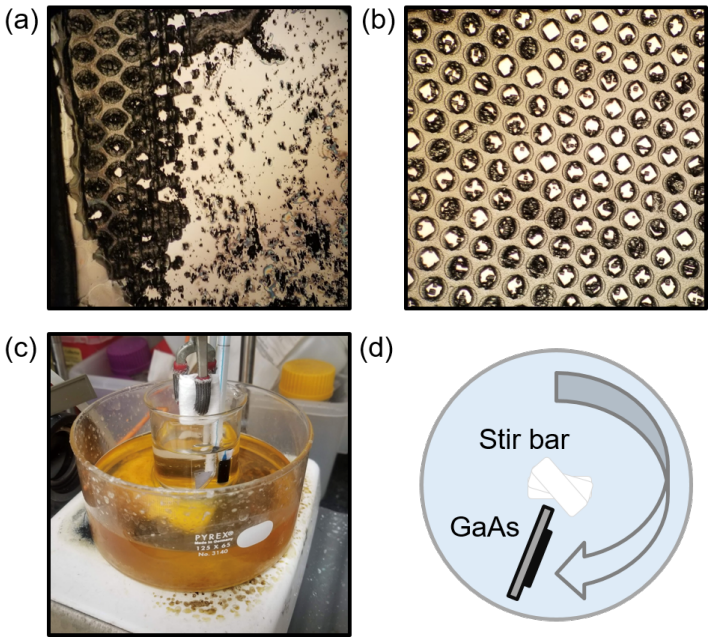

Figure S4.6. (a,b) Optical micrographs showing inconsistency of the etched surface, (c) etch bath setup, and (d) a top-view illustration of sample position in the etch bath.

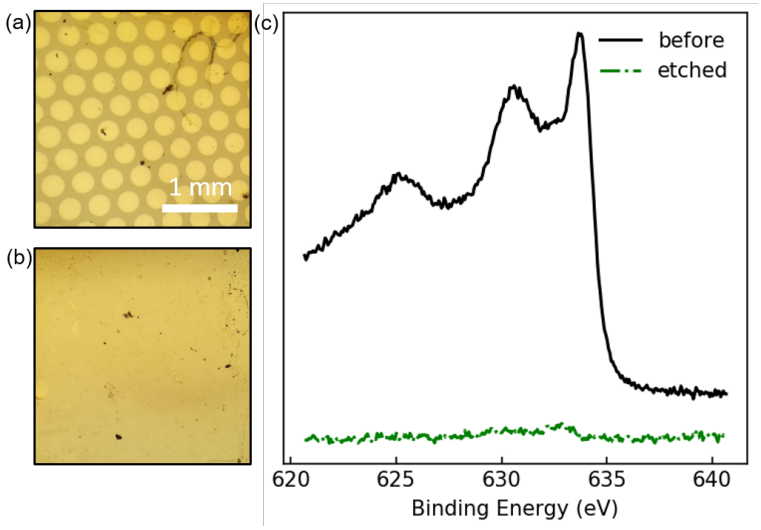

Figure S4.7. Optical microscope of a Ni mask on a GaAs substrate (a) before and (b) after mask etching. (c) XPS of Ni 2p on the respective surface.

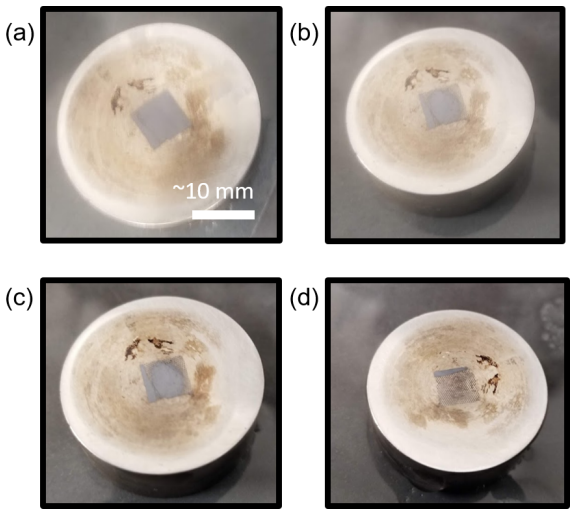

Figure S4.8. Micro-island structures embedded in crystal bond on a polishing stub with each image showing a subsequent thinning step (a-d).

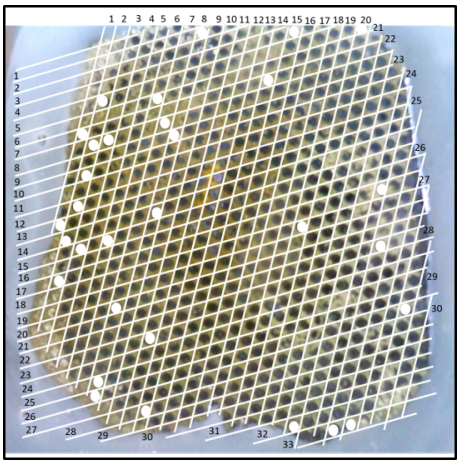

Figure S4.9. Optical micrograph of the electrode surface with a superimposed hexagonal array grid.

References

(1) Yang, F.; Nielander, A. C.; Grimm, R. L.; Lewis, N. S. Photoelectrochemical Behavior of N-Type GaAs(100) Electrodes Coated by a Single Layer of Graphene. *J. Phys. Chem. C* **2016**, *120* (13), 6989–6995.

(2) Hu, S.; Shaner, M. R.; Beardslee, J. A.; Lichterman, M.; Brunschwig, B. S.; Lewis, N. S. Amorphous TiO_2 Coatings Stabilize Si, GaAs, and GaP Photoanodes for Efficient Water Oxidation. *Science* **2014**, *344* (6187), 1005–1009.

(3) Schneider, C. A.; Rasband, W. S.; Eliceiri, K. W. NIH Image to ImageJ: 25 Years of Image Analysis. *Nat. Methods* **2012**, *9* (7), 671–675.

(4) Zhao, Y.; Liu, W.; Bao, Y.; Ma, J.; Liu, Y.; Wang, X.; Yang, F. Direct Wafer Bonding of GaAs/Si by Hydrophobic Plasma-Activated Bonding. In *Eleventh International Conference on Information Optics and Photonics (CIOP 2019)*; Wang, H., Ed.; SPIE, 2019; p 232. https://doi.org/10.1117/12.2549964.

(5) Gabriel, M.; Johnson, B.; Suss, R.; Reiche, M.; Eichler, M. Wafer Direct Bonding with Ambient Pressure Plasma Activation. *Microsyst. Technol.* **2006**, *12* (5), 397–400. https://doi.org/10.1007/s00542-005-0044-4.

(6) Plach, T.; Hingerl, K.; Tollabimazraehno, S.; Hesser, G.; Dragoi, V.; Wimplinger, M. Mechanisms for Room Temperature Direct Wafer Bonding. *J. Appl. Phys.* **2013**, *113* (9), 094905. https://doi.org/10.1063/1.4794319.

(7) DeJarld, M.; Shin, J. C.; Chern, W.; Chanda, D.; Balasundaram, K.; Rogers, J. A.; Li, X. Formation of High Aspect Ratio GaAs Nanostructures with Metal-Assisted Chemical Etching. *Nano Lett.* **2011**, *11* (12), 5259–5263.

(8) Kennedy, K. M.; Kempler, P. A.; Cabán-Acevedo, M.; Papadantonakis, K. M.; Lewis, N. S. Primary Corrosion Processes for Polymer-Embedded Free-Standing or Substrate-Supported Silicon Microwire Arrays in Aqueous Alkaline Electrolytes. *Nano Lett.* **2021**. https://doi.org/10.1021/acs.nanolett.0c04298.

Chapter 5

CONCLUSIONS

In this thesis, corrosion mechanisms of CdTe and ZnTe under conditions for HER were explored. The dissolution rates for CdTe and ZnTe under bias and under OCV were quantified for the samples in 1.0 M H_2SO_4 (aq) and 1.0 M KOH (aq). In an acidic media, both CdTe and ZnTe were found to corrode chemically, while in an alkaline solution, reduction of anion Cd^{2+} was the main corrosion pathway for CdTe, but both reduction of the anion Zn^{2+} and oxidation of the cationTe^{2-} were attributed to the corrosion of ZnTe. Pt catalyst overlayer was found to help mitigate corrosion in CdTe, but not in ZnTe, where protective coating is needed to achieve long-term stability.

In addition, physical pinhole defects in the protective amorphous a-TiO_2 grown by ALD were investigated. The initial pinhole defects in the as-deposited a-TiO_2 film, exposing the GaAs anodes, were attributed to atmospheric particulate during the deposition. Nevertheless, on GaAs anodes coated with pinhole-free a-TiO_2 film, new pinholes can still develop during the electrochemical operation.

In order to study the origin and the evolution of pinhole formation during the electrochemistry, GaAs micro-island structures were fabricated to provide defects isolation during testing, preventing new pinholes from propagating to the nearby sites. The number of failed micro-wires as a function of time indicates that new pinholes formed within the first 30 hours of an electrochemical operation that were developed from a limited number of defect spots in the a-TiO_2 film. Measurements of TiO_2 dissolution also agree that the corrosion of a-TiO_2 is unlikely the dominating contribution to the new pinhole formation during this initial time frame.

Future Directions

- For the study of CdTe and ZnTe corrosion mechanisms, residual oxygen present during the experiment could be contributing to the oxidative processes in addition to applied bias. Thus, an equivalent study in an oxygen-free environment would provide additional insights to the fundamental of CdTe and ZnTe corrosion.
- Although further development is needed to improve the compactness of the contact layer between the supporting p^+-Si and GaAs micro-islands film, the processes described in this work could be translated to fabrication of micro-islands structures on more complicated GaAs stacks, such as a np^+-GaAs homojunction device. Demonstration of such device would further confirm the feasibility of using this fabrication procedure in real practical devices.

A p p e n d i x

OXYNITRIDES

The following chapter discusses some preliminary results on the growth of oxynitride materials and their tunable bandgap.

Introduction

Finding stable semiconductor electrodes with suitable band edge positions remains one of the challenging tasks to realizing practical solar fuel devices. Most photoanodes are comprised of metal oxides. The typical deep lying valence band in these materials is dominated by the O 2p orbital contribution, resulting in too large a band gap and a very positive valence band edge, precluding efficient water oxidation. It is proposed that nitrides and sulfides can overcome this problem because their valence band position is usually higher in energy, but these materials suffer from poor electrochemical stability[1]. Developing metal oxynitrides that afford tailoring of properties of oxides and nitrides could allow for stable and efficient metal photoanodes. Metal oxynitrides could retain stability of oxides with a valence band position that could yield band gaps in 1.2-2.5 range.[2] Varying the O/N ratio can lead to varying contributions of O 2p and N 2p orbitals in the valence band of oxynitride systems. In addition, because of its variable band edge positions, oxynitrides will also be useful tools for studying the semiconductor's stability as a function of band position as theoretically proposed.[3] Detailed study of most promising materials could also elucidate trends in band shifts with changing O/N ratio and formation of new phases.

Tantalum oxynitride (TaON) is one of the promising candidates as an oxynitride material for initial screening. Ta_3N_5 and TaON have been demonstrated to be potential photoanodes for water oxidation.[4] Tantalum nitrides are also reported to have good stability under PEC operation.[5] TaON has also been synthesized by reactive magnetron sputtering[6].

TaON fabrication

A radio-frequency sputtering system (AJA International Inc.) was used to deposit TaON film onto p^+-Si. The base pressure was kept at $<1x10^{-7}$ Torr, and the deposition pressure was kept at 5 mTorr. A radio-frequency (rf) power of 100 W was used during the deposition. In order to introduce nitrogen into the films, the same Ta target was used, but with varying gas flow. Three gas channels were used during the deposition: argon (Ar), N_2, and argon mixed with 10% oxygen (Ar/O_2)

The films were later characterized for the absorption edges using ultraviolet-visible spectroscopy (UV-VIS). Figure A.1 shows a tauc plot representing the bandgap for the samples with Ar/O_2 gas ranging from 0 to 5 sccm during the deposition. The bandgap of the TaON films ranges from 1.22 eV to 3.53 eV.

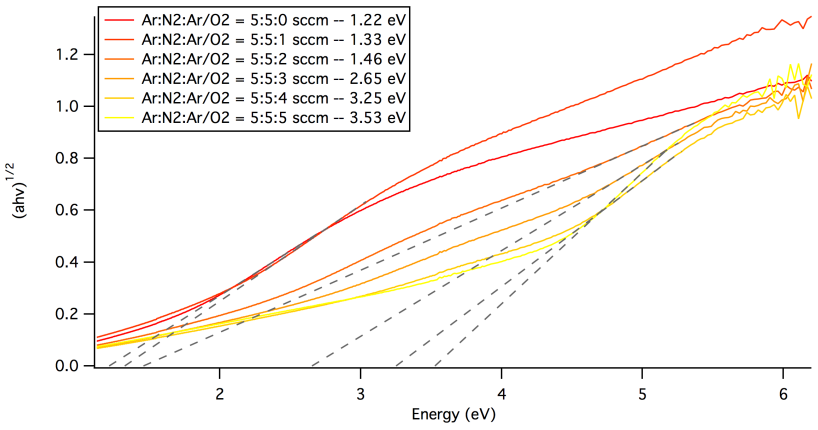

Figure A.1. Tauc plot of sputtered oxynitride sampes grown with different reactive gas flows.

Nevertheless, the electronic properties and the crystal structures of these sputtered films are considerably poorer than typical semiconductor substrates, mostly due to high deposition energy during the sputtering process preventing a crystalline structure to form. Moreover, subsequent annealing would release nitrogen that was originally incorporated in the lattice.

Another technique that can be utilized to make metal oxynitrides is single-crystal growth via float-zone. LaTiO was prepared as a precursor to LaTiON instead of TaON.

LaTiON fabrication

Oxide single-crystal synthesis

Polycrystalline samples of $LaTiO_{3.5}$ were prepared by traditional solid state reactions by heating the single-oxide precursors as starting reagents. The resulting powders were pressed in rods and sintered at 1200C for 12 h. The rods were then used as feeds for the crystal growth by the floating zone method. During the crystal growth, the rate was maintained at 10 mm h^{-1} and the seed and feed rods were counterrotated at 30 rpm and 15 rpm, respectively. A constant flow of oxygen was used as the crystallization atmosphere. After growth, the samples were slowly cooled to room temperature over a period of 6 hours to minimize the formation of cracks. The resulting crystal samples were cleaved using a razor blade into thin wafers along the growth direction and used for the subsequent nitridation step.

Oxynitride conversion

The single-crystal oxide wafers were placed in a tube furnace under constant flow of NH_3 at a temperature of 950ºC for approximately 2 hours. After the reaction, the previously transparent crystals became deep-red signaling the formation of the oxynitride layer.

Charaterizations

Figure A.2 shows single-crystal samples of the LaTiO and LaTiON samples. The vibrant red indicates an expected bandgap of ~2 eV. Figure A.3 shows work function and the valence band position measured by X-ray photoelectron spectroscopy. The calculated band edges diagram suggests suitable band energetics for both OER and HER.

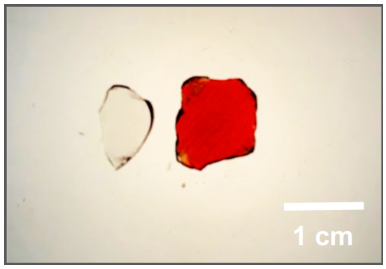

Figure A.2. Single-crystal LaTiO and LaTiON.

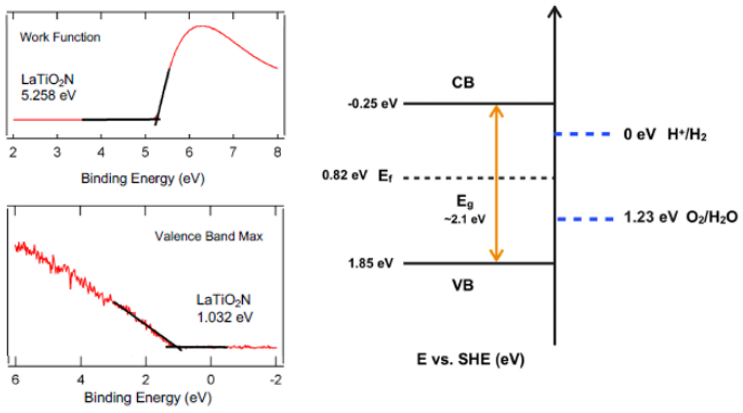

Figure A.3. Band position measurements.

References

(1) Maeda, K.; Domen, K. New Non-Oxide Photocatalysts Designed for Overall Water Splitting under Visible Light. *J. Phys. Chem. C* **2007**, *111* (22), 7851–7861. https://doi.org/10.1021/jp070911w.

(2) Wu, Y.; Lazic, P.; Hautier, G.; Persson, K.; Ceder, G. First Principles High Throughput Screening of Oxynitrides for Water-Splitting Photocatalysts. *Energy Environ. Sci.* **2013**, *6*, 157–168. https://doi.org/10.1039/c2ee23482c.

(3) Gerischer, H.; Mindt, W. The Mechanisms of the Decomposition of Semiconductors by Electrochemical Oxidation and Reduction. *Electrochim. Acta* **1968**, *13* (6), 1329–1341. https://doi.org/10.1016/0013-4686(68)80060-X.

(4) Takata, T.; Pan, C.; Domen, K. Recent Progress in Oxynitride Photocatalysts for Visible-Light-Driven Water Splitting. *Sci. Technol. Adv. Mater.* **2016**, *16* (3), 033506. https://doi.org/10.1088/1468-6996/16/3/033506.

(5) Ahmed, M.; Xinxin, G. A Review of Metal Oxynitrides for Photocatalysis. *Inorg. Chem. Front.* **2016**, No. 2. https://doi.org/10.1039/C5QI00202H.

(6) Taviot-Guého, C.; Cellier, J.; Bousquet, A.; Tomasella, E. Multiphase Structure of Tantalum Oxynitride TaO x N y Thin Films Deposited by Reactive Magnetron Sputtering. *J. Phys. Chem. C* **2015**, *119* (41), 23559–23571. https://doi.org/10.1021/acs.jpcc.5b07373.